Vortex sensing and energy expenditure of fish exposed to unsteady flow and biomimetic transfer of noise filter and signal amplification techniques

Dissertation
zur
Erlangung des Doktorgrades (Dr. rer. nat.)
der
Mathematisch-Naturwissenschaftlichen Fakultät
der
Rheinischen Friedrich-Wilhelms-Universität Bonn

vorgelegt von
Adrian Thomas Klein
aus
Wuppertal

Bonn 2012

Angefertigt mit Genehmigung der Mathematisch-Naturwissenschaftlichen Fakultät
der Rheinischen Friedrich-Wilhelms-Universität Bonn

1. Gutachter Prof. Dr. H. Bleckmann
2. Gutachter Prof. Dr. W. Alt
Eingereicht im Dez. 2012
Tag der Promotion: 29.05.2013
Erscheinungsjahr: 2013

Diese Dissertation ist auf dem Hochschulschriftenserver der ULB Bonn
http://hss.ulb.uni-bonn.de/diss_online/ elektronisch publiziert

Abstract

Biomimetics is a promising field of research in which natural processes and structures are transfered to technical applications. Part one and two of this work investigate the behavior and the hydrodynamic sense of fish to uncover strategies for locomotory cost reduction and navigation in unsteady flow. Fish detect unsteady flow with their lateral line organ. Trout and rudd were exposed to an unsteady flow signature caused by submerged cylinders. Trout preferred distinct three dimensional regions relative to the cylinder and showed less muscle activity than in non-preferential regions. Interestingly one of those regions had a three dimensional flow signature compared to the almost two dimensional flow pattern of a vortex street. Navigation in complex flow requires sensors and smart signal processing. This work shows that the activity of central neurons of rudd involved in the processing of hydrodynamic information correlated with unsteady flow signatures in terms of spike pattern or spike rate or both. It would be advantageous for robots to use an artificial hydrodynamic sense together with natural inspired signal processing to reduce locomotory costs and also navigate in complex hydrodynamic habitats. In sensory systems it is crucial to separate meaningful signals from noise which may occur in complex habitats. Nature has developed a stunning diversity of lateral line morphologies. The function is not well understood. Part three and four of this work investigate several lateral line morphologies with respect to noise filtering and signal amplification mechanisms. To do so an artificial lateral line sensor was used. Therefore it was possible to gain control of all parameters. An artificial lateral line design was found which significantly enhances signal to noise ratio and therefore this work uncovers the function of this natural morphological occurrence. Additionally a finite element model with fluid structure interaction was used to develop a signal enhancing design of artificial neuromasts for fabrication with microelectromechanical systems. Interestingly a similar structure occurs in nature. Last but not least in part five this work shows an eight channel artificial lateral line canal sensor available with automatic fabrication techniques.

Associates

This work was supported by associates in projects I had supervised. Simon Kranz and Felix Kaldenbach recorded muscle activity and tracked fish with Vidana in the study on the locomotion and energy expenditure of trout. In this work I established the method for recordings of free swimming trout in our flow channel, developed the experimental protocol, did the particle image velocimetry (PIV), three dimensional tracking, further analysis and statistical examination. Jan Winkelnkemper did the surgery, the unit recordings and the PIV recordings of the medial octavolateralis nucleus (MON) study. He used my scripts to automatically calculate spike rates. I proposed the set-up design which enabled synchronous PIV and MON unit recordings, developed the experimental protocol enabling statistics of balanced data sets with respect to altering experimental conditions, wrote spike rate and pattern analysis scripts, proposed statistical tests for single unit and recorded unit population analysis and did the integration of PIV and unit response. Stephanie Noack and Dominic Holtkamp supported my measurements during the signal noise study and manufactured parts of the artificial lateral line sensors based on my blueprints. Maximilian Bothe supported my measurements during an object classification study shown in future prospects. The machine shop of the Institute of Zoology (University of Bonn) manufactured parts of the experimental set-ups and build artificial lateral line canals of the signal noise part based on my blueprints. The microelectromechanical systems (MEMS) group of caesar build artificial canals with dimensions based on my finite element simulation and supported me with images of those MEMS sensors. The workshop of the institute casear build devices based on my blueprints in which I combined my silicon bar arrays and eight channel circuits. Matthias Mayser supported me with 3-D microscope images of my eight channel artificial lateral line sensor. Parts of this work have been published or are in preparation and are referenced in the publication part of this work.

Contents

List of Figures

1 Introduction

1.1 Model system fish and biomimetic transfer

Fish live in a fluid environment, therefore it is not surprising that fish have developed smart strategies for locomotion in fluids, a variety of specialized flow sensors – enabling the exploration of a three dimensional habitat – and neural circuits which lead to complex behaviors crucial for survival. Fluids are also involved in many human applications ranging from transportation tasks via international air or water routes and pipelines, microfluidics in medicine and industry. Flow and pressure sensors and mathematical algorithms are in use to control such applications. This work investigates the performance of fish respecting the unsteady flow and transfers the fundamental natural principles of the hydrodynamic sense of fish to improve existing flow sensors or even find new ones for technical applications.

1.2 Behavior of rheophilic fish exposed to hydrodynamic flow fluctuations

Rheophilic fish like trout experience a wide range of flow velocities and hydrodynamic perturbations. Instead of avoiding flow perturbations rheophilic fish often exploit turbulent zones associated with physical structures to reduce locomotory costs (Gerstner and Webb, 1998; Webb, 1998b). To learn how trout use flow perturbations for the reduction of energy expenditure behavioral studies have been undertaken in a controlled laboratory environment. Webb (1998a) placed single cylinders horizontally and vertically inside a flow channel and studied how water motions caused by the cylinders altered the swimming behavior of river chub (*Nocomis micropogon*) and smallmouth bass (*Micropterus dolomieu*). Liao et al. (2003a) used a D-shaped cylinder (hereafter referred to as cylinder) for a similar study with trout. A cylinder exposed to running water causes defined local changes in flow velocity, flow direction and hydrodynamic pressure (Zdravkovich, 1997). At Reynolds numbers (Re) >140 a cylinder sheds columnar vortices of alternating sign called a Kármán vortex street (Blevins, 1990; Vogel, 1996).

Liao et al. (2003a) compared the swimming behavior of trout exposed to undisturbed unidirectional flow with that of trout exposed to the flow environment altered by the cylinder. Compared to free stream swimming, trout easily hold station in the vicinity of a cylinder by either swimming in the region of reduced flow immediately behind the cylinder (drafting), by swimming in the further downstream Kármán vortex street (Kármán gaiting), by using the high-pressure reduced-flow bow wake zone in front of the cylinder (bow wake swimming) or by moving into a stable position close to and sideways of the cylinder (entraining)(see also Webb (1998a); Przybilla et al. (2010) and Bleckmann et al. (2012)). Compared with trout swimming in undisturbed flow there was a reduced tail beat frequency during Kármán gaiting, entraining and swimming in the bow wake zone (Liao et al., 2003a; Przybilla et al., 2010). This is in line with the observation that Kármán gaiting trout recruit relatively few axial swimming muscles for station holding (Liao et al., 2003b; Liao, 2004), a finding that was derived from single muscle bursts of trout holding station while Kármán gaiting.

Up to now red axial muscle activity has only been recorded from normal swimming and Kármán gaiting trout. Therefore, red muscle activity was additionally recorded from drafting trout and from trout swimming in the bow wake zone. Instead of only analyzing single muscle bursts, red and white muscle activity of trout swimming continuously for four hours have been recorded. Mean muscle activity was quantified and plotted as a three-dimensional function of trout position. As expected (Liao et al., 2003a; Przybilla et al., 2010), station holding trout preferred the Kármán gait, entraining, and bow wake region. In addition, trout displayed an up to now undescribed wave mode. In three of four regions, muscle activity was significantly reduced compared to the muscle activity observed while swimming in other areas of the flow tank. Thus, the amount of muscle activity necessary to hold station plays a deciding role for habitat selection in trout. In addition particle image velocimetry (PIV) was used to quantify the flow field.

1.3 How fish sense and perceive hydrodynamic flow fluctuations

Nature has invented a stunning diversity of sensory systems, whose small size and high sensitivity so far is unmatched by man-made devices. Flow sensors based on hairs are located on the skin and are found in crustaceans (Bender et al., 1984), but also in spiders and insects (Humphrey and Barth, 2007). These sensors en-

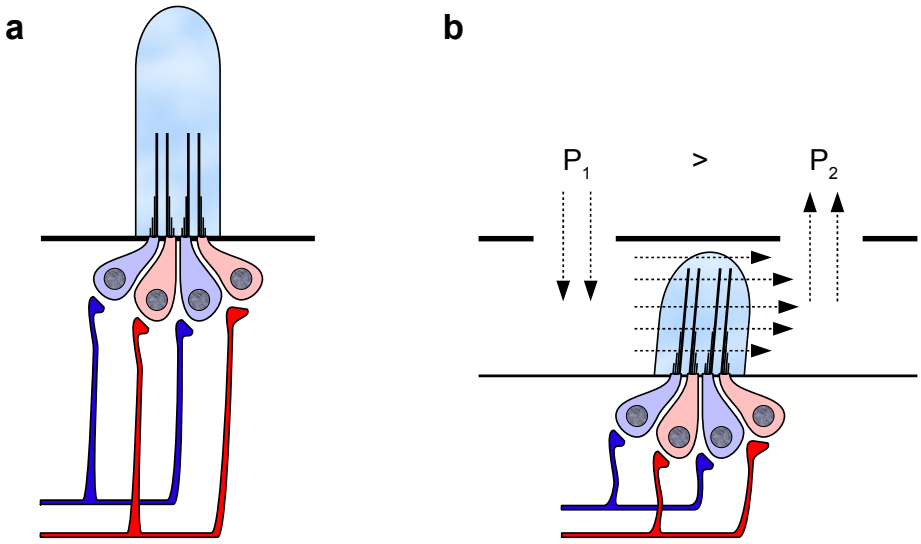

Figure 1.1: Structure of a superficial neuromast (a) and a canal neuromast (b). Both, superficial and canal neuromasts consist of hair cells and a gelatinous cupula. The cupula is interspersed with cilia bundles of hair cells. Two antipodal groups of polar hair cells (light red and light blue) cause the directional sensitivity of a neuromast. Each nerve fiber innervates exclusive (red/blue) one group of hair cells. In contrast to superficial neuromasts (a), which are directly exposed to the water surrounding the fish, canal neuromasts (b) are submerged in fluid filled canals. For instance, pressure differences ($P_1 > P_2$) cause flow inside the canal and therefore a deflection of the cupula. Modified and redrawn after (Å. Flock and Wersäll, 1962; Münz, 1985; Kalmijn, 1988; McHenry and van Netten, 2007; Bleckmann, 2008)

able insects and spiders to perceive air displacements down to flow amplitudes of 30 μm/s (Shimozawa et al., 2003). Flow sensors are also found in fish and aquatic amphibians and are called lateral line neuromasts (Fig. 1.1). With neuromasts some fish can detect water surface waves with a displacement amplitude of only 0.01 μm (Bleckmann, 1980). Most lateral line neuromasts are located on the skin (superficial neuromasts or SN), but some are located in subepidermal canals (canal neuromasts or CN). In a certain frequency range the cupula of a neuromast is deflected in proportion to water velocity due to viscous drag. The response properties of CNs in addition are determined by the diameter of the lateral line canals (LLCs))(Denton and Gray, 1983; van Netten, 2006). In general CNs respond in proportion to the pressure differences between neighboring canal pores (Kalmijn, 1988; Coombs et al., 1996), each of which connects the canal to the surrounding water. A lateral line neuromast consists of up to several hundreds or even thousands mechanosensitive hair cells, enveloped in a gelatinous cupula.

Lateral line hair cells are morphologically polarized, i.e. they have a bundle of stereocilia (stereovilli) at their apical surface that grows longer from one edge to the other towards one kinocilium (true cilium). Within the sensory epithelium of a neuromast, lateral line hair cells are oriented into two opposing directions that define the most sensitive axis of the neuromast (Å. Flock and Wersäll, 1962). Although the design of the lateral line may alternate among fish species (Coombs et al., 1988), most fish have several hundred (sometimes up to several thousand) SNs distributed over their head, body and tail fin (Schmitz et al., 2008). Different neuromasts may respond differently to the same water motions since the mechanical properties of the lateral line are also determined by the stiffness of the kinocilia and stereovilli and by the size and shape of the cupula (van Netten and Khanna, 1994; McHenry and van Netten, 2007; McHenry et al., 2008).

Lateral line information is processed from medulla to telencephalon. Hydrodynamic information of SNs and CNs is processed parallely. Lateral line nerves with fibers innervating either SNs or CNs enter the ipsilateral brainstem and terminate in the medial octavolateralis nucleus (MON) inside the hindbrain. Some primary lateral line projections may reach the ipsilateral cerebellar granular eminence and the corpus and valvula cerebelli. The MON projects bilaterally, with a majority of fibers projecting contralaterally, in the lateral portion of the torus semicircularis and in the deep layers of the optic tectum. Some diencephalic and telencephalic nuclei are involved in the processing of lateral line information (Bleckmann, 2008).

Fish use their lateral line for prey detection, predator avoidance, shoaling, intraspecific communication, rheotaxis and station holding (Bleckmann, 1994; Liao, 2007). Additionally, the lateral line system enables fish to form a spatio-temporal image of nearby objects based on their hydrodynamic signature (Windsor et al., 2008, 2010a,b). Lateral line afferents not only respond to the sinusoidal water motions generated by a vibrating sphere (Coombs et al., 1996; Engelmann et al., 2002) but also to more natural stimuli, such as single vortices (Chagnaud et al., 2006) or vortex streets caused by a cylinder exposed to running water (Chagnaud et al., 2007). The direction of water motions inside a vortex ring as well as the vortex shedding frequency of a cylinder can be determined from the responses of primary lateral line afferents (Chagnaud et al., 2006, 2007). Lateral line nerve fibers also alter their discharge rate if an object passes the fish laterally. In this case the discharge pattern reflects both, the position (including distance) of the object and the direction of object motion (Mogdans and Bleckmann, 1998).

1.4 Noise filter mechanisms and signal amplification

Fish live in various habitats that differ in their hydrodynamic noise (e.g. in lakes and ponds or in fast running rivers). For this reason, it is not surprising that the morphology of the peripheral lateral line is highly diverse (Coombs et al., 1988). For instance, neuromasts may occur free standing on the skin (superficial neuromasts), in grooves or in fluid filled canals (canal neuromasts). In general, CNs respond (up to a frequency of about 150 Hz) almost in proportion to the pressure gradient between neighbouring pores and thus to external water acceleration (van Netten, 2006). In contrast SNs respond (up to about 80 Hz) almost in proportion to water velocity (Kalmijn, 1988). The number of hair cells in a neuromast as well as the size and shape of the cupulae may be different in different fish species. Head lateral line canals may be simple (*Perciformes*), groovelike (*Holeocephali*) or furcated (*Clupeomorpha*). Most fish species have one trunk lateral line canal on each side of the body (e.g. *Carrasius auratus*), but some fish (e.g. *Brachydanio rerio*) have either no or up to four trunk canals (e.g. *Xiphister atropurpureus*) on each body side (Webb, 1998b). The diameter of the canals, size of canal pores as well as the inter pore distances may also vary across species. Despite this variability the functional significance of the lateral line diversity is still not understood.

1.5 An artificial lateral line

The sensory hairs of crustaceans, insects and spiders and the lateral line system of fish have inspired engineers and biologists to develop artificial air (Krijnen et al., 2006; Kladt, 2007) and water flow sensors (Brücker et al., 2004; Groe et al., 2006; Yang et al., 2010, 2011; Klein and Bleckmann, 2011; Klein et al., 2011; Klein and Bleckmann, 2012; Venturelli et al., 2012) based on manual fabrication and microelectromechanical system (MEMS) technology. With individual sensors, mimicking SN or sensory hair function, the air or water motions caused by a vibrating sphere can be detected (Krijnen et al., 2006) and a vibrating sphere can even be localized, if arrays of multiple sensors are used (Yang et al., 2010).

There have been several attempts to understand, model and design an engineering equivalent to the sensory hairs of insects, spiders (Humphrey et al., 1993; Barth, 2004; Krijnen et al., 2006), scorpions (Kladt, 2007) and of the superficial neuromast system of fish. However, an engineering equivalent of the fish lateral line canal system has not been existed so far, therefore artificial lateral line canals

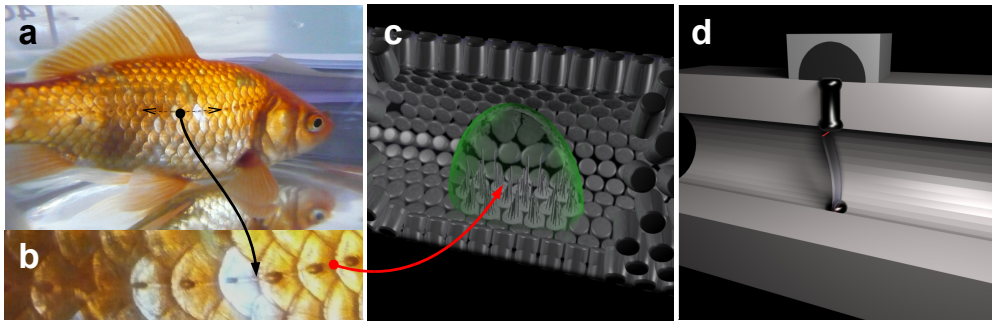

Figure 1.2: Pores of the trunk lateral line canal of a goldfish (a) expand lateral from caudal to cranial. In the magnification (b) the canal is visible under the translucent skin. Neuromasts are embedded inside the canal (c) and sit between adjacent pores (not shown). This principle was transfered to design an optical artificial canal neuromast (d, see section 2.3.1). Modified after (Klein and Bleckmann, 2011).

(ALLCs) have been build and equipped with artificial neuromasts (ANs) (Klein and Bleckmann, 2011; Klein et al., 2011; Klein and Bleckmann, 2012) (Fig. 1.2). Unlike other artificial neuromasts, the neuromasts were developed using optical signals to measure water or air motions. With these optical flow sensors water (air) motions were measured inside artificial canals and thus it was possible to quantify outside pressure gradients. The performance of the ALLCs was assessed by exposing them not only to the pressure gradients caused by a stationary vibrating sphere but also to the vortical flows caused by a cylinder placed upstream in running water. It was shown that ALLCs can even be used to determine the position and size of an upstream cylinder and to detect and localize a moving object.

For many reasons it is difficult to study form-function relationships in natural lateral lines. It is known that lateral line canals can shield canal neuromasts from DC-flow (Engelmann et al., 2002). However, the morphology of lateral line canal systems is so diverse that it is difficult to study the influence of a single canal parameter (e.g. canal diameter or inter pore distance) on the mechanical (filter) properties of a canal in physiological experiments. For this reason artificial lateral line canals, equipped with highly sensitive artificial neuromasts, were used to investigate lateral line filter properties.

1.6 Computational models and modern sensor fabrication techniques

Hand made senors are expensive and vary in their frequency characteristics as well as sensitivity. For commercial use it is necessary to manufacture cheap sensors in reproduceable quality. The use of machine automation is advantageous but manufacturing methods change with the scale of the system. This work examines two methods for the automatic production of artificial lateral line systems. Microelectromechanical systems (MEMS) offers methods for mass fabrication of devices in the nano- and micromilimeter scale whereas micromachining offers methods for mass fabrication of devices in the micro- and millimeter scale.

MEMS is primary based on a sequence of lithography, etching and deposition steps (Lamers and Pruitt, 2011). In lithography, structures are transfered on a photosensitive layer. Dependent on the properties of the layer material exposed or unexposed regions are removed. Etching removes material of the base substratum which is not covered by the thin layer material. In deposition a layer of new material is grown on the substratum. With lithography, etching and deposition 3-dimensional structures can be build with mechano- and electrical properties. In MEMS the main effort of research occurs at the point of finding the correct parameters for each fabrication step (lithography, etching and deposition). Parameters change with sequence step and dimension of structures. Therefore it is of advantage to know the sequence as well as the dimension of the sensor device before starting the research on production parameters for MEMS. Like in fish the sensitivity and filter properties of an artificial canal neuromast depends on the material properties and the scale of the system. Finite element modeling (FEM) is a method which enables the simulation of several sensor designs to find a set of design parameters for production with MEMS which work. In this work fluid structure interaction (FSI) was simulated using FEM. In a parameter scan several virtual sensor designs were tested with respect to sensor sensitivity. A design was found in the range of aspect ratios which were achievable with MEMS. The developed design improves signal detection compared to a straight artificial lateral line canal design. Based on the proposed simulation a MEMS sensor was developed in the institute caesar in Bonn as a first proof of concept.

In contrast to MEMS - which is applicable in the sub millimeter scale - classical fabrication techniques were used in this work to build an 8 channel artificial lateral line array in the millimeter scale. Each step of the proposed production is available with automatic fabrication. The fabricated sensor was sensitive to vibrating spheres and to vortex streets. Vortex streets caused time shifted signals which altered with place.

2 Materials and methods

2.1 The energy expenditure of trout exposed to unsteady flow

2.1.1 Experimental Animals

For the experiments 6 rainbow trout, *Oncorhynchus mykiss* (Walbaum 1792, total body length L 13.8 ± 2.2 cm, mean $\pm$ s.d.) were used. Trout were purchased from a local dealer and held individually in 45 l aerated fresh water tanks (water temperature: min 13°C, max 16°C) equipped with a hideout and a filter pump. Feeding took place daily with fish pellets.

2.1.2 Experimental set-up

For experiments a custom-made flow tank (volume 1000 l, for detailed information see Przybilla et al. (2010), water temperature 12 - 14°C, min max) consisting of an entrance cone (constriction ratio 3 : 1) and a working section (width 28 cm, height 40 cm, length 100 cm, water level 28 cm) made of transparent Perspex, delineated within the flow tank by upstream and downstream nets (mesh width 1 cm, fiber diameter 0.02 cm). The origin of the coordinate system (x length, y width, z height) was defined as the lower right corner of the experimental volume while looking upstream (Fig. 2.1 a and b). Flow was generated by two propellers (Kaplan propellers, 23×30 cm^2, Gröver Propeller GmbH, Köln, Germany), located downstream of the working section. These were coupled to a motor (SRF 10/1, Walter Flender Group, Düsseldorf, Germany). To avoid coarser-scale eddies in the working section, the water was directed through a collimator (inner tube diameter 0.4 cm, tube length 4 cm) and two turbulence grids (mesh widths 0.5 cm and 0.25 cm, wire diameters 0.1 cm and 0.05 cm). Two 150 fluorescent lamps were installed above the working section and light was diffused with a white diffusor plate. A solid acrylic glass cylinder (diameter 5 cm), cut lengthwise in half (D-shaped cylinder, hereafter referred to as cylinder) was placed vertically in the middle of the working section close to the upstream (upstream case, up. c.) or downstream net (downstream case, down. c.) to generate hydrodynamic perturbations.

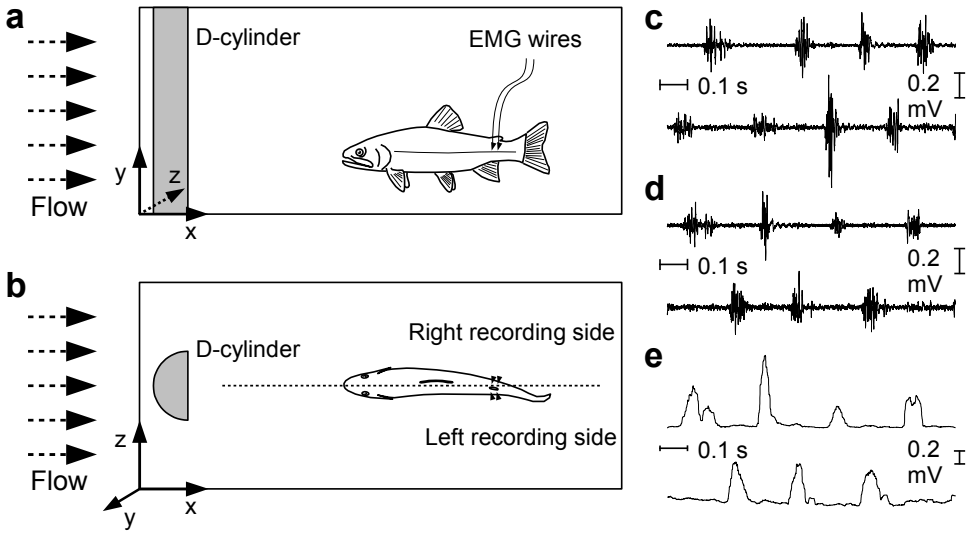

Figure 2.1: Set-up used to investigate the muscle activity of trout exposed to unsteady flow. Side (a) and top (b) view of the experimental set-up. A D-shaped cylinder was placed up- or downstream (not shown) in the experimental volume. The muscle activity of trout was recorded with thin wires. For the long time study it was necessary that recording quality did not change over time (c: start of the experiment, d: end of the experiment). To further analyse the data a sliding RMS filter was applied to the recordings (e).

2.1.3 Electromyographic recordings

Electromyograms (EMGs) were recorded from the left and right axial swimming muscles of unrestrained trout with copper wires (0.056 cm diameter, Magnet Wire, AWG 43T, PlanetEngineers.com). Wire electrodes were constructed by threading one end of a wire through the barrel of a hypodermic needle (Terumo, Neolus, 25G x5/8″). Thereafter the tip of the wire was stripped of its insulation and rolled into a hook using fine, micro-forceps and pulled snug against the needle tip for insertion (Loeb and Gans, 1986).

2.1.4 Surgical procedures

Trout were cooled down in ice water until all movements ceased. Differential electrodes were placed close to the trunk lateral line canal at the level of the adipose fin (Fig. 2.1 a and b). The distance between each electrode pair was 4 mm. After surgery trout were placed inside the flow tank and exposed to laminar flow (< 0.1 m/s). This caused them to swim against the current and thus assured that they did not entangle in the copper wires.

2.1.5 Experimental procedures

In each experimental setting five trout were tested. If it was attempted to analyze muscle activity during bow wake swimming the cylinder was position close to the downstream net (downstream case). In all other cases the cylinder was positioned close to the upstream net (upstream case). After recovery from electrode implantation each trout was tested at the bulk flow velocities 0.19, 0.28, 0.36, and 0.48 m/s (cf. PIV).

2.1.6 Verification of recording conditions

A single trout was exposed to the cylinder and muscle activity was recorded. After visible alternating patterns inside recordings the animal was killed and tied downstream of the cylinder inside the Kármán gait zone. For control recordings were repeated.

2.1.7 Video analysis

A video camera (frame rate 25 Hz) filmed the trout in side and bottom view using a mirror that was mounted at 45° below the working section. Both views were calibrated. To do so the image plane of the camera was adjusted parallel to the side of the flow channel such that the bottom of the flow channel crossed the center of the image plane (cf. Fig. 2.2 a). Therefore the side of the flow channel was visible in the upper half of the image (side view) and the bottom of the flow channel – which was visible with the 45° orientated mirror – was visible in the lower half of the image (bottom view). In both views the center of mass of the trout was tracked (side view point r_s, bottom view point r_b) with the software Vidana 2.0 (www.VidAna.net). To simplify the calibration procedure the bottom view was treated as a single camera with its image plane orientated parallel to the bottom of the flow channel (Fig. 2.2 b). Knowing the focus points (f_s and f_b) of both views, the relative position of the center of both image planes (P_s and P_b) and both tracked points (t_s and t_b) – which were restated in three dimensional notation by adding the missing third coordinate from P_s and P_b to r_s and r_b – one can construct two lines $G_s(k) = t_s + k\,(f_s - P_s)$ and $G_b(l) = t_b + l\,(f_b - P_b)$ (Fig. 2.2 c). Ideally the trout was located at the transection of G_s and G_b. Due to noise and nonlinear image distortions this was rarely the case. An approximation of trout position is the center of the shortest distance between G_s and G_b (Fig. 2.2 c, circle).

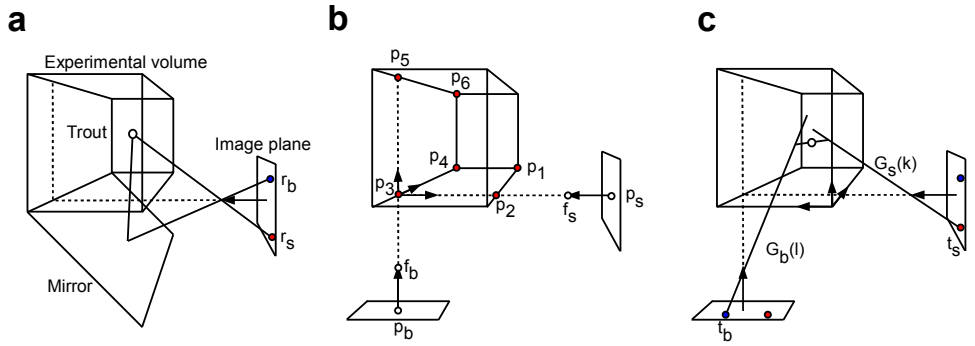

Figure 2.2: Camera calibration and 3-D reconstruction of trout position. A camera filmed the experimental volume from the side and from the bottom over a 45° mirror (b). To simplify calibration and reconstruction the mirror was mathematically eliminated by a coordinate transformation such that two virtual cameras, each for one of both views, were present (b). Points P_1 to P_6 were used to calibrate the virtual cameras. For each frame trout position was then estimated by the closest distance of two lines transecting the tracked trout positions on the image planes (r_s and r_b) and the focal points of the virtual cameras (f_s and f_b, c).

The size of the experimental volume (width $w = 28.5\,cm$, height $h = 29.3\,cm$ and length $l = 60\,cm$) and image coordinates of distinct points of the experimental volume (Fig. 2.2 b, red dots) were used to calibrate the camera by calculating f_s, f_b, P_s and P_b (Fig. 2.2 b). To simplify calculations a temporary origin was defined at the transection of both focus lines (Fig. 2.2 b stippled lines). Exemplary for the side view one can now formulate two equations with unknowns f_s and P_s:

$$\frac{F_s}{|\,P_2 - P_1\,|} = \frac{|\,P_s - f_s\,|}{|\,f_s\,| - w} \quad \text{and} \quad \frac{B_s}{|\,P_4 - P_3\,|} = \frac{|\,P_s - f_s\,|}{|\,f_s\,|} \tag{2.1}$$

with F_s and B_s defined as the distance on the image plane between points P_1 P_2 and P_3 P_4, respectively. For the bottom view points P_3, P_4, P_5 and P_6 were used accordingly to calculate f_b and p_b. Note that calculated trout positions were mirrored and translated such that the origin of the coordinate system was located as indicated in figure 2.2 c (arrows in the lower right edge point of the experimental volume while looking upstream). The three dimensional position of trout was then estimated by the centre of the nearest distance between both trajectories. EMG and video data were synchronized using a light trigger sequence. At each bulk flow velocity, EMG and video data were recorded for 4 hours, however, only the last 3 hours of an experiment were used for further analysis.

2.1.8 Post processing of data and statistics

EMG signals were amplified (Gain 4000x), band pass filtered (100 Hz to 3 kHz) and analogue to digital converted (CED Power 1401, 5 kHz). Data were post processed (Spike5) by applying a DC remove (1 s) and a sliding root mean square (RMS, 0.01 s) filter. To allocate the RMS EMG (rEMG) data to the frame rate of the camera, data were down sampled to 25 Hz. The rEMG data as well as positions of the fish were imported to MATLAB (v. 7.8.0). To normalize the rEMG data they were divided by their three hour mean. The volume of the working section was divided in 1 cm^3 cubes (voxels). For each frame in which the calculated trout position could be located inside a distinct voxel the number of stay (NS) was incremented by one and normalized rEMG (nEMG) values of both recordings were assigned to that voxel. The mean nEMG (mEMG) of each voxel was calculated by dividing the sum of all assigned nEMG values by NS. Assuming a uniform distribution of trout presence the expected value of NS (eNS) is $eNS = F / V$ with number of frames $F = 270000$ and number of voxels $V = 60 \text{ x } 28 \text{ x } 29\ cm^3$ inside the experimental volume. It was defined that trout preferred a voxel if NS was bigger than eNS and vice versa. The preferred volume was the sum of all preferred voxels. For each experimental run the number of voxels and the mean mEMG of all preferred and non-preferred voxels was calculated. Regressions as function of bulk flow velocity were calculated for parameters: mean muscle activity of preferred voxels, mean muscle activity of non-preferred voxels and volume of preferred voxels. According to the definition of voxel preference of a single experiment a region preference for all experiments of an experimental case (upstream and downstream) was defined with $eANS = N * F / V$ ($N = 20$, upstream case; $N = 18$ downstream case). NS of each voxel was added over all experiments resulting in aNS. In the upstream case a constant $k > 1$ was adjusted such that separable regions formed with $aNS > k * eANS$. Those regions were called preferred regions. Additionally the constant k was used to define over preferred voxels with $NS > k * eNS$. Regressions of mean muscle activity and volume of over preferred voxels as function of bulk flow velocity were calculated. Mean muscle activity of non-preferred regions and preferred region was calculated. Only muscle activities of regions which were explored more then k fold the expected number of stay were used for the comparison of regions. Note the difference of definition between voxel (volume) preference ($NS > k * eNS$, $k = 1$), voxel over preference ($NS > k * eNS$, $k > 1$) of single trout and region preference ($aNS > k * eANS$, $k > 1$) of all trout. Statistical tests were done with Sigma Plot 11.0.

2.1.9 Particle Image Velocimetry (PIV)

To visualize the flow profile next to and behind the cylinder a PIV analysis was performed. A laser sheet (Pegasus, 527 nm) was adjusted in the x-z-plane of the flow tank with y =15 cm. Seeding particles (PSP 50, Dantec Dynamics) were illuminated with the laser light. The flow up- and downstream of the cylinder was filmed with a high-speed video camera (Photron Ultima APX) operating at 500 frames per second (FPS). Flow vectors were computed with DaVis (LaVision). Image calibration was done using a two level calibration plate (Typ 20, LaVison).

2.2 Representation of unsteady flow in the MON of common rudd

2.2.1 Experimental Animals

34 common rudd, (*Scardinius erythrophthalmus*, Linnaeus 1758, body length (L = 6 - 9 cm) were used for the experiments. Rudd were purchased from a local dealer and held in 300 l aerated fresh water tanks equipped with a hideout and a filter pump. Fish were fed daily with fish pellets.

2.2.2 Surgical procedures

The rudd was caught with a glass and anesthetized with Tricain Methansulfonate (MS 222; c = 5 %; V=2.4 to 2.8 ml in 500 ml water). The fish was relaxed with an injection of Pancuroniumbromid (V = 50 - 100 μl; c = 3.3 %; Oragon Teknika) in both lateral muscles close to the dorsal fin. The fish was ventilated with fresh water through its mouth. Epidermis of the scull was local anesthetized with Xylocaine (v $\approx$ 50 μl; c = 2 %; AstraZeneca). To prepare the rudd for recordings from the MON the caudal part of the scull was opened (Dremel 400 Series Digital, 5000 - 330000 RPM and a scissor, 5 mm blades) such that the caudal part of the cerebellum and the dorsal part of the brain stem were visible. The cerebellum was pushed slightly away and fixated with wadding such that the MON was directly accessible.

2.2.3 Experimental set up

For experiments a custom-made circular flow tank (90 x 60 cm) with a working section (width 16 cm, height 13 cm, length 32 cm, water level 28 cm) was used (Fig. 2.3 a and b). Flow (PIV: 7 cm/s no cylinder, 2 cm/s downstream of cylinders; Particle tracking: 6 - 9 cm/s) was generated by a propeller (12 V Motor, 18 : 1, Modelcraft), located downstream of the working section. To avoid coarser-scale eddies, the water was directed through a colaminators up- and downstream of the working section. Two plates up- and downstream of the propeller were placed on the water surface to avoid surface waves. The flow tank was mounted with damping balls on a base frame. A damped table was surrounded by the base frame. After surgery, rudd were attached to and ventilated with a stainless-steel holder that consisted of a mouthpiece for artificial respiration with fresh water and two screws, which kept the head in a fixed position (Engelmann et al., 2002). The fish holder was mounted on the damped table (TMC). Additionally a three

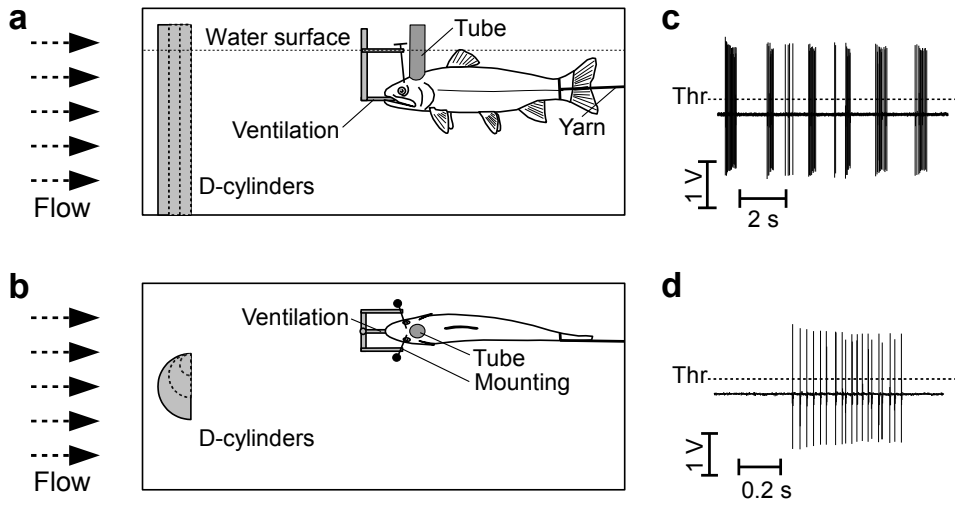

Figure 2.3: Side view (a) and bottom view (b) of the experimental set-up to record the neuronal activity in the MON of common rudd exposed to unsteady flow. Three D-shaped cylinders (1, 2 and 3 cm diameter) were successively placed upstream of rudd. Rudd were mounted on a fish holder and artificially ventilated. A tube, which was glued on the skull was filled with ringer to protect the underlying brain from swelling. Figure is not to scale. To separate spike times from recordings (c and d) a threshold (Thr) was defined for each unit.

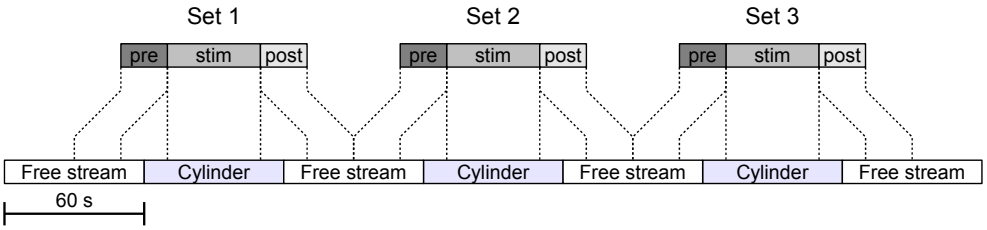

Figure 2.4: Succession of cylinder and non cylinder cases. Experimental cases were changed after 60 s of recordings. One experimental iteration consisted of a shuffled order of 3 cylinders. Between 60 s of cylinder presentation 60 s without a cylinder were presented. To exclude artifacts due to the exchange of cylinders 10 s before and after each experimental case were excluded from data analysis. Data snippets were ordered to 20 s of pre cylinder presentation (pre), 40 s of cylinder presentation (stim) and 20 s of post cylinder presentation (post).

axis micromanipulator (HS 6 manual) was mounted on the damped table. The micromanitpulator held a metal electrode (Dowben and Rose, 1953) and a head stage (DAM 80 Probe) for recordings. For PIV measurements a laser (green diode laser) was positioned lateral of the working section. A lense was used to spread a laser sheet horizontally. A high speed camera (Photron Ultima APX) was positioned on the bottom side of the flow tank and was adjusted orthogonal to the laser sheet.

2.2.4 Experimental procedures

The electrode was driven into the hindbrain ipsilateral of the stimulation side. Flow was present during the search procedure for units. Search stimuli were generated with a pipette which was moved through the experimental volume. If a unit was encountered it was tested for auditory and/or vestibulary input with knocks on the wall of the flow tank. If no auditory and/or vestibular inputs were present the stimulus protocol was started:

Three half cylinders (1, 2 and 3 cm) were used to generate vortex patterns. Half cylinders were positioned 5 cm upstream of the rudd. For a maximal stimulation strength cylinders were laterally placed such that the outer edge of the vortex street reached the rudd according to Chagnaud et al. (2007). Cylinders were successively placed in the working section (Fig. 2.4). At each cylinder representation neuronal activity was recorded for 60 s (stim). Between cylinder presentations the neuronal activity was recorded for 60 s without a cylinder (pre and post, cf. Fig 2.4). One repetition of the experiment consisted of a shuffled order of the three cylinders to avoid artifacts which may occur due to the sequence of cylinder presentation. A maximum of 5 experimental repetitions were conducted. If the recording was still stable spontaneous activity without flow was recorded.

During experiments, synchronous particle Image Velociometey (PIV) measurements were done to compare the flow field inside the field of view with the neuronal activity. Note that less PIV measurements than experimental repetitions were conducted due to the time it took to transfer the data from the high speed buffer to the computer (more than 8 min). For PIV measurements a high speed camera (Photron Ultima APX) filmed the experimental volume from below. A laser sheet (green laser) was adjusted on the hight of the lateral line canal such that the vortex street was visible with its alternating vortices in the camera image. The laser sheet illuminated seeding particles (PSP 50 μm, Dantec). The camera

filmed a field of view close to the fish with 1024 pixel in flow direction and 128 pixel orthogonal to the flow. A frame rate of 250 FPS was used. The buffer was capable to hold 16384 frames of PIV recording.

2.2.5 Data evaluation

Data acquisition and post-processing

Neuronal activity was amplified (1000x, DAM 80), notch filtered (50 Hz, notch filter build by Hendrik Herzog, Bonn) and recorded with an analogue to digital converter (CED Power 1401, 10 kHz) and the software Spike2 (Version 7.02). A threshold was defined for each recorded unit to separate spikes from noise. To higher the probability that single units were processed only units with inter spike intervals > 1 ms and similar spike forms in terms of amplitude and shape were used for further signal processing. Additionally only units with more than 1 repetition ($n > 1$) were further processed. To avoid artifacts which were caused from the mounting and demounting of cylinders 40 s were extracted out of each 60 s snippet (c.f. Fig 2.4). For statistical analysis sets of 20 s before the cylinder representation (pre), 40 s of cylinder representation (stim) and 20 s after the cylinder representation (post) were formed.

Spike rate analysis

The mean spike rate of pre, stim and post was calculated. For each unit a 2-way ANOVA (IBM SPSS Statistics 19, $\alpha = 0.05$, Bonferroni) was done on spike rates with factors cylinder size (1, 2, 3 cm) and stimulus type (pre, stim, post). Additionally three (pre, stim and post) linear regressions were calculated (SPSS) with cylinder size versus spike rate.

Spike pattern and frequency analysis

Spike pattern were analyzed. To do so a FFT was calculated over spike events (0.001 s rectangular kernel, 0.001 s bin width, 131072 bins) to extract the peak frequency. Spike intervals were also analyzed. To do so time delays (d) between spikes i and j were computed with $d_{ij} = t_j - t_i$ for M spikes with $i = 1, 2, \ldots, M-1$, $j = i+1, i+2, \ldots, M$ and time of appearance (t). Number of delays occurring each 100 ms were counted and plotted as function of time interval.

Correlation of spikes and PIV

High speed image data was calibrated (printed circuit board, raster distance 2.54 mm) and flow vectors were computed (multi pass, interrogation window 128 x 128 pixel² to 32 x 32 pixel², 50% overlap, post processing: smooth 3 x 3 pixel²) with DaVis (La Vision). Flow vector data was exported as text-files. The vector data was imported in MATLAB R2009a. Each imported text-file consisted the flow vectors of one time step. In MATLAB the data was sorted in form of time series at each position. A cross correlation over the time domain between spike events and flow vector components u, v and |u,v| was calculated for each vector position to achieve a spatial correlation strength map. The mean flow was calculated for overall images.

2.3 Lateral line canal morphology and signal to noise ratio

2.3.1 ALLCs equipped with ANs

ALLCs were equipped with artificial neuromasts (AN). To build artificial ANs (Klein, 2009; Klein and Bleckmann, 2011; Klein et al., 2011; Klein and Bleckmann, 2012), transparent silicon bars (Wacker Silicones, Elastosil RT 60) were fabricated and installed inside each ALLC segment (c.f. Fig. 2.5 a). For canal fluid motion detection, one end of each silicon bar was illuminated with an infrared light emitting diode (LED) (SFH420). Light, leaving the opposite end of the silicon bar, illuminated an optical fiber that was connected to a SMD photo-transistor (PT15) whose output was amplified (transistor BC547). A potentiometer (100 kΩ) was placed between the emitter of the transistor and the ground. Transistor output was fed into an AD converter (Power 1401, sampling rate 1 kHz) and stored on a computer (Optiplex 745, Dell). Pressure gradients between canal pores caused water flow inside the ALLCs that in turn deflected the silicon bars. In the absence of a stimulus, silicon bars were not vertically straight (0°) but slightly deflected to one side (at about 10°). The degree of deflection facilitated (flow in one direction) or reduced (flow in the opposite direction) the amount of light that reached the SMD photo-transistor. Thus, artificial CNs were direction sensitive.

The large size of the ANs (3-4 mm) made it necessary to built ALLC with a diameter = 4 mm). The ALLCs used for these measurements were composed of 3 parts. Part 1 housed the AN (Fig. 2.5 a). Part 2 was a PVC plate (Fig. 2.6 b) that was attached to part 1 (Fig. 2.6 a, b). A half canal was milled inside the PVC plate. Part 3 were mirror-inverted PVC plates of part 2 (Fig. 2.5 c) that contained, however, between 1 and 33 canal pores (Fig. 2.6 c). Part 3 not only differed in pore numbers but also in pore size and spatial pore configuration (Fig. 2.6). For measurements part 2 and one of the part 3 plates were screwed together such that they formed an ALLC (diameter 2 mm)(Fig. 2.6 a and b). By exchanging different types of part 3, different types of ALLCs were built. ALLC 1P had 1 pore with a diameter (d) of 1.5 mm. ALLC 5Pn: five narrowly spaced pores, d = 1.0 mm. ALLC 5Pw: 5 widely spaced pores, d = 1.0 mm. ALLC 9P: nine pores, d = 0.87 mm. ALLC 13P: 13 pores, d = 0.79 mm. ALLC 33P: 33 pores, d = 0.63 mm; ALLC 0P: no pores (c.f. Fig. 3). Pore size was adjusted such that identical pressure gradients caused identical volume flows at the AN. Note that the AN housed in part 1 measured the pressure difference between the two tubuli

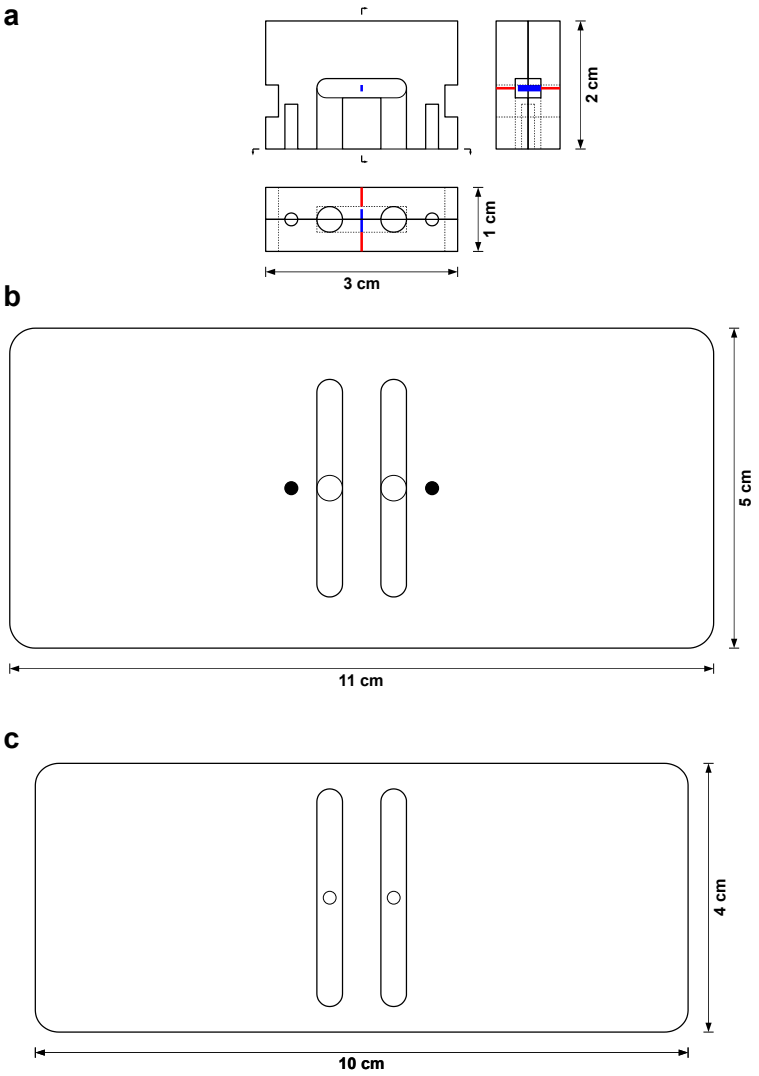

Figure 2.5: Parts which formed the artificial lateral line canal. Part 1 (a) housed the artificial neuromast. Part 2 (b) consisted of two drills (open circles) which connected two half canals with part 1. Part 3 (c) had two half canals which formed full canals together with part 2. Additionally part 3 had pore openings (open circles). In this figure part 3 had one pore opening at each side.

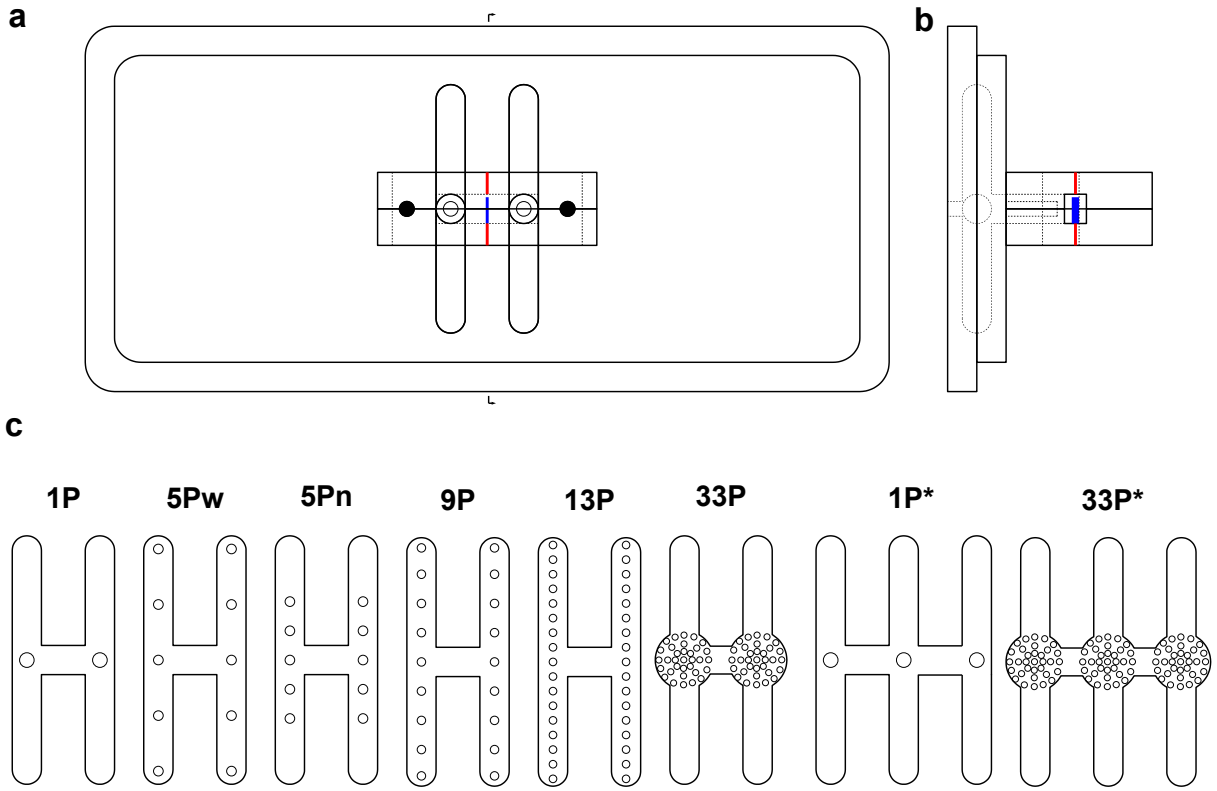

Figure 2.6: Assembled parts (a and b) and pore patterns (c). By exchanging part 3 (see Fig. 2.5) it was possible to test several pore patterns with a single artificial neuromast. Hereafter ALLCs were redrawn in simplified form (c).

(pore rows) of part 3. The volume flow through our ALLC was calculated according to the Hagen Poiseuile equation: $\dot{V} = pd^4\pi p/(128\eta l)$ with volume flow rate (V), diameter of tube (d) and length of tube (l). Assuming equal volume flow through N pores (which means V/N = const.) results: $\frac{N_1 p {d_1}^4 \pi p}{(128\eta l)} = \frac{N_2 p {d_2}^4 \pi p}{(128\eta l)} \Leftrightarrow \sqrt[4]{\frac{N_1}{N_2}} d_1 = d_2$ with number N_1 and diameter ${d_1}^4$ of reference pores and number N_2 and diameter ${d_2}^4$ of unknown pores. Using this relationship with $N_1 = 5$ and $d_1 = 1\,\text{mm}$ results for $N_2 = 1$ $d_2 = 1.495\,\text{mm}$, $N_2 = 9$ $d_2 = 0.863\,\text{mm}$, $N_2 = 13$ $d_2 = 0.788\,\text{mm}$ and $N_2 = 33$ $d_2 = 0.624\,\text{mm}$. Pore sizes of the ALLCs were not exactly identical with the calculated pore sizes because drills with a diameter that exactly matched the calculated values were not available. The drills chosen were such that the deviation between the calculated pore diameter and the pore diameter of the ALLC was $< 0.98\%$, i.e. the deviation in volume flow was at most 3.97%. Since a single AN can only provide information about the temporal variation of a signal, a two neuromast system can provide additional information about the spatial variation of the signal. Therefore in a second series of experiments, measurements were done with an ALLC that housed two ANs separated along the axis of the main canal by 1 cm. Part 2 and 3 were modified such that the ALLC had 6 tubuli. Two ALLCs were built. Tubuli had equal pore sizes and pore patterns than the tubuli of ALLCs 1P and 13P. The ALLCs with 2 ANs were termed ALLC 1P* and 13P* (Fig. 2.6 c). In all experiments sensor output was fed into an analog to digital converter (CED power 1401 mk2, sampling rate 1 kHz) and high pass filtered (0.1 Hz, Spike2).

2.3.2 Flow tank

The experimental series were conducted in a circular flow tank. The experimental volume of the working section of the flow tank was 34x15x10 cm^3. The respective ALLC was inserted into a plate such that the bulk flow in the tank remained undisturbed (Fig. 2.7 arrowheads). Bulk flow velocity was 9 cm/s.

2.3.3 Calibration

High-speed imaging (Photron Fastcam Ultima APX) was done to calibrate the displacement of the vibrating sphere. In the frequency range 10 to 80 Hz peak-to-peak displacement of the sphere was adjusted to a peak sphere velocity of 45 cm/s. Air bubbles, released at the bottom of the working section through hypodermic needles, served as a noise source. Two noise levels (noise 1 and noise 2) were introduced into the flow tank. To quantify the noise, air bubbles were

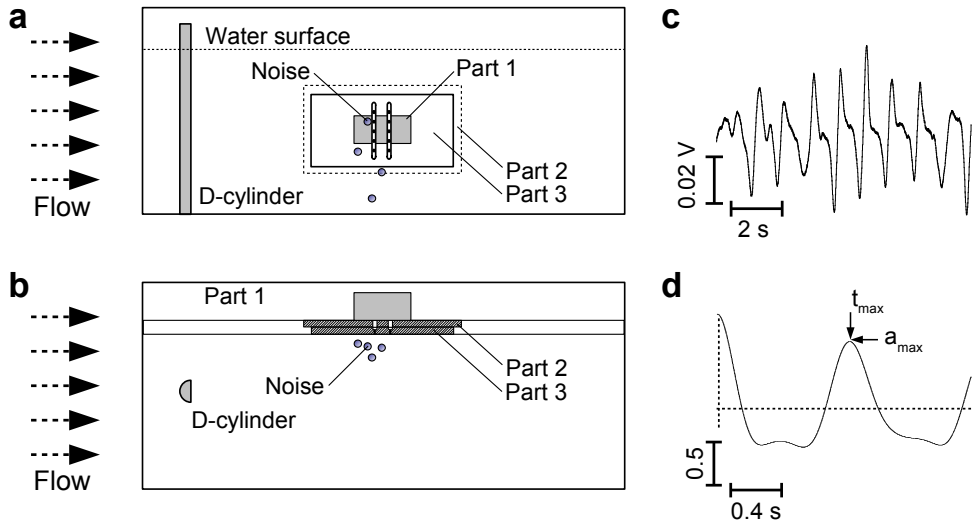

Figure 2.7: Set-up used to examine the influence of pore pattern on signal to noise ratio. Side view (a) and bottom view (b) of the experimental set-up. A D-cylinder (1 cm) was placed upstream of the ALLC which was attached to a plate. ALLCs with different pore patterns were used. Noise was generated with air bubbles. Additionally to the D-cylinder a vibrating sphere and a vibrating cylinder were placed in 1 cm distance in the center of the device (not shown) and used as signal sources. For instance a vortex street caused periodic output fluctuations of the AN (c). Autocorrelation (d) was used to find the main frequency component and self similarity of the measured vortex street signal (c).

illuminated and filmed (Photron Fastcam Ultima APX, 500 FPS, 2048 Frames) from the side under still water conditions. The number of air bubbles released per second was counted and air bubble sizes were measured (Photron Fastcam viewer 3.17). PIV was used to determine bulk flow velocity. For PIV a light sheet (IR laser 1W, 808nm, 808ILM1W, Dragon Lasers) was horizontally orientated and filmed from below (Photron Fastcam Ultima APX, 250 FPS).

2.3.4 Frequency response

To test the performance and frequency response of the ALLCs a vibrating sphere (diameter 1 cm, vibration axis parallel to the plate, vibration frequency 10 to 80 Hz, peak velocity 45 cm/s) was placed inside the experimental volume. This experiment, done with ALLC 1P, was conducted under still water conditions. In this experiment and in all following experiments measurements were done for 200 s and repeated 5 times. To take in to account a possible variation in signal output due to interchanging part 3, this part was detached and reattached between successive measurements.

2.3.5 Sensor output as function of pore pattern

A vibrating cylinder (diameter 1 cm, vibration frequency 4 Hz) was placed in 1 cm distance to the ALLCs. The sensor output was measured using ALLC 1P, 5Pn, 5Pw, 9P, 13P and 33P.

2.3.6 Vibrating sphere and noise

A vibrating sphere (diameter 1 cm, vibration axis parallel to the plate, vibration frequency 10 Hz) was placed in 1 cm distance to the ALLCs. The sensor output was measured using ALLCs 1P and 13P. ALLCs were tested with and without noise (noise level 2).

2.3.7 Vortex streets

A D-shaped cylinder (hereafter referred to as cylinder, diameter 2 cm), oriented vertically, was exposed to bulk water flow. The upstream distance between the cylinder and the center of the ALLCs (Fig. 2.7) was 1.5, 3.0, 6.0, 9.0 cm. The distance between the wall facing edge of the cylinder and the ALLC surface was 1 cm. For the measurements ALLC 1P and 13P were used.

2.3.8 Vortex street and noise

A cylinder (diameter 2 cm) was placed 6.0 cm upstream of the ALLC. The distance between the wall facing edge of the cylinder and the ALLC surface again was 1 cm. The sensor output was measured using ALLCs 1P, 5Pn, 5Pw, 9P, 13P and 33P. Measurements were done in running water and in running water contaminated with hydrodynamic noise (noise level 1 and 2). This experiment was repeated with noise level 1 and ALLCs 1P* and 13P*.

2.4 Optimization of an optical artificial neuromast for fabrication with MEMS

2.4.1 Simulation of fluid flow inside an artificial lateral line canal with respect to diminution size

To test the influence of diminutions on the flow velocity inside an artificial lateral line canal several canal forms were designed with Comsol 4.2. Simulated artificial lateral line canals consisted of two pore openings (r = 500 μm, Fig. 2.8 red and blue regions). The distance between centers of both pores was 5000 μm. A straight artificial lateral line canal expanded between both pores. The canal was 1000 μm wide, 5000 μm long and 500 μm high. Diminutions with different cross sectional sizes (Fig. 2.8 a, d = 100, 200, 300, 400, 500 and 1000 μm) were modeled in the middle of the lateral line canal. A tetrahedral mesh – consisting of over 3*10^5 to over 5*10^5 elements (100 μm to 1000 μm diminution) – was generated. A pressure difference of 0.01 Pa was applied between both pore openings. Maximum element size inside diminution was 30 μm. Maximum element size of the other fluid domains was 120 μm. Fluid flow was calculated with the fluid structure interaction (FSI) package of Comsol (4.2) in steady state analysis. Peak velocities in the middle of the lateral line canal were analyzed as function of diminution size. To examine the influence of the mesh size on the simulation result a second calculation was done with 300 μm diminution and a finer mesh (over 1.3*10^6 elements, 20 μm maximum element size of diminution and 60 μm maximum element size of the other domains).

2.4.2 Simulation of a bending silicon bar and fluid flow inside an artificial lateral line canal

After peak flow velocity was detected the underlying diminution size was used for a parameter scan of a bending silicon bar (0.001 GPa, Youngs modulus; 0.3 Poisson ratio, 1000 kg/m^3 density). The bar was sized 25 μm width and 460 μm hight. A parameter scan was conducted by altering the width of the bending bar (50, 100, 150, 200 and 250 μm). In a first step a tetrahedral mesh was generated for the bending bar. In a second step a tetrahedral mesh was generated for the fluid domain. The total mesh consisted of over 2.3*10^5 elements. A pressure difference of 1.0 Pa was applied between both pore openings. Fluid flow was calculated with the FSI package of Comsol (4.2) in steady state analysis. Peak displacement of the silicon bars was analyzed as function of bar width.

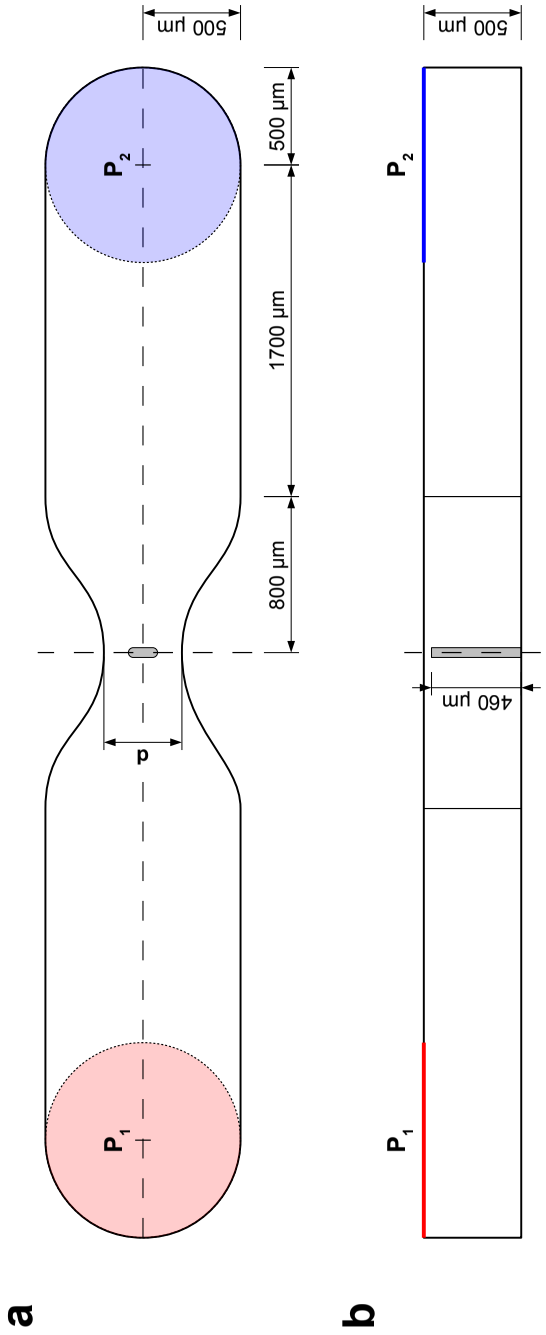

Figure 2.8: Geometry of simulated lateral line canal. The simulated lateral line canal had two (P_1, P_2) circular pore openings (a, top view, red and blue) located on the upper side (b, side view, red and blue). Diminutions with several diameters (d = 50, 100, 150, 200 and 250 μm) were tested with respect to peak flow velocity inside the center of the diminution. In a second step a diminution size of 300 μm was used together with a silicon bar (gray structure in a and b). Silicon bar width was altered to investigate its influence on bar deflection.

2.5 Improvement of production steps of optical artificial neuromasts

2.5.1 Sensor design

To improve optical artificial canal sensors in terms of reproducibility automatic fabrication and direction sensitivity the light amplification circuit (Fig. 2.9) was redesigned and arrays of bars with similar properties were used instead of hand made fiber glass mounted single bars. In contrast to a photo transistor a position sensitive device (PSD, OD3.5-6) was used for light detection. The current was amplified and differentiated with an operational amplifier (OP, TL 072). A high pass filter (0.034 Hz) was used to eliminate direct current (DC) offset. An additional inverting amplifier was used to further amplify the signal. Analogue to the IR LED of the hand made single sensor an 8 channel light emitting circuit (100 Ω and IR LED 805 HT) was developed with an inter diode distance of 5.08 mm. The circuit board layout with 8 channels was developed with the software eagle. The designed circuit boards (see Eagle Layouts in Appendix A) were industrial manufactured and populated with pick-and-place machines (Beta Layout, Aarbergen). Silicon sensor bar arrays with 8 bars in line were manu-

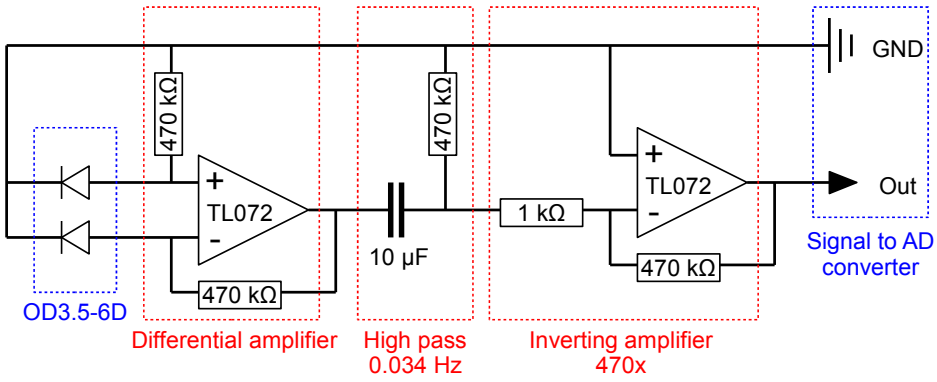

Figure 2.9: Light amplification circuit. For better performance a PSD was used and signals amplified with two operational amplifiers (OP TL 072). First the difference between both anodes of the PSD was done to reduce the DC shift caused by the light itself on the photo active area. Additionally the difference was amplified in this step. A high pass filter was used to eliminate the DC component followed by a second amplification step.

factured (method not shown due to patent application). The distance between adjacent sensor bars was 5.08 mm. Bar height was 2.6 mm. Bar width was 1 mm and bar thickness was 0.15 mm. Artificial lateral line canals as well as cavities for light emitting and light amplification circuit boards were milled into opaque

POV plates (see blueprints in Appendix A, production by workshop of caesar, Bonn). The circuit boards and the silicon bar array were assembled into the POV device. For electric insulation and water tightening electric components were molded in epoxy resin (UHU SCHNELLFEST) or (XOR-Giessharz, Casting resin, GLOREX, SWITZERLAND).

2.5.2 Analog to digital conversion and signal processing

Signals of the 8 channel sensor device were AD converted (CED Power 1401, 10 kHz). The AD converter was capable to measure between -5 and 5 V but the output of the light amplification circuit ranged between -9 and +9 V. To adjust the light amplification output to the input range of the AD converter a decoupling capacitor (10 μF) and a voltage divider with two 10 kΩ resistors were placed between the light amplification output and the input of the AD converter.

2.5.3 Test of the functionality of the artificial lateral line array

To test the performance of the artificial lateral line array it was submerged in the experimental section of a flow channel as used in part 2.3 and exposed to a vortex street caused by a 2 cm cylinder located 0 cm upstream ($v = 5.67 \pm 0.31$ cm/s, particle tracing, $\pm$ s.d.) of the sensor device. The cylinder was placed in 2 cm distance of a wall which hold the sensor device. Pores of the sensor device were planar with the wall to prevent self induced flow fluctuations which may occur when edges were present. A second performance test was done with two vibrating spheres (1 cm diameter, 50 Hz and 49.8 Hz) in still and running water with and without the presence of a 2 cm cylinder located 6 cm upstream in 2 cm distance to the wall which hold the sensor. The distance between both sphere centers was 1.2 cm and the distance to the artificial lateral line array was 2 cm. Note that in contrast to single sphere vibration two vibrating spheres with slightly different frequencies produce a non uniform signal (beating waves).

3 Results

3.1 The energy expenditure of trout exposed to unsteady flow

3.1.1 Validity of EMG recordings

Continuously swimming trout had a typical alternating activity of left and right swimming muscles (Fig. 2.1). EMGs of continuously swimming trout at the beginning of an experiment (Fig. 2.1 c) and the end of an experiment (after 4 hours, Fig. 2.1 d) were on equal scale in terms of activation pattern, mean amplitude and baseline noise. Note that rEMG values increased with increasing muscle activity (Fig. 2.1 e). Additionally rEMG values smoothed and rectified the EMG data. No alternating patterns were found in dead trout that were tied inside the Kármán gait region, i.e. recordings were not contaminated by artifacts.

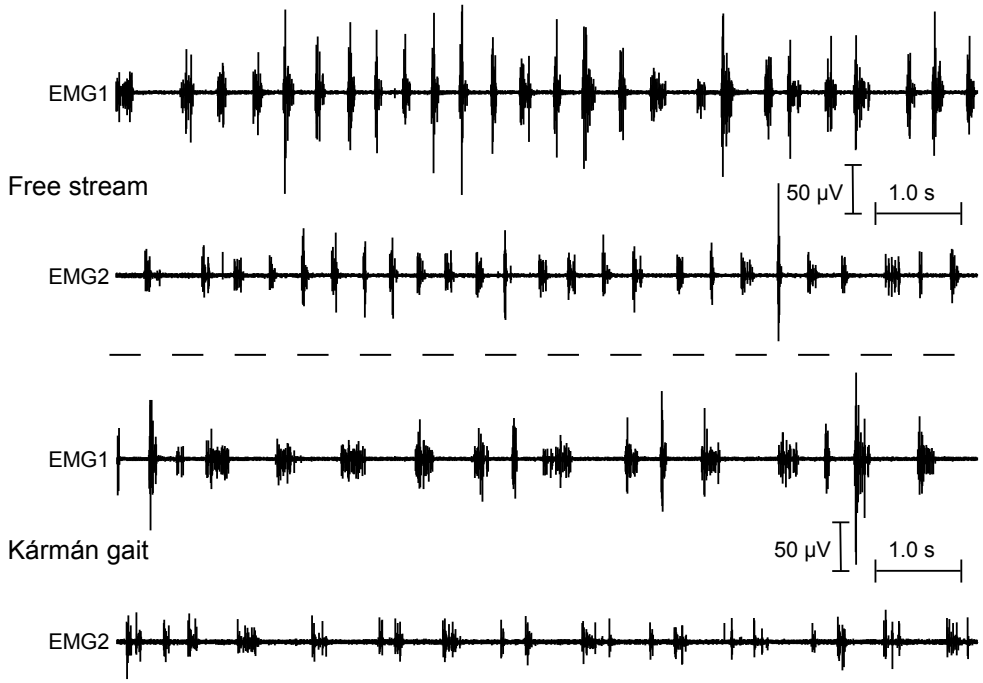

Figure 3.1: Muscle activity of both recording sides (EMG1 and EMG2) during swimming in the almost unhindered flow (a) and during Kármán gaiting downstream of the cylinder (b). Muscles were in both cases alternating active as expected. Note that muscles were longer active during Kármán gait with a lower amplitude than during free stream swimming.

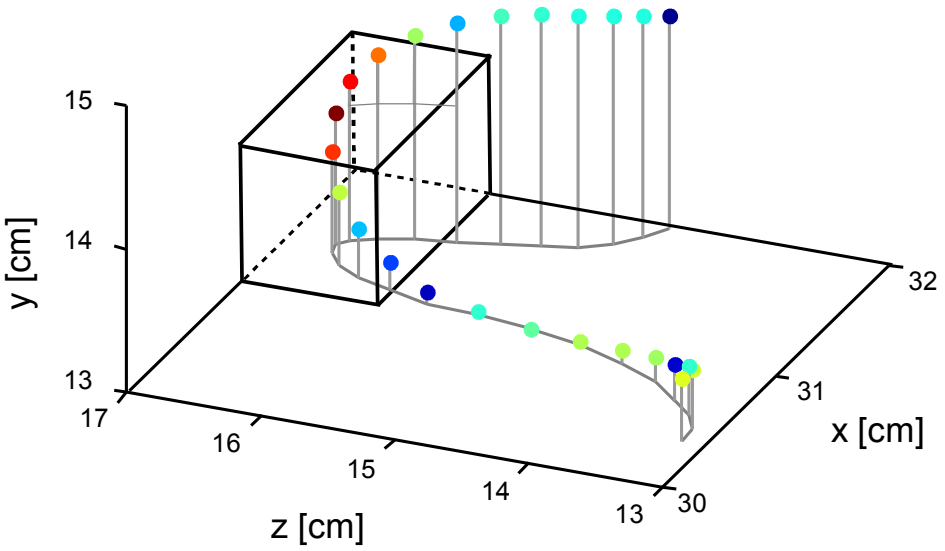

Figure 3.2: Muscle activity as function of space. The data shows a 1 s (25 frames) snippet of position of trout (dots) and color codet muscle activity (red: high muscle activity; blue: low muscle activity). The cube visualizes an 1 cm^3 voxel of the experimental volume. For each voxel the number of trout presence as well as mean muscle activity was calculated. Note that the data shows a trout during Kármán gaiting and that only one muscle recording (left muscle) is color coded.

3.1.2 Muscle activity as function of voxel preference

Single trout explored 15% ([10%, 29%], up. c.) and 9% ([7%, 14%], down. c.) of the total number of voxels (median, Q0.50 ([25% quartile, Q0.25, 75% quartile, Q0.75]) of all experiments of a single case. No correlation between flow velocity and explored volume was found (up. c.: $p = 0.532$, down. c.: $p = 0.244$). Proportion of voxels with NS > eNS was 6.2% ([3.1%, 9.6%], up. c.) and 2.9% ([1.5%, 4.3%], down. c.). Mean mEMG of preferred voxels – defined by NS > k * eNS (k = 1.0) – was 0.95 ([0.92, 0.98], up. c.) and 0.95 ([0.94, 0.97], down. c.). In contrast mean mEMG of non-preferred voxels was 1.99 ([1.55, 2.51], up. c.) and 2.32 ([1.75, 3.81], down. c.). No correlation of preferred volumes, mean mEMG of preferred volumes and mean mEMG of unpreferred volumes with bulk flow velocity was found in upstream case ($p = 0.714$, $p = 0.142$, $p = 0.163$). A correlation between preferred volumes, mean mEMG of preferred volumes and mean mEMG of non-preferred volumes with bulk flow velocity was found in downstream case. In downstream case the preferred volume decreased with increasing bulk flow velocity ($m = -7062.38$ [s / m] = -14.5 [% of total experimental volume* s / m],

Figure 3.3: Mean muscle activity as function of number of stay inside voxels of downstream experiments. Plots show data of all experimental iterations (horizontal) and velocities (vertical). Black markers indicate minimal and maximal muscle activity of voxels with equal number of stay. Mean muscle activity of voxels with the same number of stay decreased with increasing number of stay inside voxels (red line). Note that data is on double logarithmic scale.

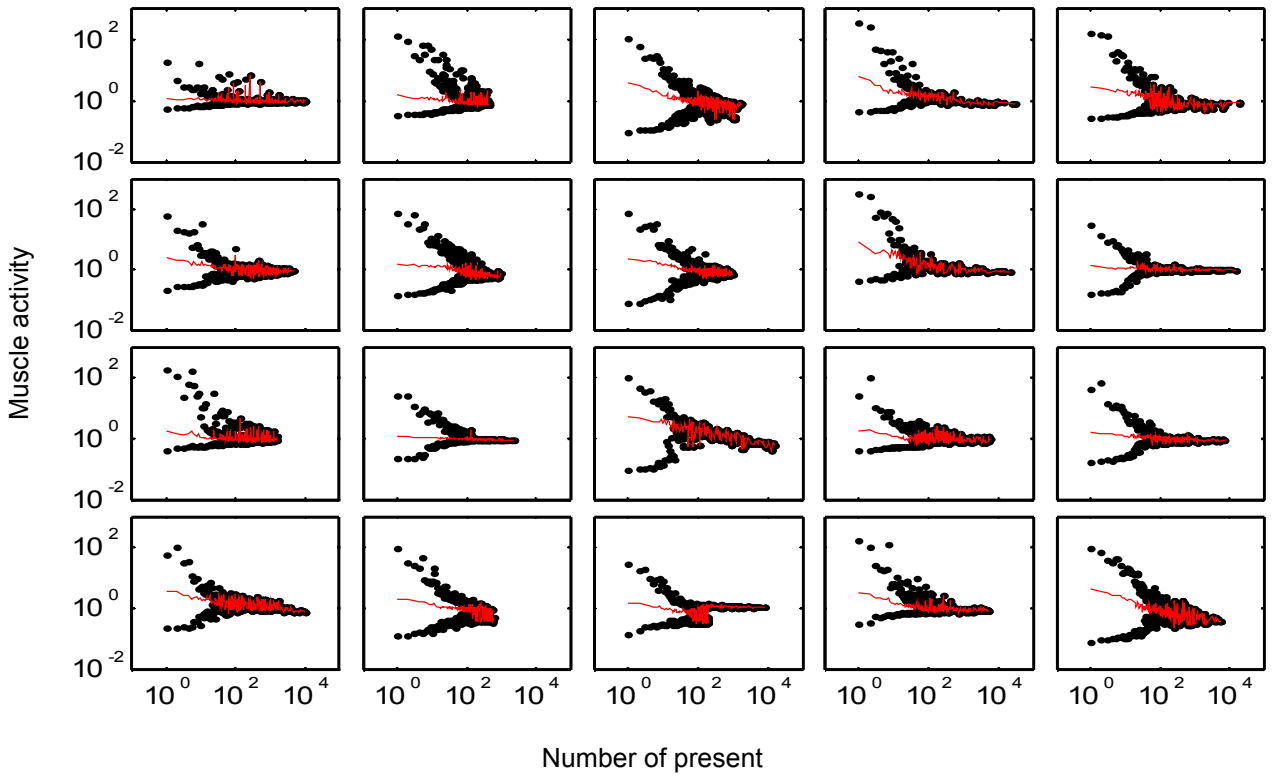

Figure 3.4: Mean muscle activity as function of number of stay inside voxels of upstream experiments. Plots show data of all experimental iterations (horizontal) and velocities (vertical). Black markers indicate minimal and maximal muscle activity of voxels with the same number of stay. Mean muscle activity of voxels with the same number of stay decreased with increasing number of stay inside voxels (red line). Note that data is on double logarithmic scale.

$p = 0.050$), mean mEMG of preferred volume decreased with increasing bulk flow velocity ($m = -0.30$ [s / m], $p = 0.003$) and mean mEMG of non-preferred volume increased with increasing bulk flow velocity ($m = 14.97$ [s / m], $p = 0.002$). Mean mEMG of preferred volumes differed from mean mEMG of non-preferred volumes (up. c.: $p < 0.001$, down. c.: $p < 0.001$, rank sum test). Note that in most experimental cases muscle activity decreased with increasing region preference (Figs. 3.3 and 3.4).

3.1.3 Kármán gait, entraining, wave mode and bow wake

During upstream case experiments $k = 3.8$ lead to four separable 3-dimensional regions inside the experimental volume characterized by $aNS > k * eANs$. One Kármán gait region (Figs. 3.1, 3.7, 3.9 b and 3.10 b), 2 entraining regions (Figs. 3.6, 3.9 b and 3.10 b) and a wave mode region (Figs. 3.5, 3.9 b and 3.10 b) were found. Since in these experiments the cylinder was placed close to the upstream net trout were not able to use the bow wake zone for station holding. Both entraining regions had a cylindrical volume (606 voxels, 1.2% of the total volume) with the center located 4 cm left or right and 10 cm downstream of the cylinder (Figs. 3.9 and 3.10). In addition to the two entraining regions, trout preferred a spherical volume (146 voxels, 0.3% of the total volume) whose center was located 6 cm downstream of the cylinder and 21 cm above the bottom of the flow tank (wave mode). The Kármán gait region was located in the center of the flow tank, as expected (Liao et al., 2003a). This zone had a prolate ellipsoid volume (932 voxels, 1.9% of the total volume). When the cylinder was placed close to the downstream net trout preferred three distinct regions (Figs. 3.9 and 3.10). Two spherical volumes (105 voxels, 0.2% of the total volume) close to the downstream net at the bottom of the flow tank and one cylindrically shaped volume (433 voxels, 0.9% of the total volume) in front of the cylinder (bow wake region, Figs. 3.8, 3.9 a and 3.10 a). Figures 3.5, 3.7 and 3.6 show data of three representative experimental runs for the upstream case. Note that the mEMG values were lowest where the probability of presence was highest (Figs. 3.5, 3.7 and 3.6, compare a and b). Trout spend 10^3 to 10^4 frames (proportion of presence: number of frames inside voxel / total images; $3.7 * 10^{-3}$ to $3.7 * 10^{-2}$) inside preferred voxels (Figs. 3.5 a, 3.7 a and 3.6 a). With increasing distance to preferred voxels, the number of frames a trout spend inside a voxel decreased. Note that the decrease was more than two orders of magnitude over a distance of 5 cm.

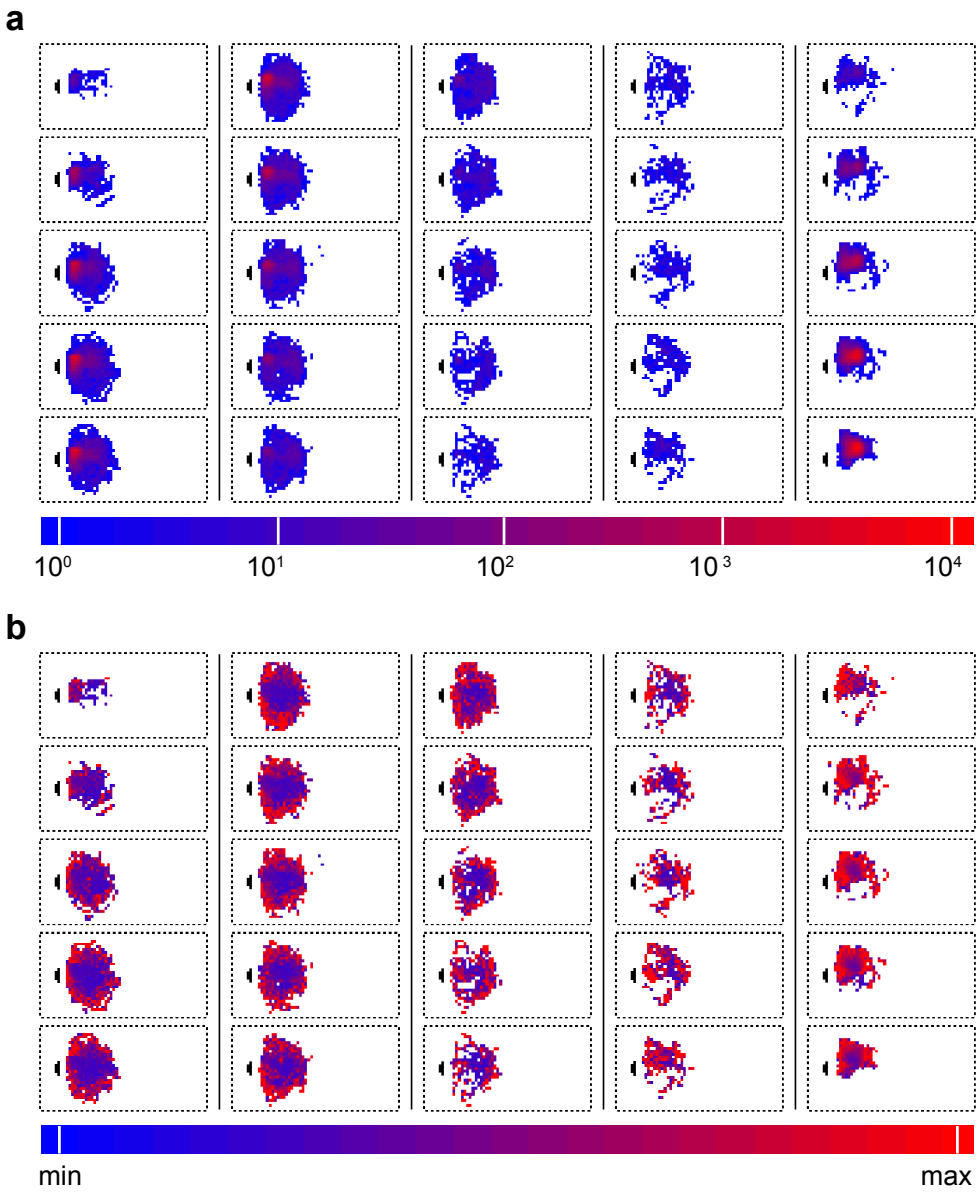

Figure 3.5: Number of stay (a) and muscle activity (b) of trout showing wave mode (WM) behavior as function of place. Red regions in a indicate high region preference whereas red regions in b indicate a high muscle activity. Note that region preference is on logarithmic scale and muscle activity was minimal in preferred regions.

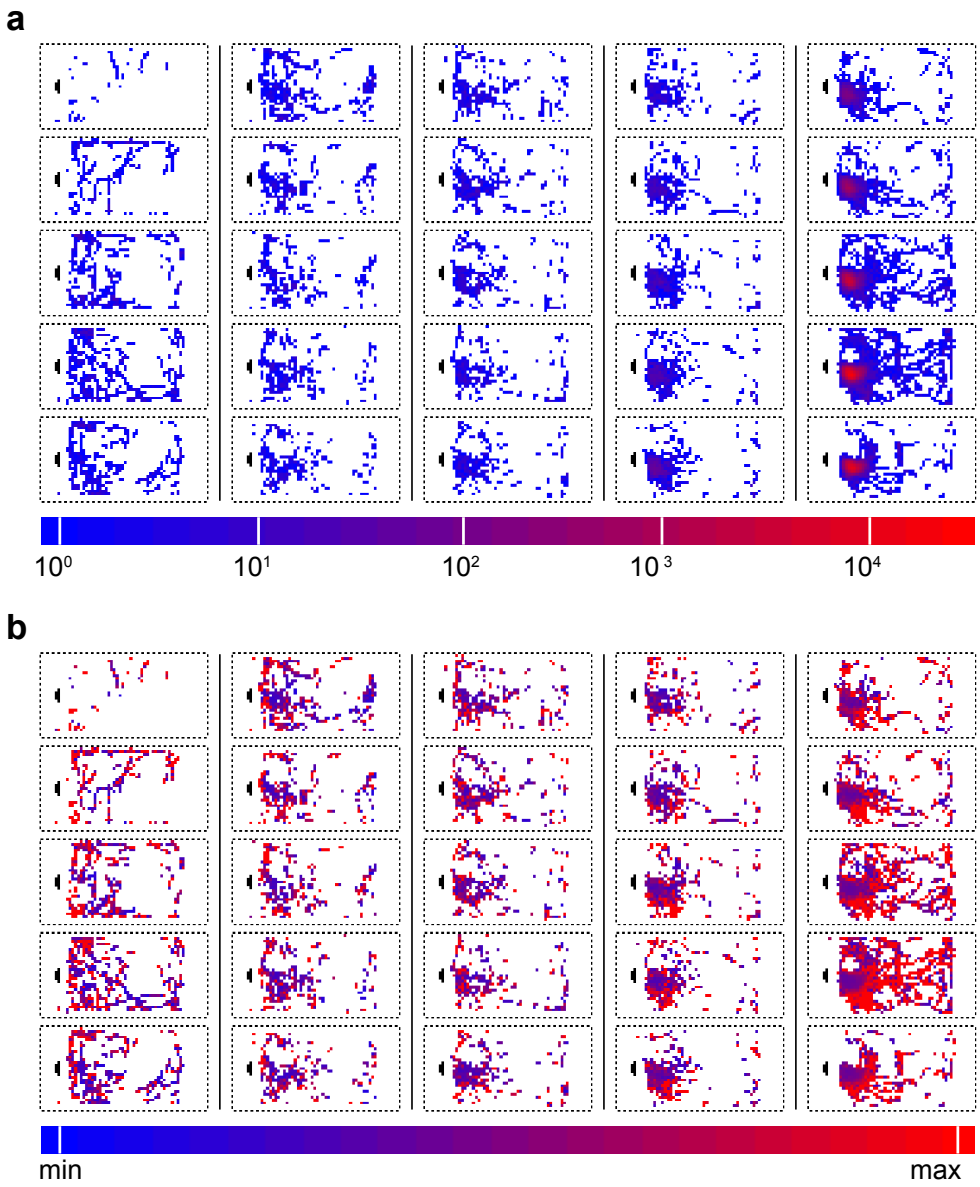

Figure 3.6: Number of stay (a) and muscle activity (b) of trout showing entraining (EN) behavior as function of place. Red regions in a indicate high region preference whereas red regions in b indicate a high muscle activity. Note that region preference is on logarithmic scale and muscle activity was minimal in preferred regions.

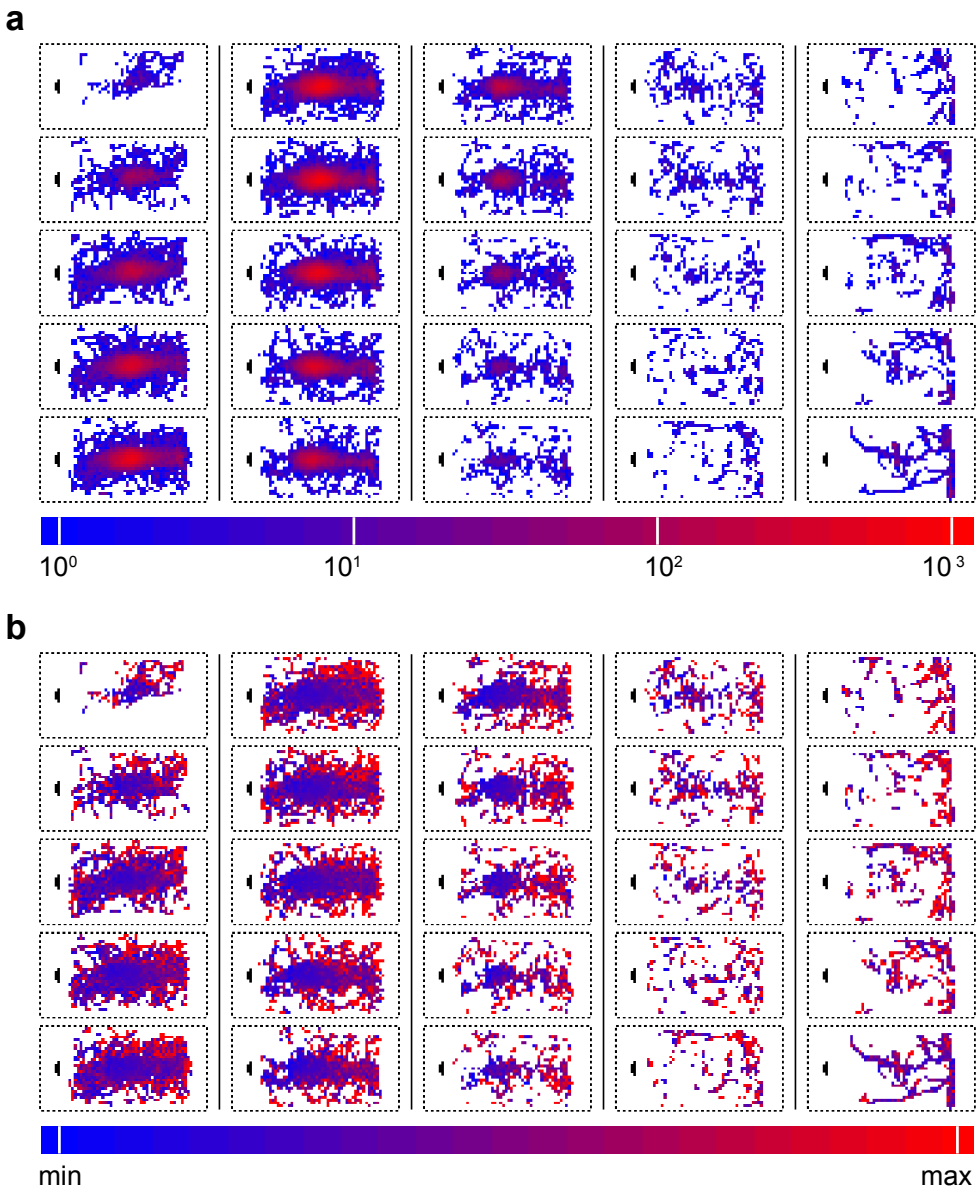

Figure 3.7: Number of stay (a) and muscle activity (b) of trout showing Kármán gait (KG) behavior as function of place. Red regions in a indicate high region preference whereas red regions in b indicate a high muscle activity. Note that region preference is on logarithmic scale and muscle activity was minimal in preferred regions.

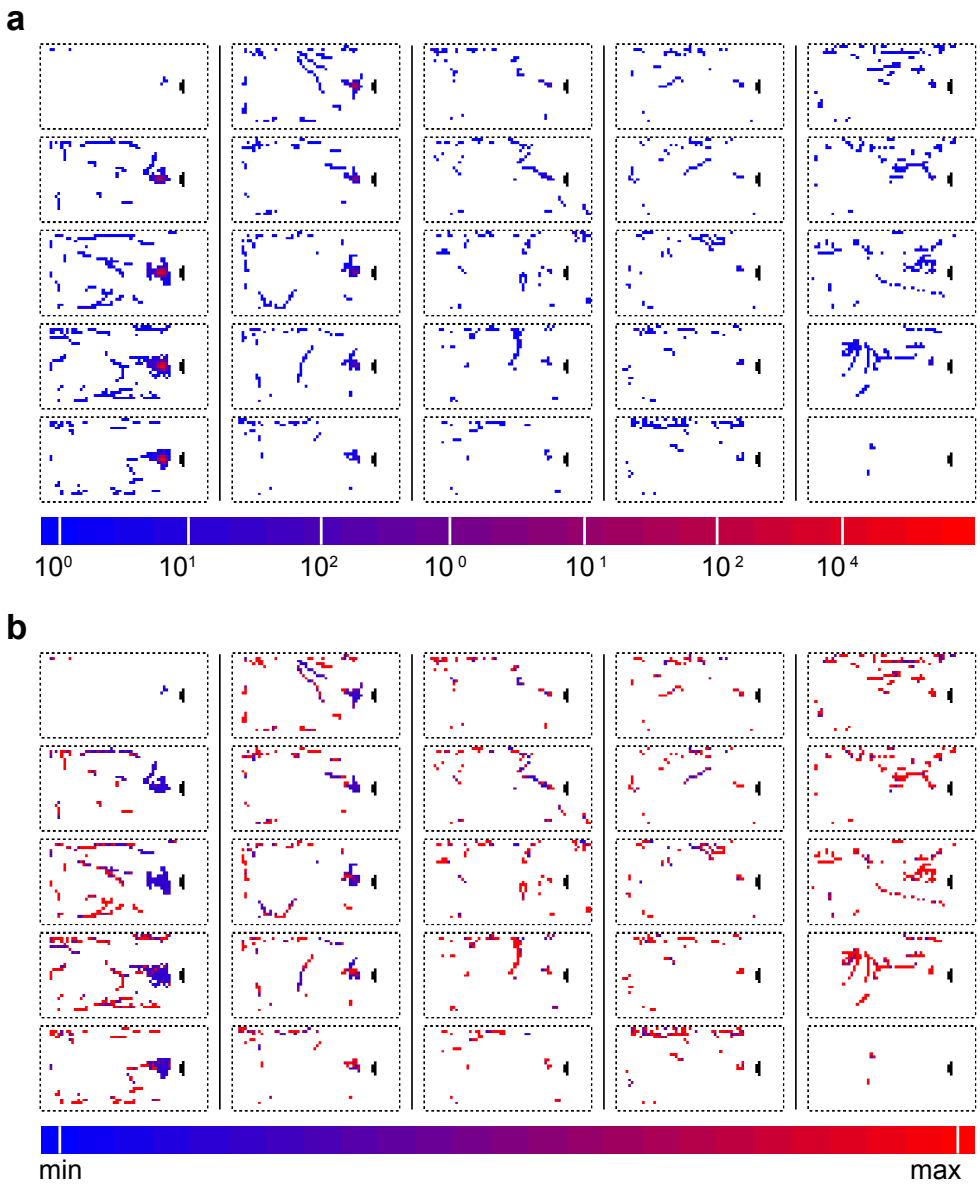

Figure 3.8: Number of stay (a) and muscle activity (b) of trout showing bow wake (BW) behavior as function of place. Red regions in a indicate high region preference whereas red regions in b indicate a high muscle activity. Note that region preference is on logarithmic scale and muscle activity was minimal in preferred regions.

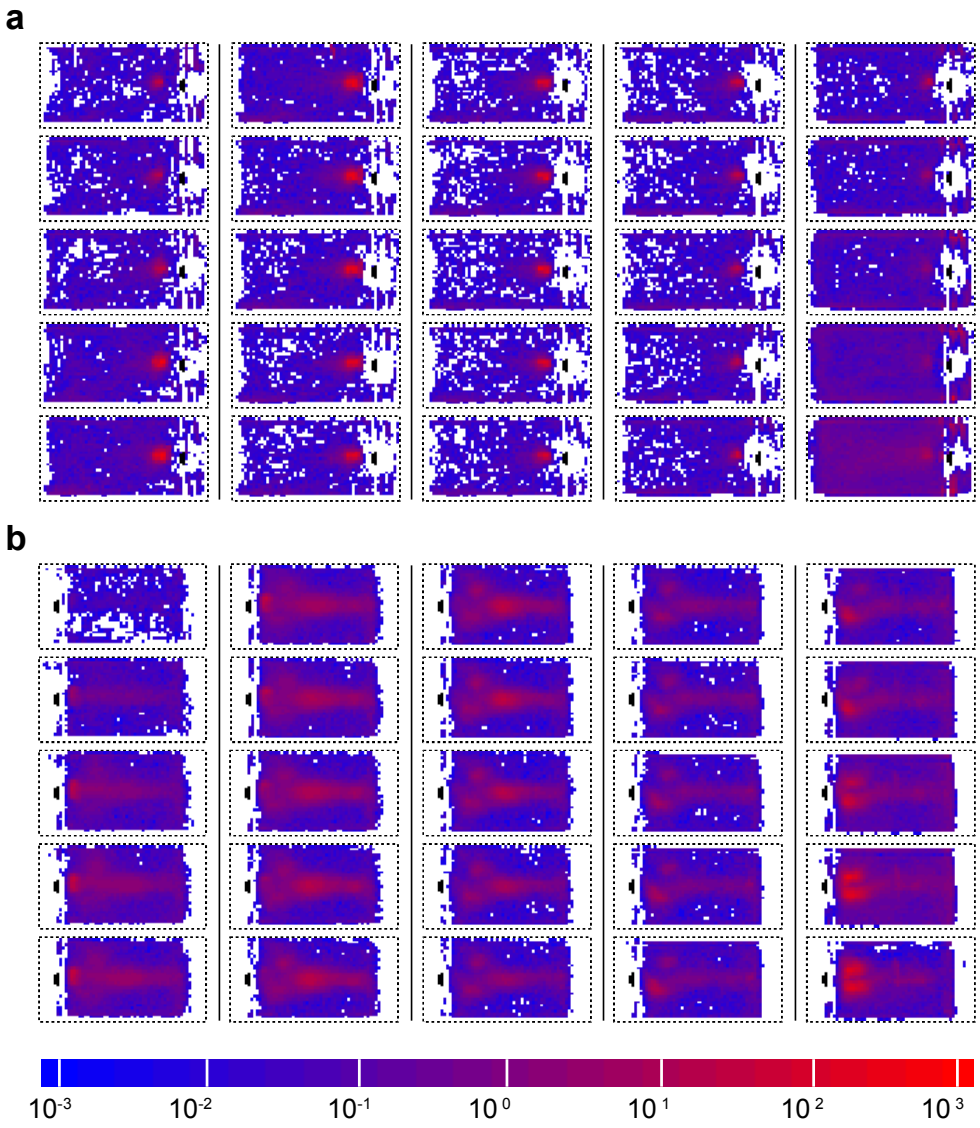

Figure 3.9: Cumulated number of stay as function of place during up- (a) and downstream (b) experiments. Red regions indicate a high region preference and blue regions a low region preference. Note that region preference is on logarithmic scale. Animals preferred distinct regions in the experimental volume. The relation between bow wake (a), Kármán gait, Entraining and wave mode (b) is visible. Note that preferred regions had curved 3-D structures.

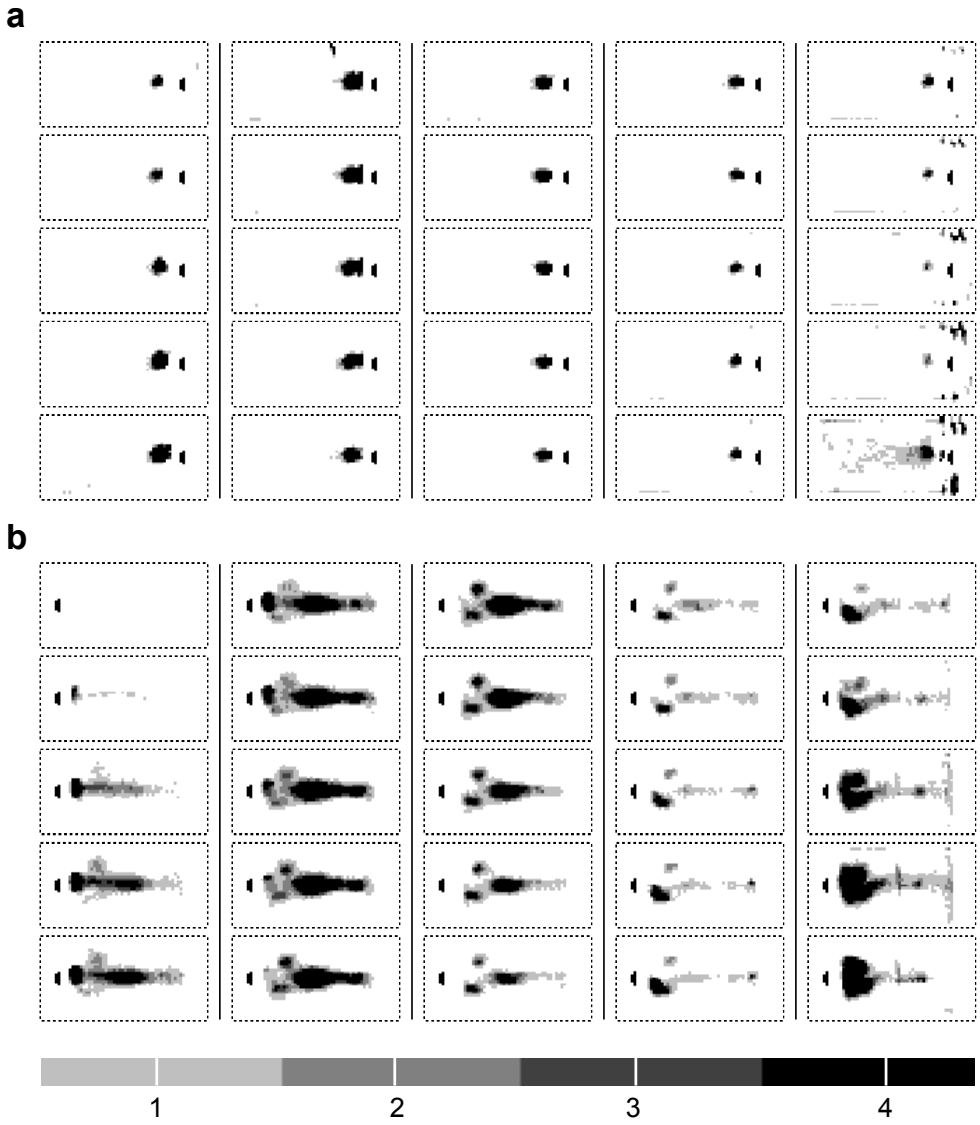

Figure 3.10: Region preference in terms of k as function of place during up- (a) and downstream (b) experiments. White regions indicate non-preferred regions and regions which have not been explored by trout. The color bar encodes k for plotted values aNS > k * eANS. This means that gray scaled voxels were explored more than k fold of the expected number of stay from a uniform distribution. Note that preferred regions had curved 3-D structures. In this work k = 3.8 resulted in separable preferred regions of Kármán gait, entraining and wave mode in upstream case.

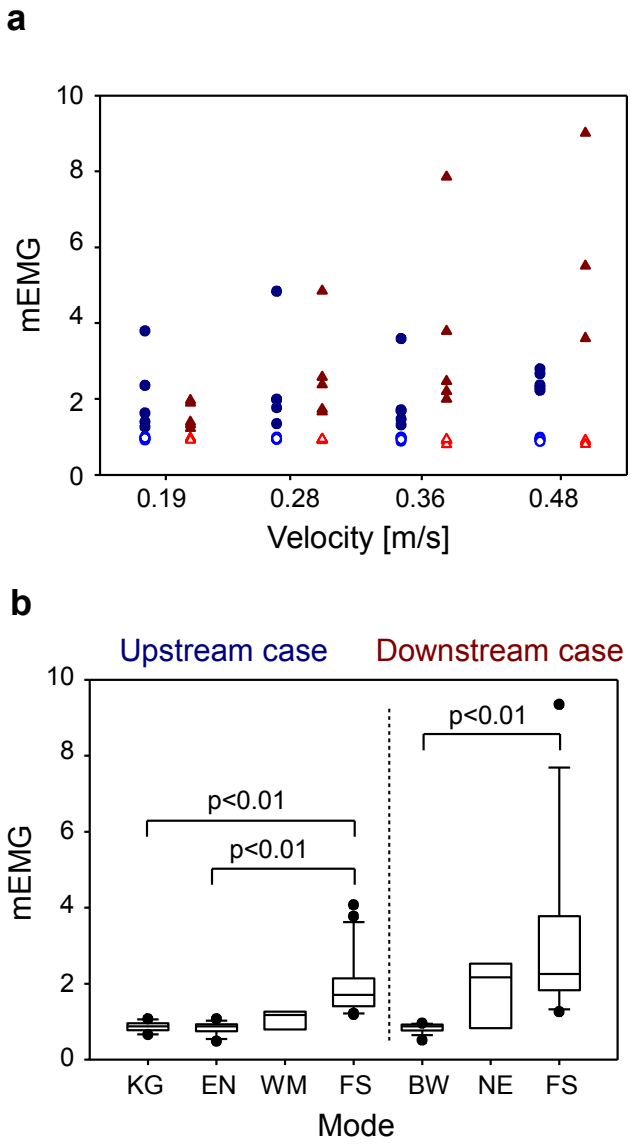

Figure 3.11: Mean muscle activity as function of flow velocity (a) and region (b). Mean muscle activity inside over preferred regions (a, open symbols) was always below mean muscle activity inside non-preferred regions (a, closed symbols) during up- (circles) and downstream (triangles) case. Muscle activity in non-preferred regions increased with increasing bulk flow velocity ($m = 14.98$, $p = 0.002$) in downstream case whereas no increase was found in upstream case ($m = 0.88$, $p = 0.666$). Muscle activity in over preferred regions ($NS > k * eNS$, $k = 3.8$) increased with increasing bulk flow velocity ($m = 0.419$, $p = 0.032$) in downstream case whereas no increase was found in upstream case ($m = -0.181$, $p = 0.163$). Muscle activity during Kármán gait (b, KG) and Entraining (EN) was significantly different to the muscle activity inside non-preferred regions (FS). No difference was found for the wave mode region (WM). Trout inside bow wake region (BW) showed significantly reduced muscle activity compared to trout inside non-preferred regions (FS). No significant difference was found for the net region (NE).

In all upstream experiments trout stayed at least one frame inside the Kármán gait region and inside the entraining region. The wave mode region was explored in 17 out of 20 cases. In 10 out of 20 experimental runs trout stayed more frames inside the Kármán gait region as expected from the uniform distribution (data of one fish shown in Fig. 3.7 b). In 14 out of 20 this was the case for the entraining region (data of one fish shown in Fig. 3.6 b) and in 5 out of 20 the case for the wave mode region (data of one fish shown in Fig. 3.5 b). In 13 out of 20 (upstream case) and 11 out of 18 (downstream case) experimental runs trout preferred only one region. In other cases more than one region was preferred. In the upstream case trout preferred Kármán gaiting (50%), entraining (70%) and wave mode swimming (25%). Wave mode swimming was observed in five experimental runs (upstream case) and only at high flow velocities (0.36 and 0.48 m/s). In the downstream case trout preferred swimming in the bow wake region (100%) and in regions that were close to the net (39%). Muscle activity in non-preferred regions ($NS < k * eNS$, $k = 1.0$) increased with increasing bulk flow velocity ($m = 14.98$, $p = 0.002$, linear regression, Fig. 3.11 a) in downstream case whereas no increase was found in upstream case ($m = 0.88$, $p = 0.666$). Muscle activity in over preferred voxels ($NS > k * eNS$, $k = 3.8$) increased with increasing bulk flow velocity ($m = 0.419$, $p = 0.032$) in downstream case whereas no increase was found in upstream case ($m = -0.181$, $p = 0.163$). The mEMG was significantly ($p < 0.01$, ANOVA on ranks, Dunns) lower in Entraining region and Kármán gait region than in non-preferred regions (Fig. 3.11 b). No difference of mean mEMG between Kármán gait, entraining and wave mode region ($p > 0.05$) as well as no difference between Wave mode region and non-preferred regions ($p > 0.05$) was found. The mEMG was significantly ($p < 0.01$, ANOVA on ranks, Dunns) lower in bow wake region than in non-preferred regions and net regions (Fig. 3.11 a). No difference of mean mEMG between net region and non-preferred region ($p > 0.05$) was found.

3.1.4 Muscle activity pattern during Kármán gaiting

The data of a representative experimental run indicate that the curvature of the horizontal (z-axis) locomotion during Kármán gaiting was almost sinusoidal (Fig. 3.12 a). Both recordings of the left and right muscle showed activity during a Kármán gait cycle. Mean activity of both recordings was phase locked (0° and 180°) with the horizontal curvature of the Kármán gait cycle (Fig. 3.12 a, b). The peak frequency of the horizontal locomotion during Kármán gaiting increased with increasing flow velocity (Fig. 3.13, bars). Additionally the peak frequency of high pass filtered (rEMG subtracted by mEMG) muscle activity was coincident with the peak frequency of horizontal locomotion (Fig. 3.13, solid line).

3.1.5 Particle image velocimetry

Bulk flow velocities (laser sheet at y = 15 cm, field of view = 15.5 x 15.5 cm^2) were 0.19 [0.18, 0.20], 0.28 [0.27, 0.28], 0.36 [0.36, 0.37] and 0.48 [0.47, 0.49] m/s (Q0.5 [Q0.25, Q0.75] of vectors inside the field of view). The submerged cylinder caused a Kármán vortex street at each bulk flow velocity. Vortex shedding frequencies were 0.88, 1.24, 1.47 and 2.19 Hz. Maximum mean velocities (0.28, 0.44, 0.55 and 0.70 m/s) occurred next to the cylinder. The mean flow velocity was reduced inside the bow wake, Kármán gait and wave mode region (Fig. 3.14). Flow fluctuations (RMS) were largest inside the Kármán gait region and almost zero inside the bow wake and entraining region (Figs. 3.15 and 3.16).

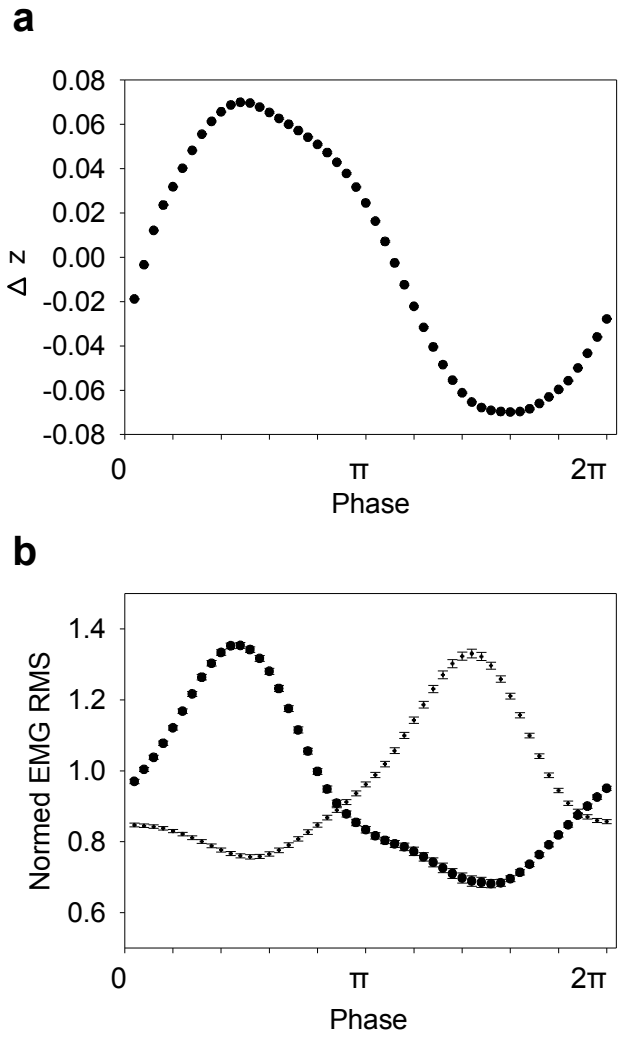

Figure 3.12: Vertical oscillation of fish position (a) and oscillation of muscle activity (b) during Kármán gait. The curvature of vertical position was almost sinusoidal. Left and right muscles showed similar oscillations. Note that muscles were alternating active.

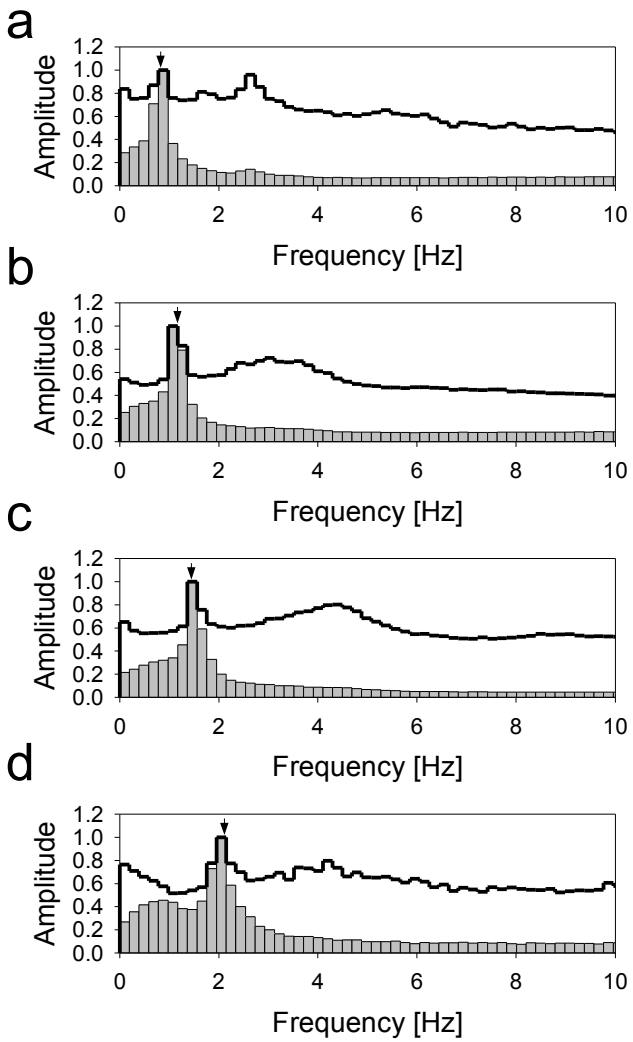

Figure 3.13: Frequency spectrum of curvature of vertical position and muscle activity during Kármán gait. Peak frequency of muscle activity coincide with peak frequency of curvature of vertical position. Note that peak frequency of vertical fluid flow (arrows) also coincide with peak frequency of muscle activity.

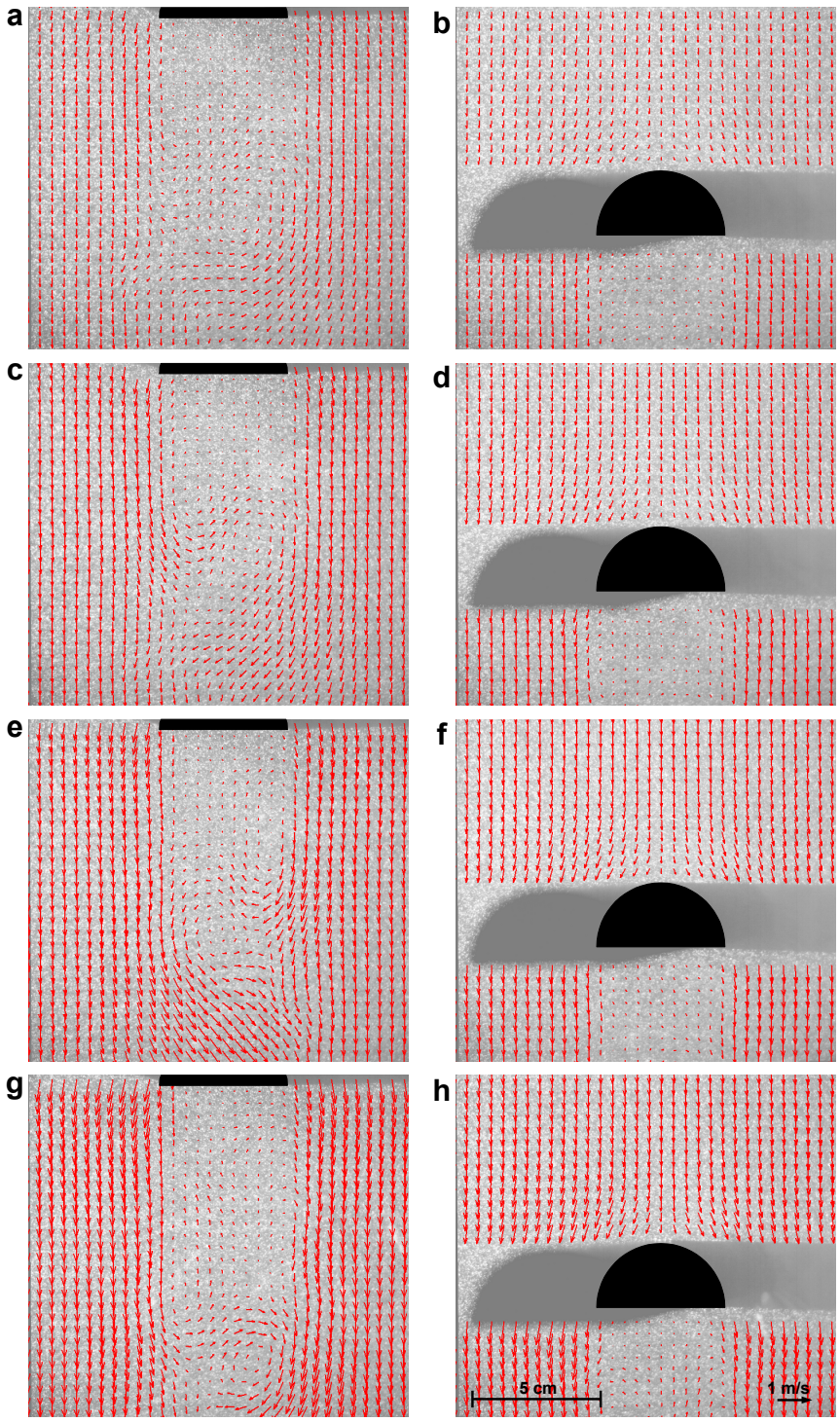

Figure 3.14: Flow caused by a 5 cm cylinder at 0.19 (a and b), 0.28 (c and d), 0.36 (e and f) and 0.48 m/s (g and h) at one point in time. Flow was almost laminar in front of the cylinder (b, d, f and h) at all flow velocities and decelerated in the bow wake region. Vortices were visible downstream of the cylinder (a, c, e and g). Note that the downstream distance of the vortex shedding region increased with increasing bulk flow velocity.

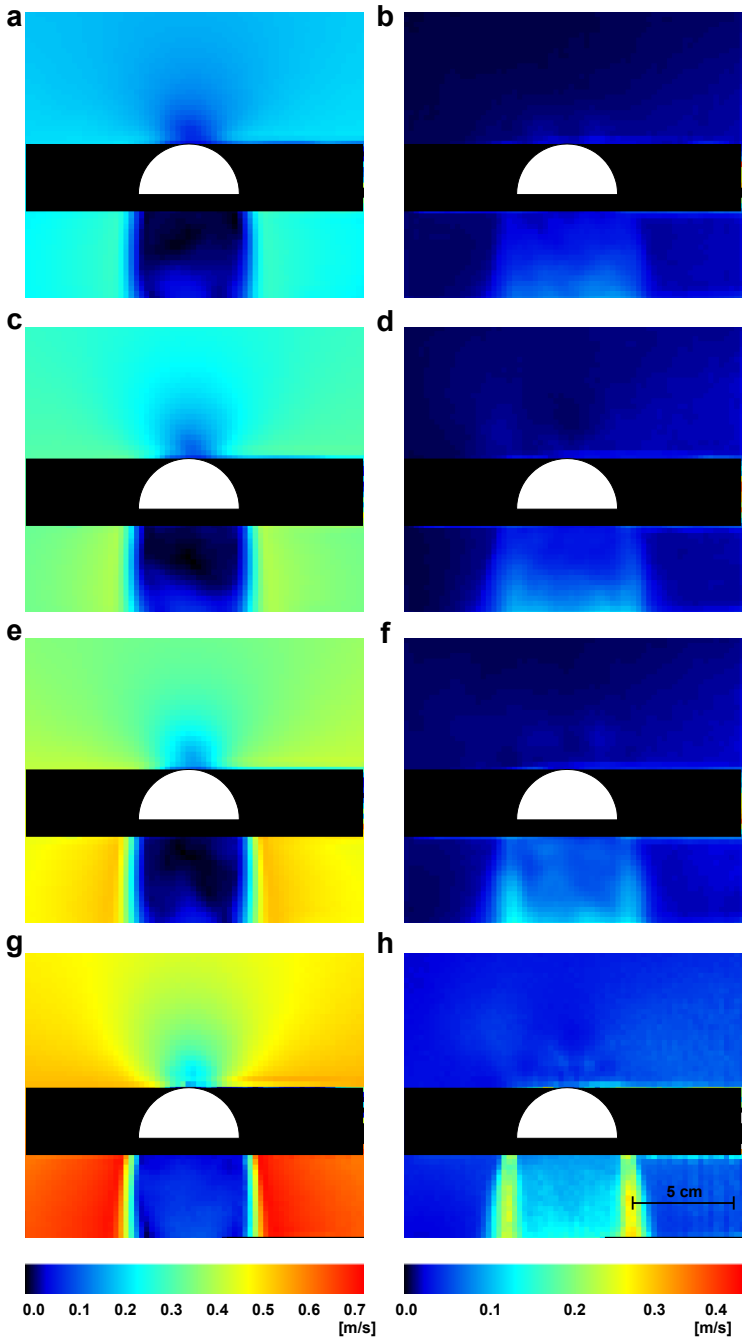

Figure 3.15: Mean flow magnitude (a, c, e and g) and RMS of flow magnitude (b, d, f and h) of the bow wake region. Bulk flow velocity was 0.19 (1 and b), 0.28 (c and d), 0.36 (e and f) and 0.48 m/s (g and h). Flow magnitude in front of the cylinder and in the suction zone behind the cylinder was lowest. Flow magnitude next to the cylinder was highest. RMS as indication for flow fluctuations was lowest in front of, next to and in the suction region of the cylinder whereas RMS was highest inside the vortex shedding region (not shown) and transition region from accelerated flow next to the cylinder towards the suction region.

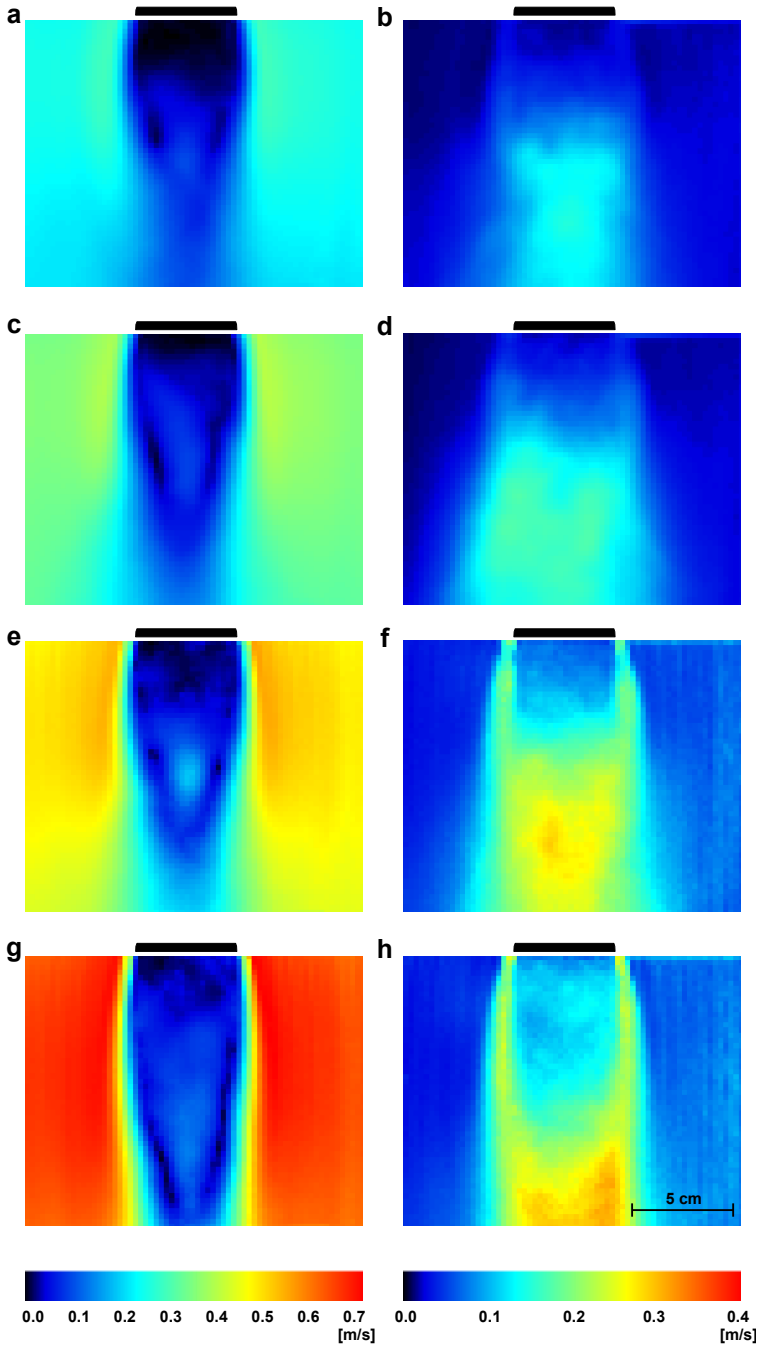

Figure 3.16: Mean flow magnitude (a, c, e and g) and RMS of flow magnitude (b, d, f and h) of Kármán gait and Entraining regions. Bulk flow velocity was 0.19 (1 and b) , 0.28 (c and d), 0.36 (e and f) and 0.48 m/s (g and h). Flow magnitude next to the cylinder was highest and reduced in the suction region downstream of the cylinder. RMS as indication for flow fluctuations was lowest next to the cylinder whereas RMS was highest inside the vortex shedding region and transition region from accelerated flow next to the cylinder towards the suction region.

3.2 Representation of unsteady flow in MON of common rudd

3.2.1 Unit overview

During this work 73 units were recorded from 34 rudd. 31 units with $n \geq 2$ iterations were further processed and used for spike rate and pattern analysis. Additionally one unit with $n < 2$ iterations was used in the PIV part of the spike pattern analysis. Three or more experimental iterations were conducted with 26 units (Fig. 3.24 a). Spike rates were during pre condition between 0.100 and 11.100 (min, max, mean = 3.141, Q0.25 = 0.787, Q0.50 = 2.250, Q0.75 = 4.710) spikes per second (S/s), during stim condition between 0.23 and 12.76 (min, max, mean = 4.569, Q0.25 = 1.603, Q0.50 = 3.590, Q0.75 = 6.992) S/s and during post condition between 0.03 and 16.10 (min, max, mean = 3.141, Q0.25 = 0.690, Q0.50 = 2.010, Q0.75 = 4.270) S/s. Spike rate of all recorded units increased with increasing cylinder diameter (m = 0.762 [S/s], p = 0.001). Spontaneous rates were between 0.24 and 13.06 (12 of 31 units, min, max, mean = 2.85, Q0.25 = 0.45, Q0.50 = 1.17, Q0.75 = 4.15). Note that Q0.75/Q0.50 = 2.09 (pre), Q0.75/Q0.50 = 1.95 (stim) and Q0.75/Q0.50 = 2.12 (post). Due to the variation among all units single unit analysis was done with respect to spike rate and pattern. In the following two subsections detailed results of 6 units were shown. Note that all other units reacted on the cylinder stimulus less than those 6 units in terms of spike rate and spike pattern and that recorded units showed a mostly continuous reaction spectrum (see following sections).

3.2.2 Spike rates of single units

Regressions were calculated among pre, stim and post condition of spike rate as function of cylinder size. A reaction in terms of spike rate of a unit was defined as increase or decrease of spike rate during stim or post condition. No unit with a significant effect of cylinder size on the Spike rate during pre condition was found in the regression analysis. Units which showed an increase in spike rate (Figs. 3.18, 3.19, 3.20 and 3.21), units which showed a decrease in spike rate (Fig. 3.22) and units which showed neither a significant increase nor a significant decrease (Fig. 3.23) with increasing cylinder size during stim condition were found. One unit which showed an increase in spike rate (Fig. 3.21) and units which showed a decrease in spike rate (Fig. 3.19 and 3.20) with increasing cylinder size during post condition were found. Figure 3.24 overview all processed units during pre, stim and post condition with plots of regression ordinate value as function of rate

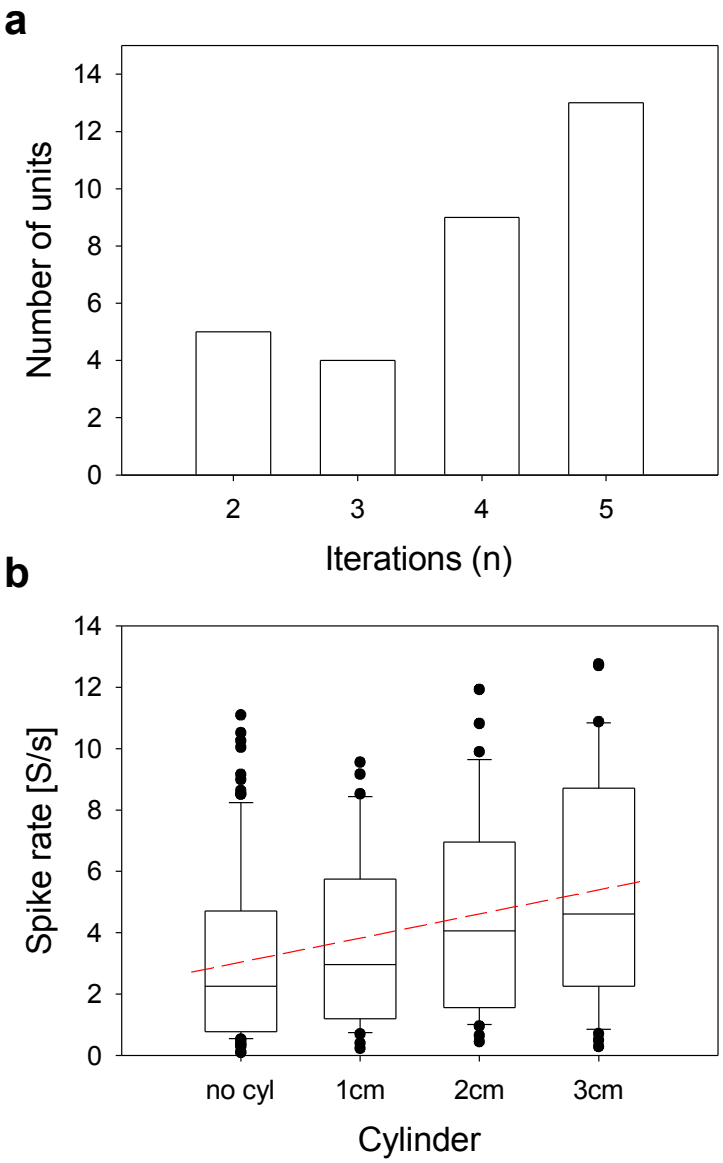

Figure 3.17: Number of experimental iterations (a) and spike rate of recorded units as function of cylinder size (b). Spike rate of recorded units increased with increasing cylinder diameter (stippled line, $m = 0.762$ [S/(s*cm)], $p < 0.001$), adj. $R^2 = 0.073$. Note that quartiles of spike rates lay between 0.787 [S/s] and 6.678 [S/s] which indicates a large variation of spike rates among recorded units.

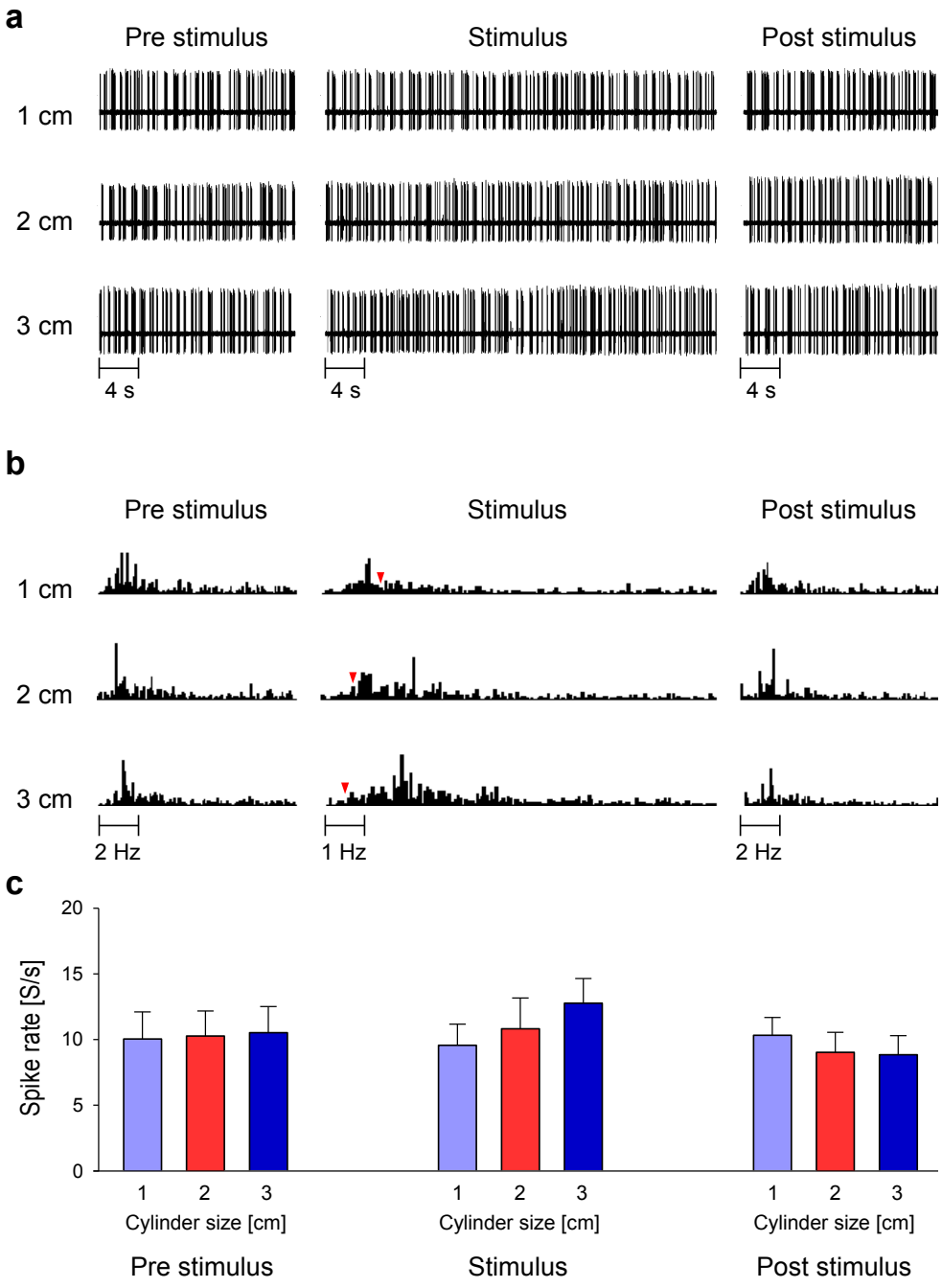

Figure 3.18: Spike pattern (a), FFT of spike pattern (b) and spike rate (c) of unit #3 as function of cylinder size and stimulus type. A single iteration of the experiment is shown in a and b. The peak frequency increased with increasing cylinder diameter (b). Note that peak frequency did not coincide with calculated vortex shedding frequency (red arrow heads). Spike rate of this unit increased with increasing cylinder size (c, $m = 1.600$, 95% C.I. $= [0.305; 2.895]$ [S/(s*cm)], $p = 0.019$). Error bars: s.d., $n = 5$.

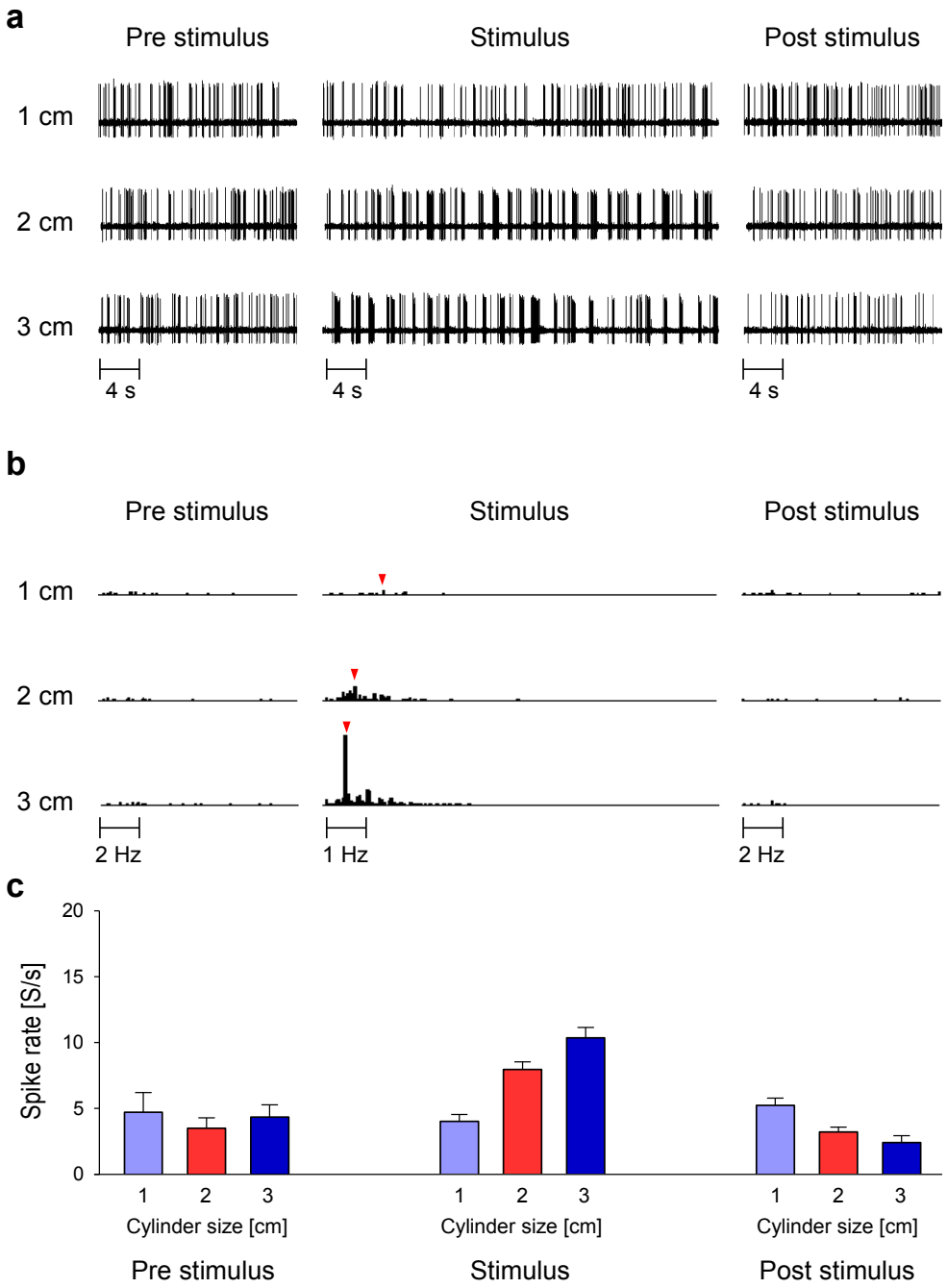

Figure 3.19: Spike pattern (a), FFT of spike pattern (b) and spike rate (c) of unit # 10 as function of cylinder size and stimulus type. A single iteration of the experiment is shown in a and b. Peak frequency decreased with increasing cylinder diameter (b). Note that peak frequency coincide with calculated vortex shedding frequency (red arrow heads). Spike rate of this unit increased with increasing cylinder size during stimulation (c, m = 3.167, 95% C.I. = [2.675; 3.660] [S/(s*cm)], $p < 0.001$). Additionally spike rate decreased with increasing cylinder diameter during post condition (c, m = -1.410, 95% C.I. = [-1.791; -1.029] [S/(s*cm)], $p < 0.001$). Error bars: s.d., n = 5.

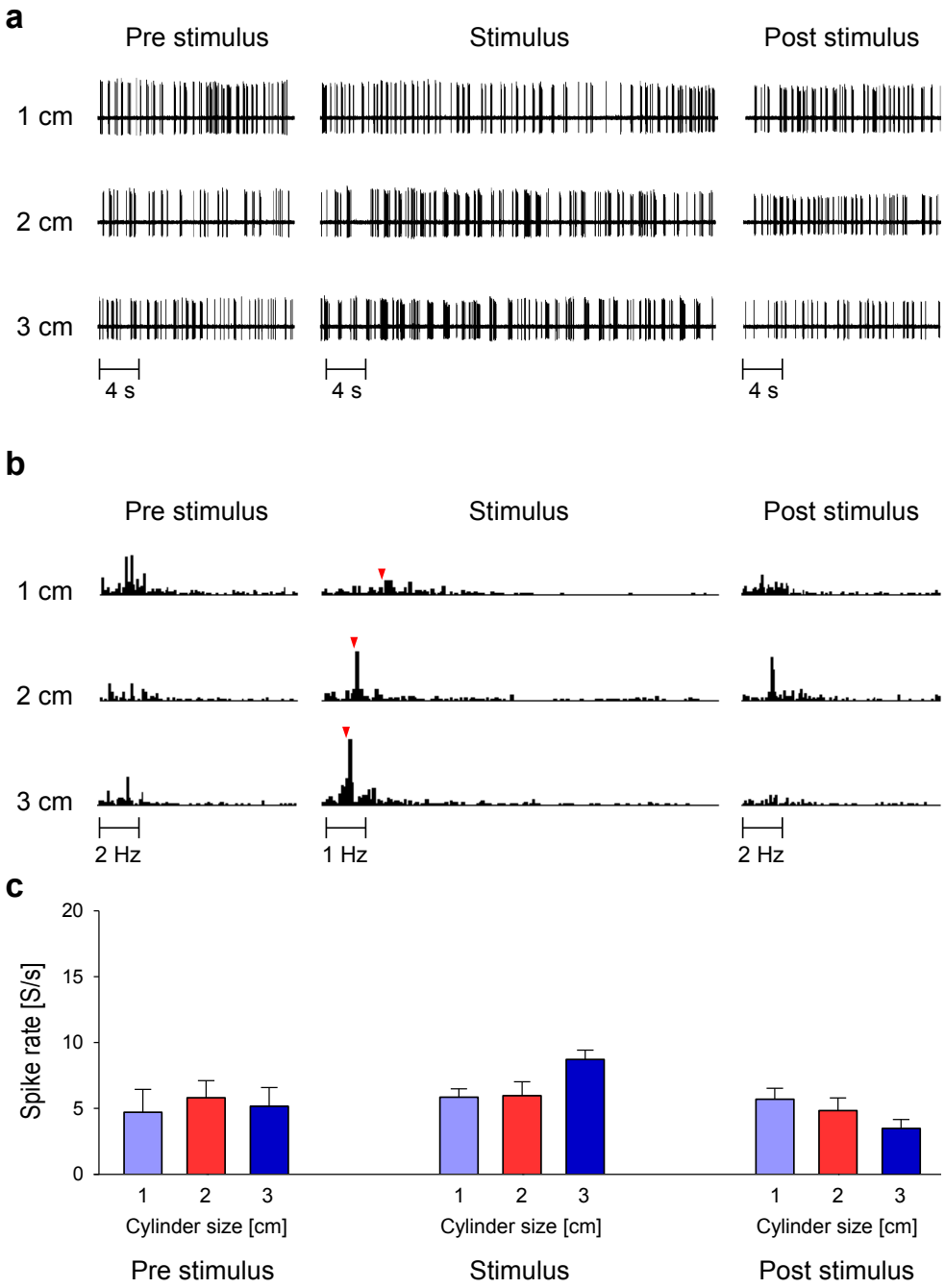

Figure 3.20: Spike pattern (a), FFT of spike pattern (b) and spike rate (c) of unit #15 as function of cylinder size and stimulus type. A single iteration of the experiment is shown in a and b. Peak frequency decreased with increasing cylinder diameter (b). Note that peak frequency coincide with calculated vortex shedding frequency (red arrow heads). Spike rate of this unit increased with increasing cylinder size during stimulation (c, m = 1.430, 95% C.I. = [0.726; 2,.134] [S/(s*cm)], p = 0.001). Additionally spike rate decreased with increasing cylinder diameter during post condition (c, m = -1.105, 95% C.I. = [-1.662; -0.548] [S/(s*cm)], p = 0.001). Error bars: s.d., n = 5.

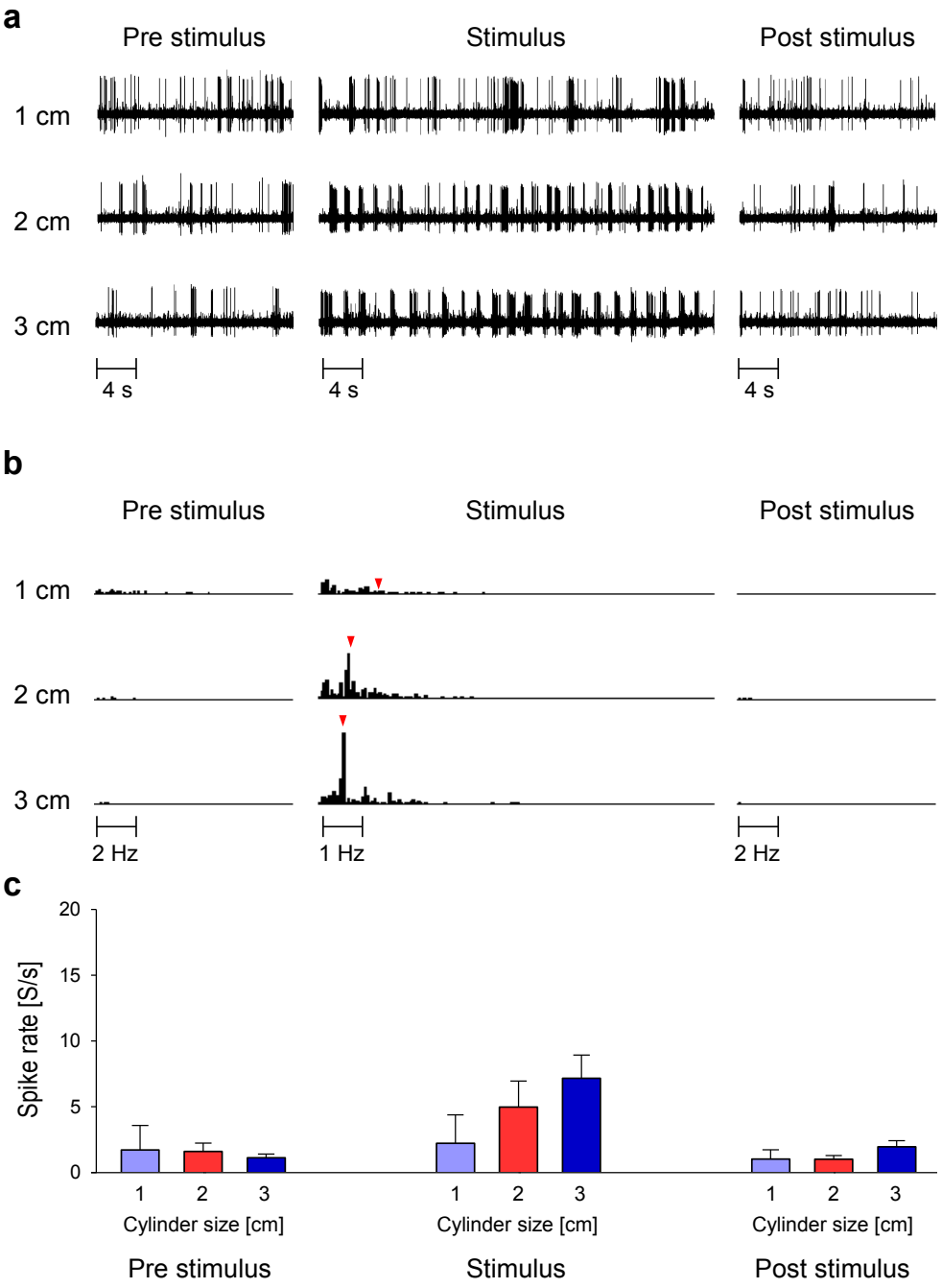

Figure 3.21: Spike pattern (a), FFT of spike pattern (b) and spike rate (c) of unit # 17 as function of cylinder size and stimulus type. A single iteration of the experiment is shown in a and b. Peak frequency decreased with increasing cylinder diameter (b). Note that peak frequency coincide with calculated vortex shedding frequency (red arrow heads). Spike rate of this unit increased with increasing cylinder size during stimulation (c, $m = 2.465$, 95% C.I. $= [1.165; 3.765]$ [S/(s*cm)], $p = 0.001$) and during post condition (c, $m = 0.470$, 95% C.I. $= [0.097; 0.843]$ [S/(s*cm)], $p = 0.017$). Error bars: s.d., $n = 5$.

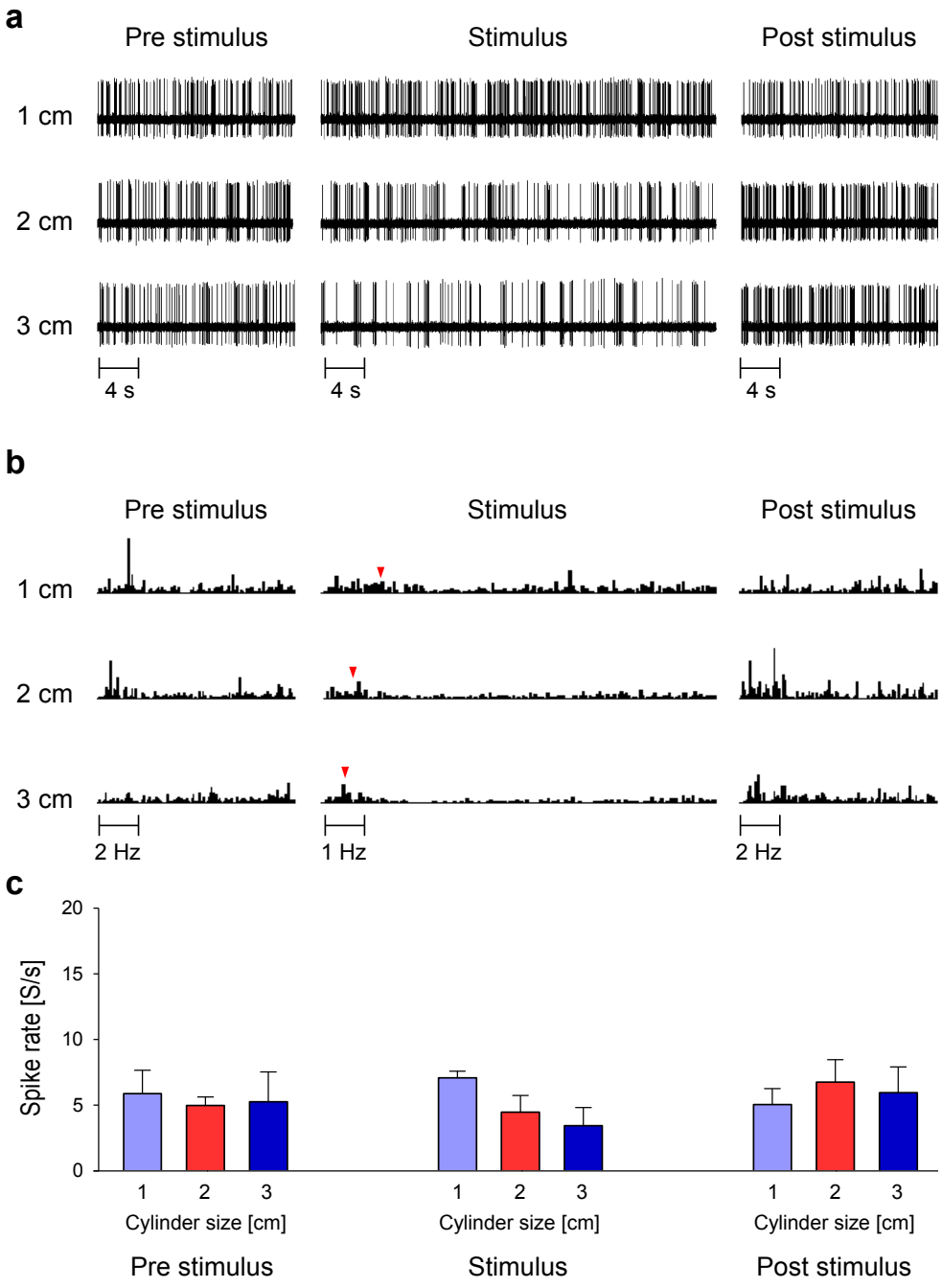

Figure 3.22: Spike pattern (a), FFT of spike pattern (b) and spike rate (c) of unit # 20 as function of cylinder size and stimulus type. A single iteration of the experiment is shown in a and b. Peak frequency decreased with increasing cylinder diameter (b). Note that peak frequency during stimulation with the 2 and 3 cm cylinder was similar to the calculated vortex shedding frequency (red arrow heads). Spike rate of this unit decreased with increasing cylinder size during stimulation (c, m = -1.823, 95% C.I. = [-2.604; -1.041] [S/(s*cm)], $p < 0.001$). Error bars: s.d., n = 5.

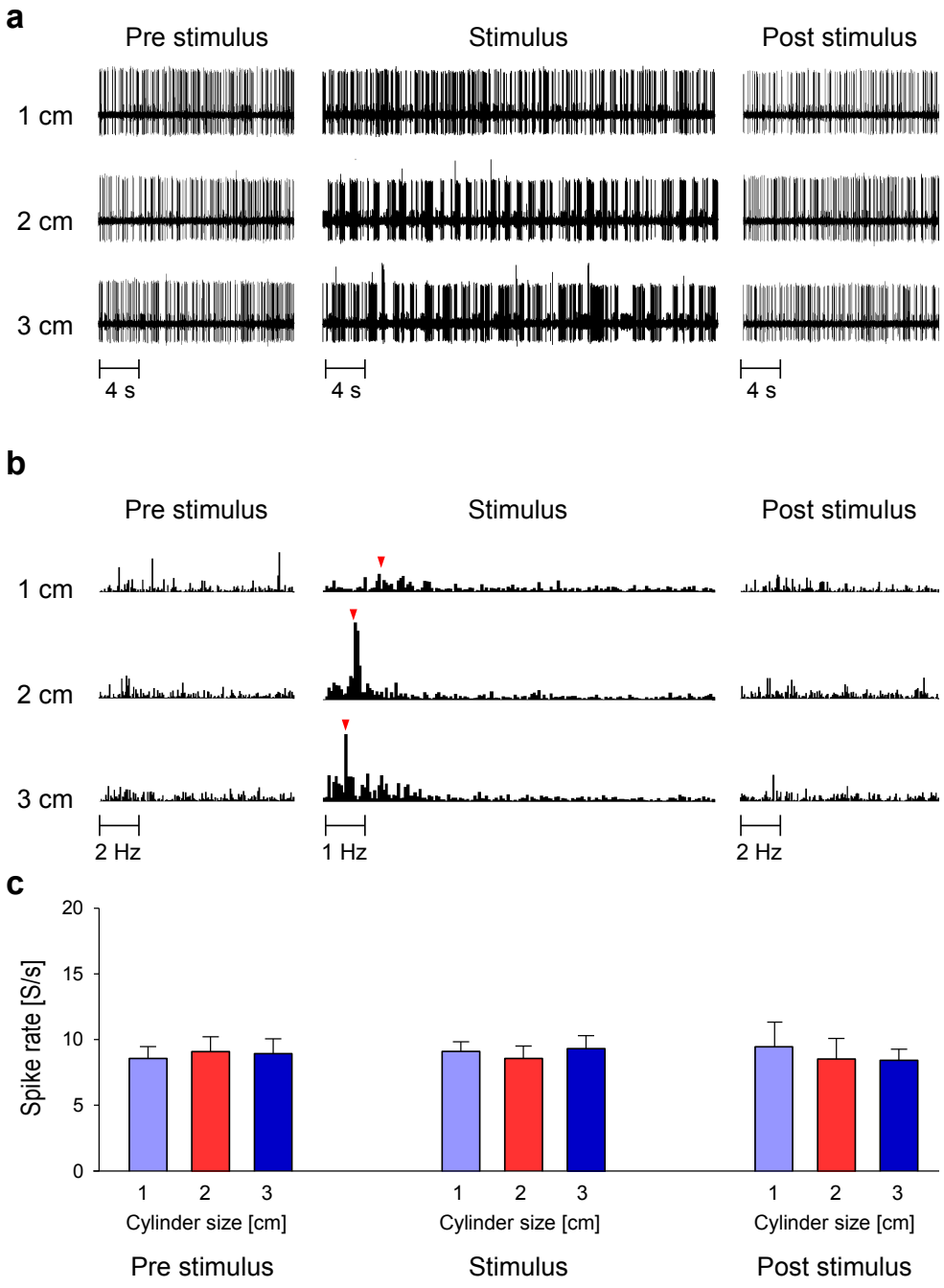

Figure 3.23: Spike pattern (a), FFT of spike pattern (b) and spike rate (c) of unit # 21 as function of cylinder size and stimulus type. A single iteration of the experiment is shown in a and b. Peak frequency decreased with increasing cylinder diameter (b). Note that peak frequency during stimulation with the 2 and 3 cm cylinder was similar to the calculated vortex shedding frequency (red arrow heads). No significant de- or increase of spike rate as function of cylinder size was found in the regression analysis. Error bars: s.d., n = 5.

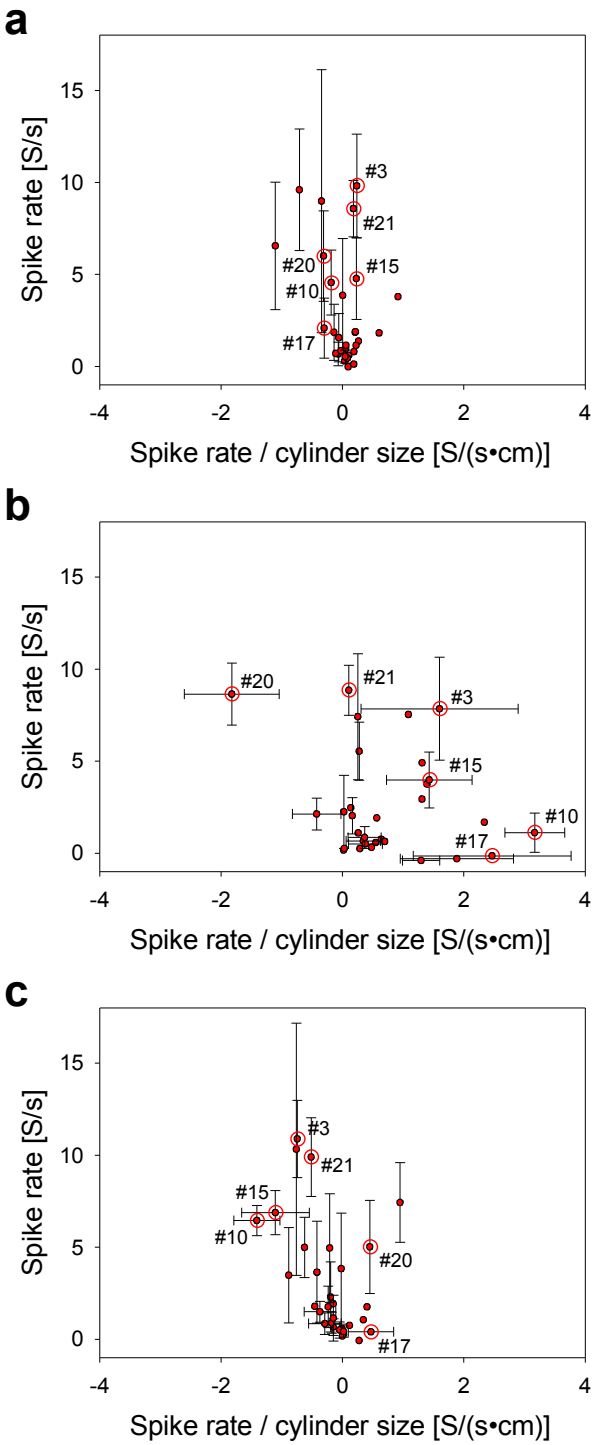

Figure 3.24: Ordinate value of regression as function of rate increase. During pre condition no significant rate increases were found (a). If cylinders were present (b, stim condition) and during post condition (c) some units showed a significant increase/decrease in spike rate if cylinder size was increased. Marked units were shown in figures 3.18 to 3.23. Error bars: 95% confidence intervals. Note that only confidence intervals of significant values were plotted.

	Pre	Stim	Post
1 cm vs. 2 cm	1	10	1
2 cm vs. 3 cm	0	19	3
1 cm vs. 3 cm	0	11	0

	1 cm	2 cm	3 cm
Pre vs. post	0	0	3
Pre vs. stim	5	15	16
Stim vs. post	7	20	17

Table 3.1: Number of significant differences which occurred among pairwise comparisons of spike rates during pre, stim and post condition (top table) and which occurred among pairwise comparisons of spike rates during 1 cm, 2 cm and 3 cm condition (bottom table). Most differences were found during stim condition (top table) and among comparisons between stim and pre/post condition (bottom table).

increase (slope of the regression). During pre condition only significant ordinate values occurred (Fig. 3.24 a, plotted 95% confidence intervals). During stim and post condition both, significant ordinate values as well as significant regression slopes, were found (Figs. 3.24 b and c, plotted 95% confidence intervals). During pre condition 0 of 31 units de- or increased significantly, during stim condition 11 of 31 units de- or increased significantly and during post condition 5 of 31 units de- or increased significantly with spike rate as function of cylinder size. Spike rate increase of stim case negatively correlated with spike rate increase of post case ($m = -0.291$ [post/stim], $p < 0.001$).

To analyse effects of factors cylinder size and experimental condition and if cylinder size as well as stimulus condition were distinguishable from each other in terms of spike rates a 2-way ANOVA was conducted. Significant differences were found among multiple comparisons. The total number of differences found in each pairwise comparison are indicated in table 3.1. Most differences were found during stim condition and among comparisons between stim and pre/post condition as expected. On the one hand this indicates that during stimulus condition cylinders had an effect on the spike rate and on the other hand this indicate that the presence of a cylinder was distinguishable from the case if no cylinder was present. Differences were also found during post condition (Table 3.1 top) which means that cylinder size during stim condition had an effect on the spike rate during post condition. Unexpected but only one significant difference between spike rates during pre condition caused by the 1 cm and 2 cm cylinder was found which indicates an influence of the cylinder size during stimulus presentation on the spike rate before the cylinder was presented (see section 4.2).

3.2.3 Spike pattern of single units

Most processed units showed bursts during stim condition (see a in Figs. 3.19, 3.20, 3.21 and 3.23). Units were found with a peak spiking frequency similar to calculated vortex shedding frequencies (v = 6 cm/s: 1.33, 0.75 and 0.57 Hz, see plot c in Figs. 3.19, 3.20, 3.21, 3.22 and 3.23). Additionally units were found with a significant rate increase which did not showed a peak frequency similar to the vortex shedding frequency (Fig. 3.18). Bursting and vortex street oscillation in spiking activity is also visible in spike interval images (Figs. 3.25 and 3.26). Note that two different frequency components were visible due to at least two peaks. One component (Figs. 3.25 and 3.26, blue arrows) in the range of 100 ms which coincide with time separation between adjacent spikes in bursts and one component (Figs. 3.25 and 3.26, red arrows) in the time range of vortex street delays, which increased with increasing cylinder size as expected. The effect of increasing and decreasing spike rate with increasing cylinder size is also visible in spike interval plots in terms of increasing or decreasing number of spike intervals with a certain delay range.

3.2.4 PIV and neuronal response of single units

Two units were found which showed a correlation peak close to the surface of rudd (Figs. 3.27 and 3.28). Mean flow velocity decreased with decreasing distance to the rudd as expected (Figs. 3.27 and 3.28 a). In the presence of a 3 cm cylinder flow velocity downstream of the cylinder was decreased (2 cm/s) compared to the bulk flow velocity (PIV: 6 cm/s). In both cases a positive cross correlation peak between unit activity and vertical flow velocity (u) was found (Figs. 3.27 and 3.28 b). Neuronal activity at the peak correlation side was synchronously active with positive flow velocity (Figs. 3.27 and 3.28 e). A negative peak was found in the correlation map between vertical flow component (v) and neuronal activity (Figs. 3.27 and 3.28 c). Neuronal activity at the peak correlation side was synchronously active with negative flow velocity (Figs. 3.27 and 3.28 f). No peak with similar magnitude than in maps of vertical and horizontal flow component was found between unit activity and flow magnitude (Figs. 3.27 and 3.28 d).

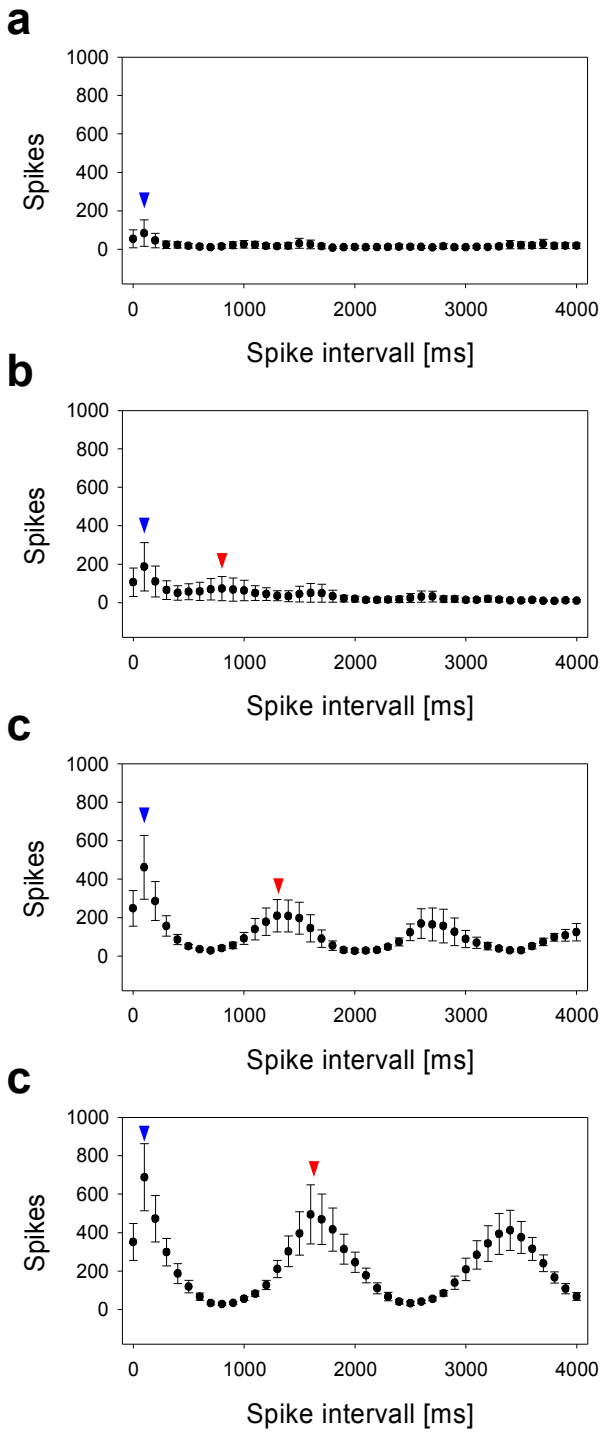

Figure 3.25: Spike interval plot of unit # 17 as function of cylinder size (a: no cylinder, b: 1 cm, c: 2 cm and d: 3 cm). A peak is visible in each plot at 100 ms delay (blue arrows). A second peak occurred in the presence of a cylinder and coincide with vortex shedding delay (red arrows). Additionally the amount of spikes and therefore the number of overall spike intervals increased (compare also with Fig. 3.21). Error bars: ± s.e.

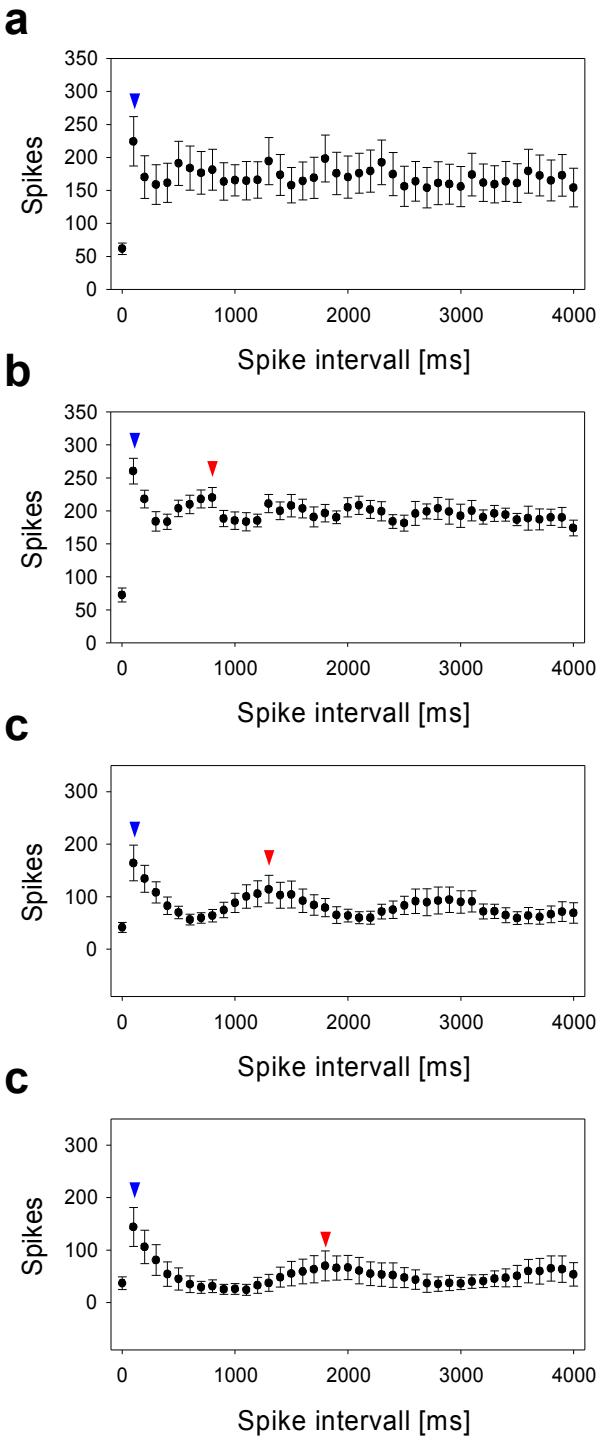

Figure 3.26: Spike interval plot of unit # 20 as function of cylinder size (a: no cylinder, b: 1 cm, c: 2 cm and d: 3 cm). A peak is visible in each plot at 100 ms delay (blue arrows). A second peak occurred in the presence of a cylinder and coincide with vortex shedding delay (red arrow). Additionally the amount of spikes and therefore the number of overall spike intervals decreased (compare also with Fig. 3.22). Error bars: ± s.e.

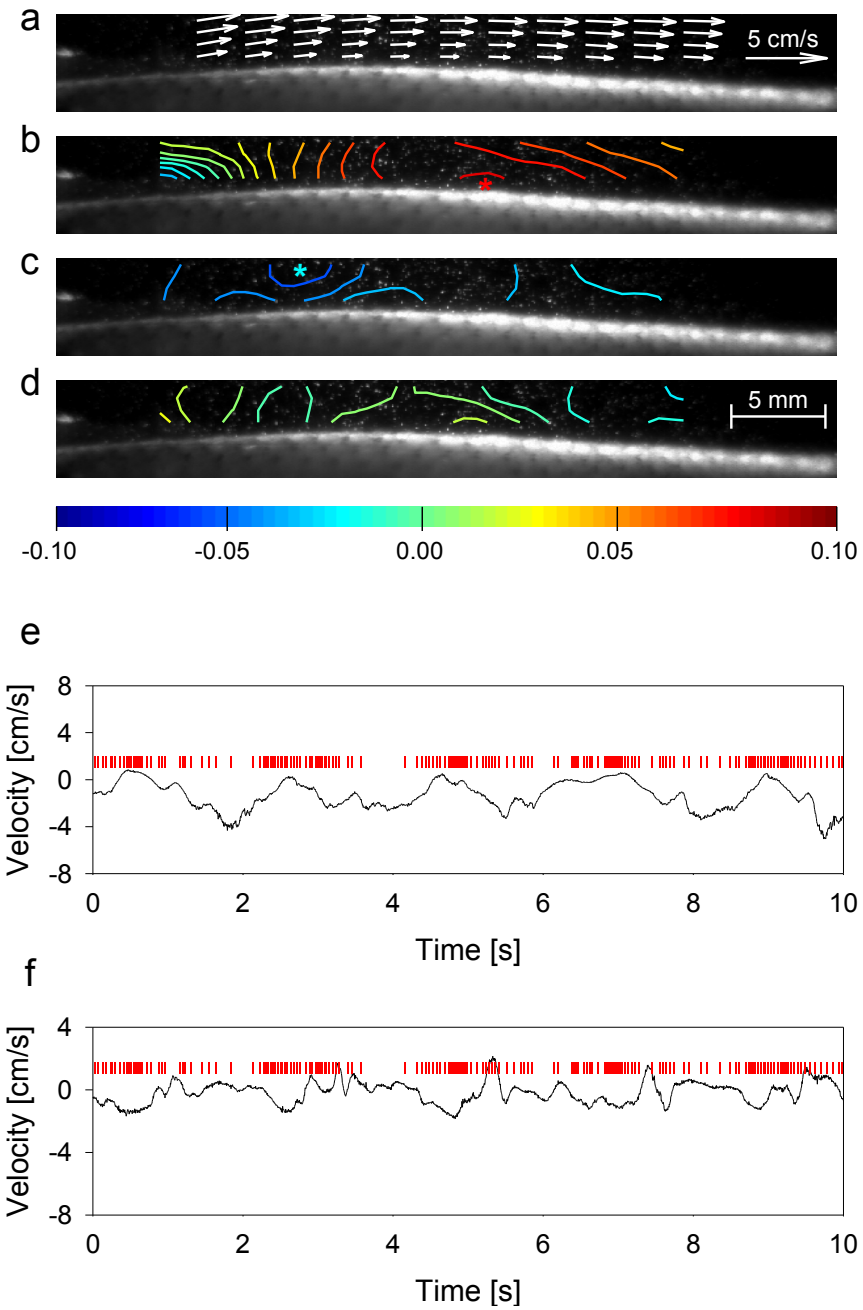

Figure 3.27: Mean flow (a) and correlation between flow and spiking activity (b, c and d) of unit #32 as function of place caused by a 3 cm cylinder. Flow was almost parallel to the fish (a) and decreased with decreasing distance to the fish. Cross correlation values at 0 ms time shift between spiking activity and horizontal flow component (b) showed a positive peak close to the fish (red star in b). Cross correlation values at 0 ms time shift between spiking activity and vertical flow component (c) showed a negative peak in 2 mm distance to the fish (blue star in c). Cross correlation values at 0 ms time shift between spiking activity and flow magnitude (d) showed correlation values close to 0.0 (green). Note that area of interest was located between pectoral (left) sand anal fin (right).

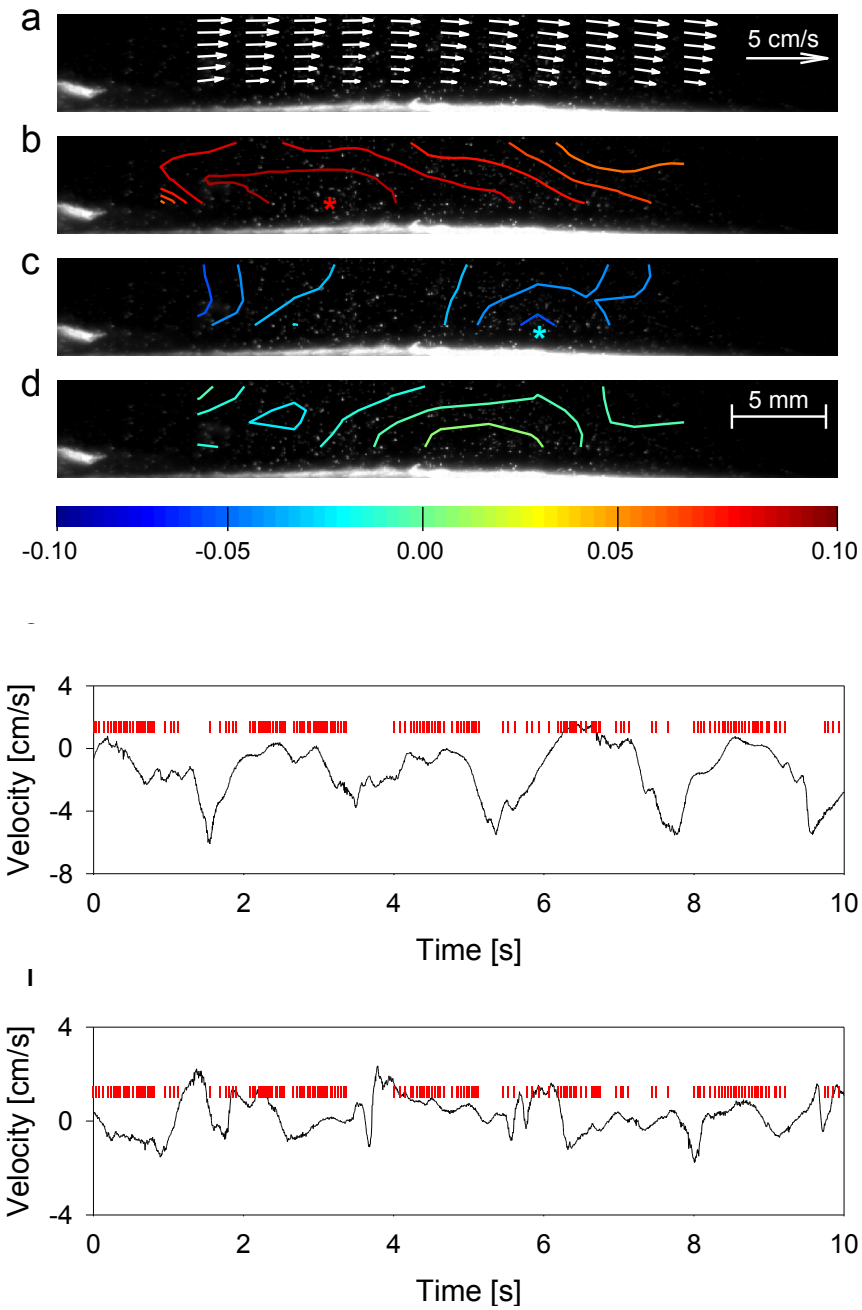

Figure 3.28: Mean flow (a) and correlation between flow and spiking activity (b, c and d) of unit # 25 as function of place caused by a 3 cm cylinder. Flow was almost parallel to the fish (a). Note that vectors inside the boundary have not been computed. Cross correlation values at 0 ms time shift between spiking activity and horizontal flow component (b) showed almost positive values (red). Cross correlation values at 0 ms time shift between spiking activity and vertical flow component (c) showed almost negative values (blue). Cross correlation values at 0 ms time shift between spiking activity and flow magnitude (d) showed correlation values close to 0.0 (green). Note that area of interest was located between pectoral (left) sand anal fin (right).

3.3 Lateral line canal morphology and signal to noise ratio

3.3.1 Control experiments and frequency response of the sensor

The ALLC with no pores neither responded to bulk water flow (9 cm/s), a vibrating sphere stimulus (frequency, amplitude 45 cm/s), to a Kármán vortex street (vortex shedding frequency 0.93 Hz) or to the hydrodynamic noise caused by air bubbles (noise level 2). In the frequency range 10 - 80 Hz (peak velocity always 45 cm/s), the sensor produced a sinusoidal output signal whose amplitude decreased with increasing sphere vibration frequency. Peak values of the Fourier transformed sensor output signal diminished exponentially with stimulus frequency (1P ALLC). A vibrating cylinder (diameter 1 cm) placed vertically close to the ALLC also caused sinusoidal output signals (Fig. 3.29). In this case the mean rectified amplitude obtained with the ALLC 1P was significantly smaller compared to the mean rectified amplitudes obtained with ALLCs P5n, P5w, P9, P13 and P33 (ANOVA on ranks, $p < 0.05$, Fig. 3.30). Consequently absolute sensor output values obtained with ALLC P1 are not comparable with absolute sensor output values obtained with ALLCs P5n, P5w, P9, P13 and P33.

3.3.2 Air bubble noise

To investigate how the responses of the ALLCs are contaminated by hydrodynamic noise two noise levels were applied: Noise level 1 (low air bubble density): Horizontal air bubble size 3.10 ± 1.48 mm, vertical air bubble size 2.92 ± 1.53 mm and inter air bubble time interval 19.20 ± 9.31 s. Noise level 2 (high air bubble density): Horizontal air bubble size 4.20 ± 0.62 mm, vertical air bubble size 3.60 ± 0.44 mm and inter air bubble time interval 19.90 ± 7.40 s.

3.3.3 Vortex street signal as function of cylinder distance

In this experiment the ALLCs were exposed to running water and to the vortices shed by a cylinder. The upstream position of the cylinder varied between 1.5 and 9 cm. Sensor output signals showed periodic peaks at the vortex shedding frequency (Fig. 3.31 a). Autocorrelation peak amplitudes (Fig. 3.31 b) of the ALLCs 1P and 13P decreased after a cylinder distance of 3 cm. This decrease was more pronounced in the ALLC 1P than in the ALLC 13P (3.0 cm $p < 0.05$ t-test, 6.0 cm $p < 0.01$ t-test, 9.0 cm $p < 0.01$ rank sum test).

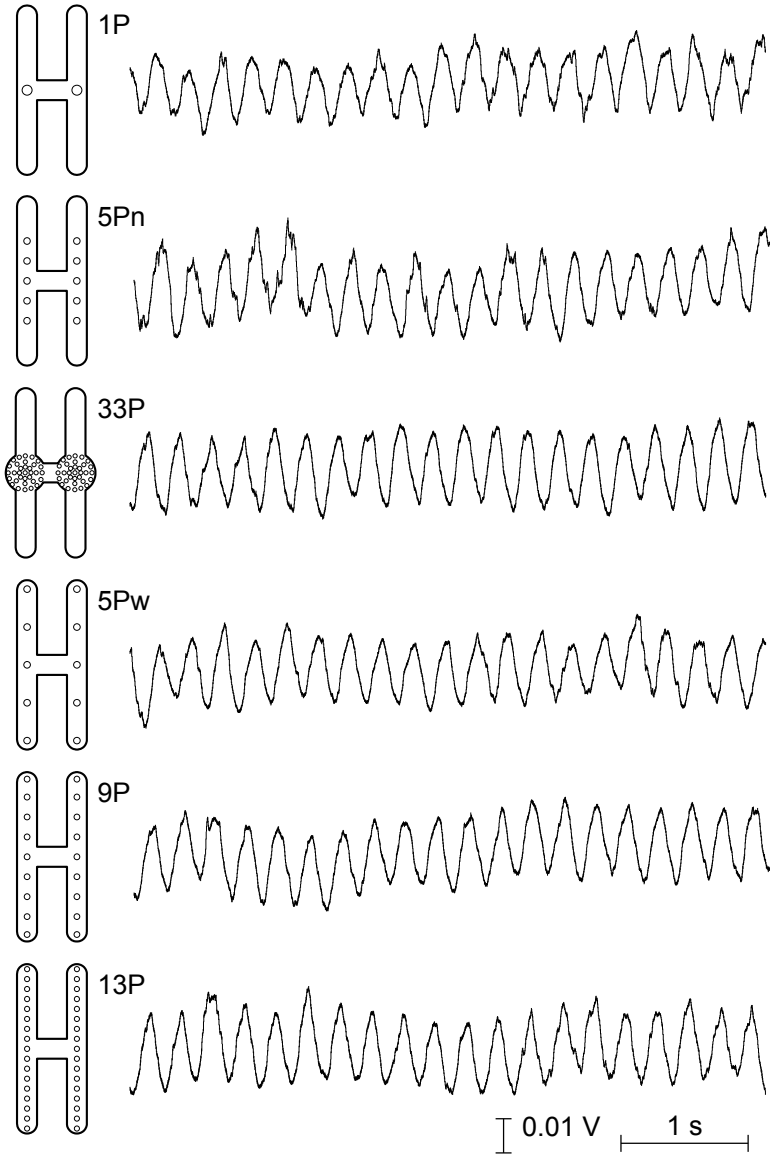

Figure 3.29: Signal as function of ALLC type in the presence of a vibrating cylinder. A vibrating cylinder caused sinusoidal output signals of the AN of all ALLCs. Vibrating frequency: 4 Hz.

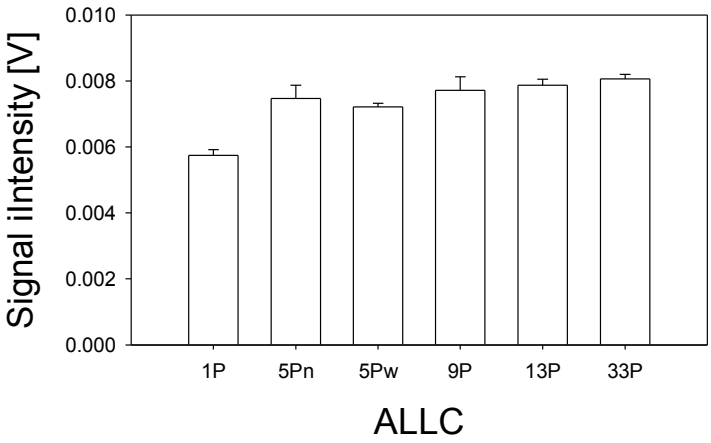

Figure 3.30: Signal amplitudes as function of ALLC type in the presence of a vibrating cylinder. Significant differences were found between ALLC 1P and other ALLCs. This means that in some cases comparison of ALLCs in terms of signal amplitude was not possible. Error bars ± s.e.

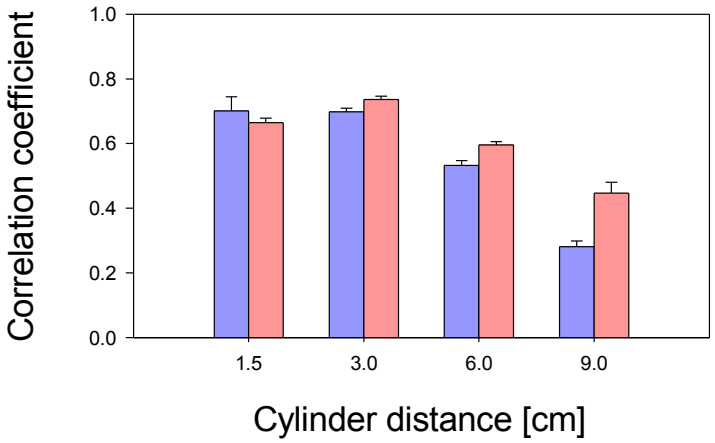

Figure 3.31: Sensor signal caused by a Kármán vortex street. A cylinder was placed 1.5, 3.0, 6.0 and 9.0 cm upstream of the sensor device. ALLCs 1P (blue) and 13P (red) were used during measurements. Correlation coefficients decreased with increasing cylinder distance indicating that the self similarity of vortex streets decreased with vortex street age. Signals measured with ALLC 13P showed higher correlation values than ALLC 1P at larger distances. Error bars ± s.e.

3.3.4 Responses to the vibrating sphere under noise conditions

In this experimental series the ALLCs (1P and 13P) were stimulated in still water with a sphere vibrating with 10 Hz (sphere displacement amplitude <1 mm). The frequency of the sensor signal equaled the vibration frequency of the sphere, i.e. autocorrelation of the data (Fig. 3.32 a, b) yielded a maximum at a delay time of 0.1 s (10 Hz). If hydrodynamic noise was added (noise level 2) the sinusoidal sensor signals were superimposed by large peaks (Fig. 3.32 c, d). Output signals of ALLC 1P contained larger peaks than the output signals of ALLC 13P. There was no local autocorrelation maximum at 0.1 s when the ALLC 1P was exposed to the vibrating sphere and noise. In contrast, when ALLC 13P was exposed to the vibrating sphere and noise an autocorrelation maximum at 0.1 s was still visible but smaller compared to the no noise condition (Fig. 3.32 d). The difference between the autocorrelation amplitudes (0.1 s delay) of ALLCs 1P and 13P was significant (Fig. 3.32 c, d; univariate linear model [t-test], SPSS, p = 0.003, 95%-C.I. = [0.063; 0.221],) if noise was present.

3.3.5 Vortex street and noise

For these experiments ALLCs 1P, 5Pn and 33P (group 1, low spatial distribution of pores) and ALLCs 5Pw, 9P and 13P (group 2, large spatial distribution of pores) were used (c.f. Fig 2.6). All these canals had one artificial neuromast (sensor). As in the previous experiment the ALLCs were exposed to running water and to the vortices shed by a cylinder. In addition hydrodynamic noise was added in some of the experiments. In the noise free case, the signal output of all ALLCs showed periodic peaks that represented the vortex shedding frequency (Fig. 3.33, no noise). If noise was added, the periodic peaks were smaller and superimposed by less predictable peaks (Fig. 3.33, noise level 1). Compared to no noise conditions peak autocorrelation values significantly (2 way ANOVA, $p < 0.001$) decreased if noise (noise level 1) was present. At noise level 2 this decrease was even more pronounced (compare Fig. 3.34 a and b). For statistical analysis a two way Anova with the two factors ALLC type and noise (no noise and noise) was used. Noise level 1 (Fig. 3.34 a): There was a significant interaction between the type of ALLC and the noise condition ($p = 0.017$). This indicates that the canal type influences how noise alters the autocorrelation and thus the output signal of the respective ALLC. There were no significant differences if no noise was present. Significant differences in multiple comparisons (Bonferroni t-test, $\alpha = 0.05$) were found between all ALLCs of group 1 and group 2 if noise was

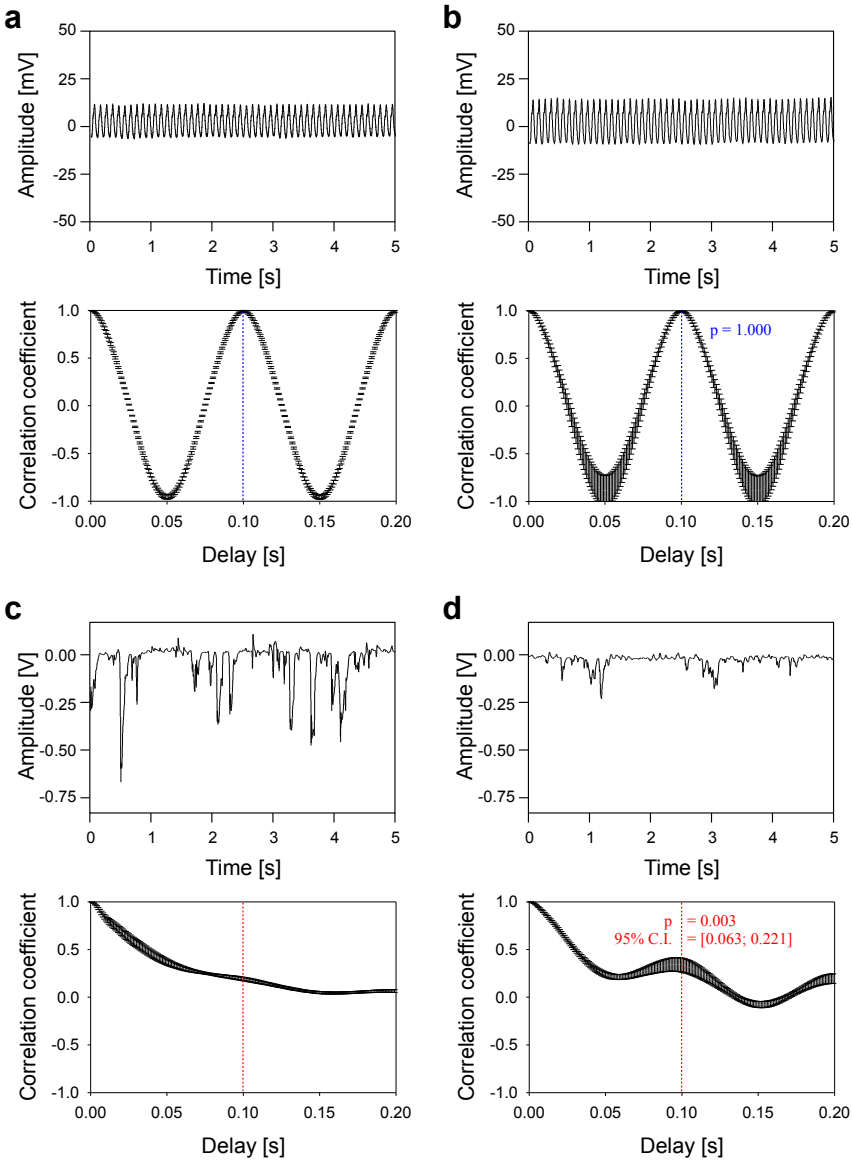

Figure 3.32: Influence of ALLC type on auto correlations (bottom graphs) of sensor signals (top graphs) in the presence of a vibrating sphere and air bubble noise (c, d). In the case of no air bubble noise sinusoidal oscillations in the sensor output measured with ALLCs 1P (a, top graph) and 13P (b, top graph) were visible. The auto correlation of both signals (a and b, bottom graphs) showed a peak at 0.1 s (10 Hz). No significant difference of peak auto correlation coefficients (stippled blue lines, $p = 1.000$, t-test) was found. In the presence of noise (c, d) sensor signals measured with ALLCs 1P (c) and 13P (d) showed disturbances (top graphs, sharp peaks). Disturbances measured with ALLC 13P had lower amplitudes than disturbances measured with ALLC 1P. Peak auto correlation coefficients of both signals (c and d, bottom graphs) significantly differed at 0.1 s ($p = 0.003$, t-test). Note that scaling in a and b is different to c and d (top graphs) and that in the presence of noise only a peak at 0.1 s was visible in the auto correlation of signals recorded with ALLCk 13P. Error bars ± s.e.

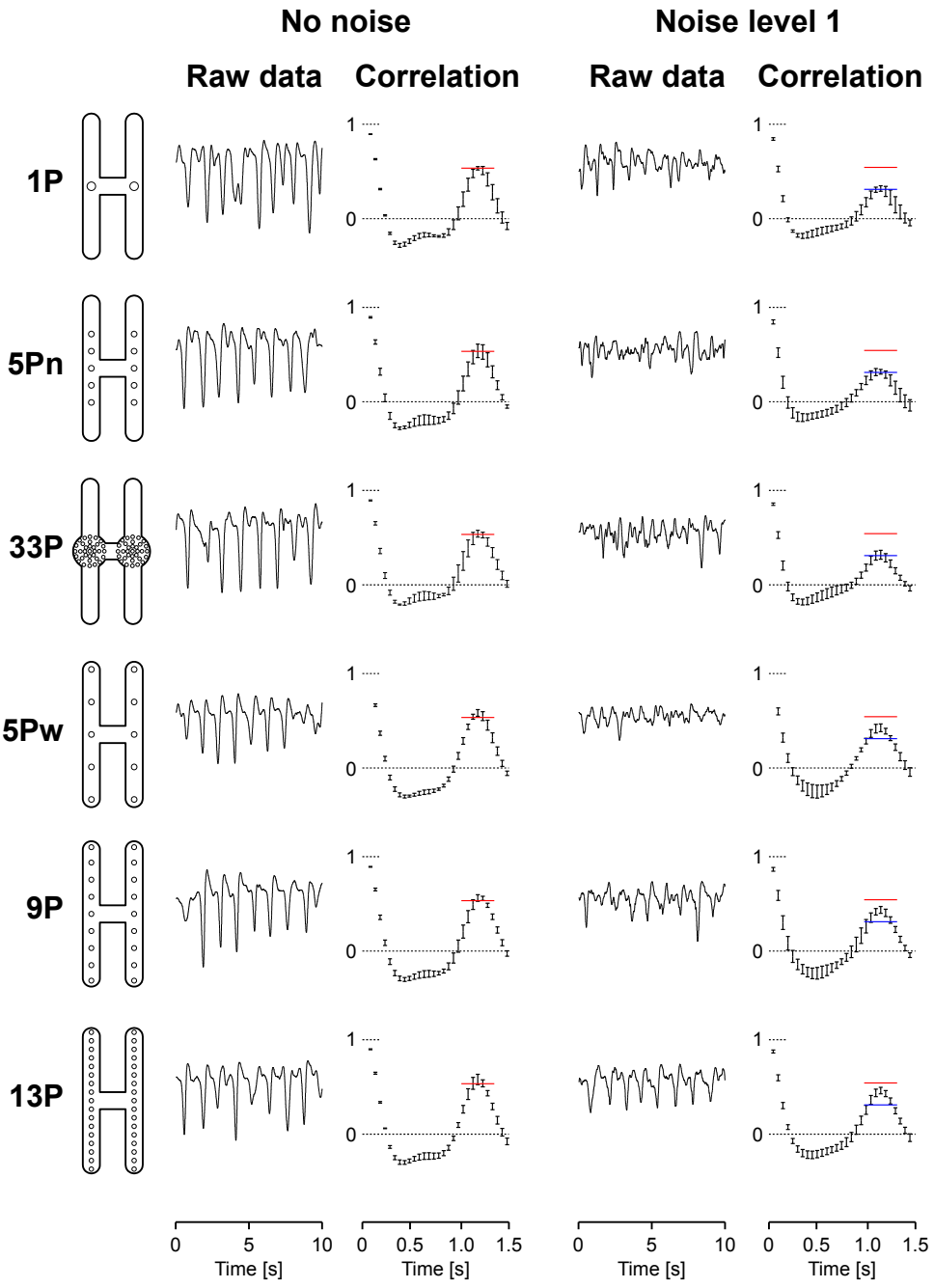

Figure 3.33: Raw data of ALLCs which were stimulated with a vortex street under noise less and noise level 1 case. Autocorrelation of all experimental cases showed a local peak at vortex shedding delay. Error bars ± s.d. Red lines indicate mean correlation peak of ALLC 1P of the noise less case. Blue lines indicate mean correlation peak of ALLC 1P of the noise level 1 case. Note that noise influences peak correlation magnitude. ALLCs 5Pw, 9P and 13P showed higher peak correlation values than ALLCs 1P, 5Pn and 33P if noise level 1 was present.

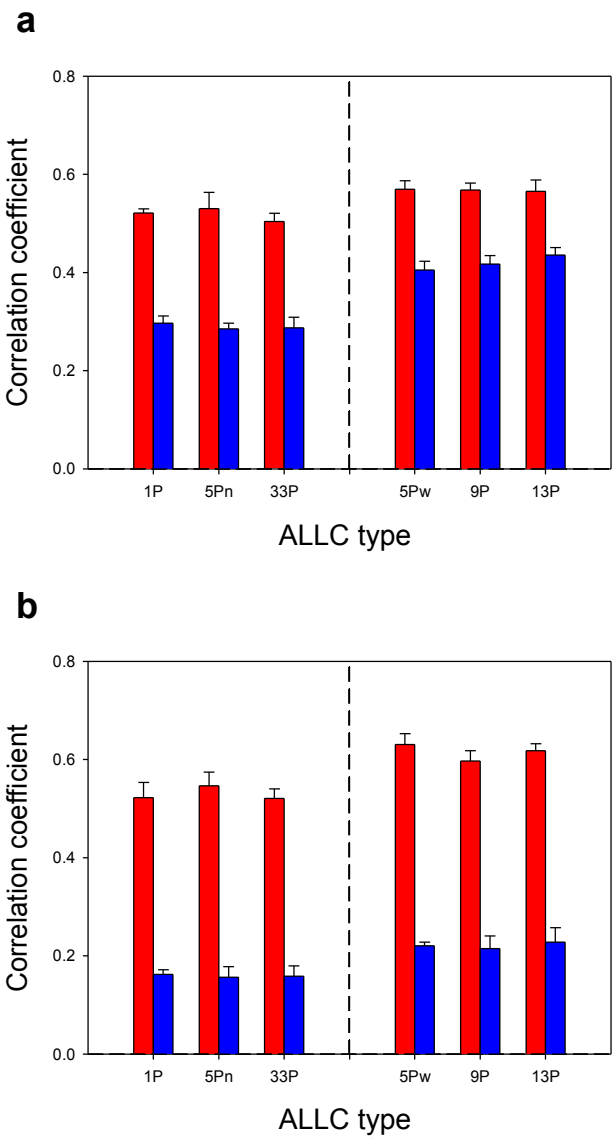

Figure 3.34: Peak autocorrelation coefficients of sensor output caused by a vortex street as function of ALLC type during no noise and noise condition. A D-cylinder was placed 6 cm upstream of the center of ALLCs (1P, 5Pn, 33P, 5Pw, 9P and 13P) and exposed to flow with (blue) and without (red) air bubbles. Noise significantly (2 way ANOVA $p < 0.001$) decreased autocorrelation coefficients. Noise level 1 (a, less air bubbles): during noise ALLCs 5Pw, 9P and 13P had significantly higher autocorrelation coefficients in multiple comparisons than ALLCs 1P, 5Pn and 33P. Noise level 2 (b, more air bubbles): ALLCs 5Pw, 9P and 13P had significantly higher autocorrelation coefficients in multiple comparisons than ALLCs 1P, 5Pn and 33P if no noise was present (excluding pairs 9P and 1P, 5Pn and 33P). Note that autocorrelation coefficients were more influenced if noise level was increased and that if differences between different ALLCs were found ALLCs with high spatial extension of pores (5Pw, 9P and 13P) had higher autocorrelation coefficients than ALLCs with less spatial extension of pores (1P, 5Pn and 33P). Error bars + s.e.

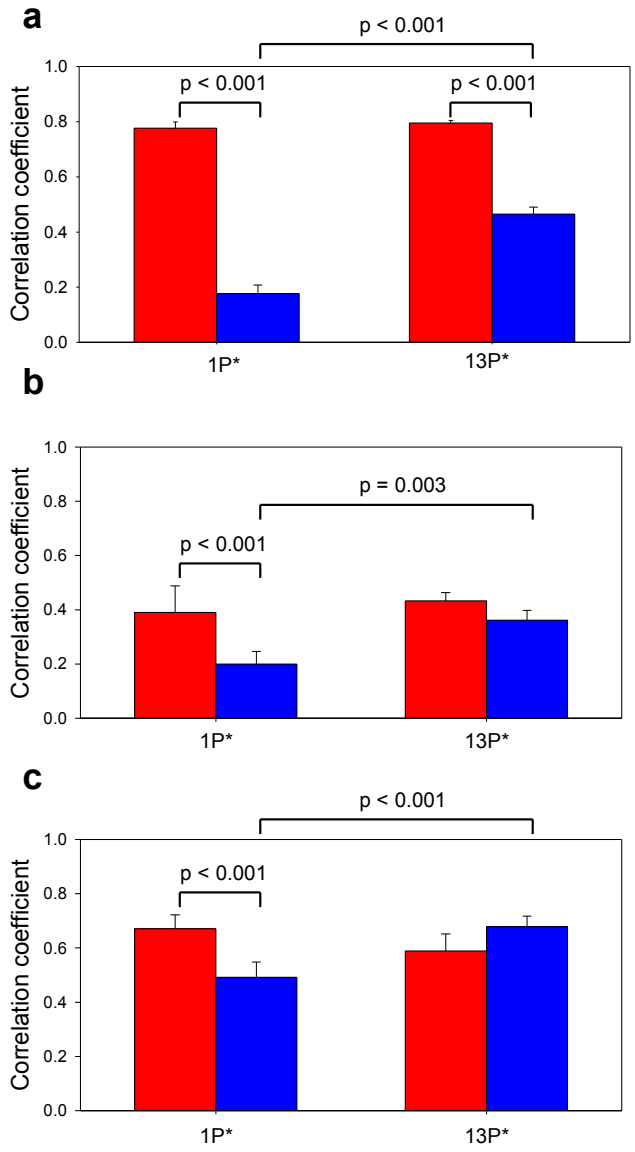

Figure 3.35: Peak autocorrelation coefficients of two sensor outputs caused by a vortex street as function of ALLCs 1P* and 13P*. A D-cylinder was placed 6 cm upstream of the center of an ALLC (1P* and 13P*) and exposed to flow with (blue) and without (red) air bubbles. Second peak autocorrelation values of the up- (a) and downstream (b) sensor substantially decreased in most cases if noise was present. Peak cross-correlation value (c) decreased if ALLC 1P* was used. In all noise cases (blue bars in a, b and c) correlation values obtained with ALLC 1P* were below correlation values obtained with ALLC 13P*. Error bars + s.d.

present (pmax = 0.01). Noise level 2 (Fig. 3.34 16 b): No significant interaction between both factors (ALLC type and noise/no noise) was found (p = 0.867). Significant differences in multiple comparisons (Bonferroni t-test, $\alpha = 0.05$) were found between ALLCs of group 1 and group 2 (excluding combinations ALLC 9P and group 1) under both experimental conditions (no noise and noise level 2, pmax = 0.032). In the previous experiments the signals of only 1 artificial neuromast was available and therefore only the autocorrelation as a measure of self similarity. To examine how the type of ALLC influences the similarity between the output signals of adjacent neuromasts (cross correlation) further experiments with ALLCs (ALLC 1p* and 13p*) that contained 2 ANs were conducted.

ALLCs again were exposed to a vortex street or to both, a vortex street and air bubble noise. If air bubble noise was present autocorrelation also decreased ompared to the noiseless case (2 way ANOVA, factors presence of noise and ALLC type, Fig. 3.35 a and b). Similar to the previous section this decrease was more pronounced in ALLC 1P* than in ALLP 13P*. Under noise conditions correlation values obtained with ALLC 1P* differed from those obtained with ALLC 13P*. An interaction between the factors ALLC type and noise (noise, no noise) was not only found in the autocorrelation (Fig. 3.35 a, b) but also in the cross correlation (Fig. 3.35 c). On the one hand differences were found in the peak cross correlation value obtained with ALLC 1P* between the noise and noiseless case. On the other hand a difference was found in multiple comparisons in the noise case between cross correlation values of ALLC 1P* and 13P*.

3.4 Optimization of an optical artificial neuromast for fabrication with MEMS

3.4.1 Flow velocity as function of diminution width

The geometry was successfully meshed (Fig. 3.36 a, b) and a pressure gradient was present between both pores inside the simulated lateral line canal as expected (Fig. 3.36 c). According to the pressure gradient a flow profile developed inside the canal (Fig. 3.36 d). Flow inside the diminution was higher than flow inside the straight part of the canal. In contrast to canals with diminution (Fig. 3.37 a, 100 to 500 μm) a canal without diminution shows uniform flow along the length axis (Fig. 3.37 a, 1000 μm). Flow always was higher inside diminution than in non-tapered regions of each canal but flow velocity among different canals with different diminutions differed (Fig. 3.37 b). Simulated peak velocity of 97 μm/s occurred at a diminution size of 300 μm (Fig. 3.37 a, 300 μm). Peak velocity (300 μm diminution) was 64% higher than peak velocity of a canal without diminution (Figs. 3.37 a and b). Peak velocities of calculations with coarse and fine mesh differed less than 1.2% (coarse mesh: 96.63 μm/s, fine mesh: 97.74 μm/s, 300 μm diminution).

3.4.2 Bar deflection in the diminution as function of bar width and flow velocity

The simulated silicon bar bended in the presence of flow. Maximum simulated bar deflection of 6.4 μm occurred at the minimum simulated bar width of 50 μm. Maximum bar bending was 48% higher than minimum simulated bar deflection (4.3 μm) of a 250 μm width bar. Note that bar deflection rapidly decreased to a plateau with increasing bar width (for instance: 100 μm bar width, 4.7 μm bar deflection).

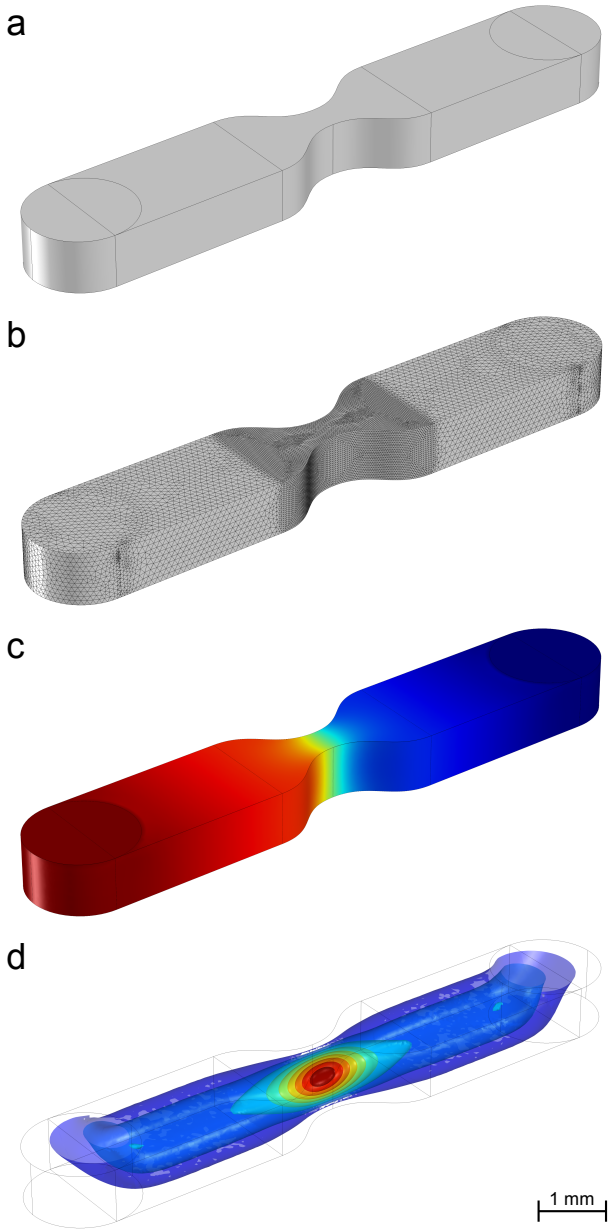

Figure 3.36: Geometry (a), mesh (b), pressure (c) and absolute flow velocity (d) of a simulated artificial lateral line canal. The simulated canal had a diminution of 300 μm. The resolution of the tetrahedral mesh was finest at the diminution to higher the precision of the simulation. In contrast to a straight canal – were pressure linearly drops between pores – the diminution leaded to a rapid pressure drop separating two chambers (c, red and blue regions). Isolines of flow magnitudes (d) show that flow was almost constant inside the straight parts of the canal and accelerated inside the diminution. Peak velocity occurred at the center of the diminution.

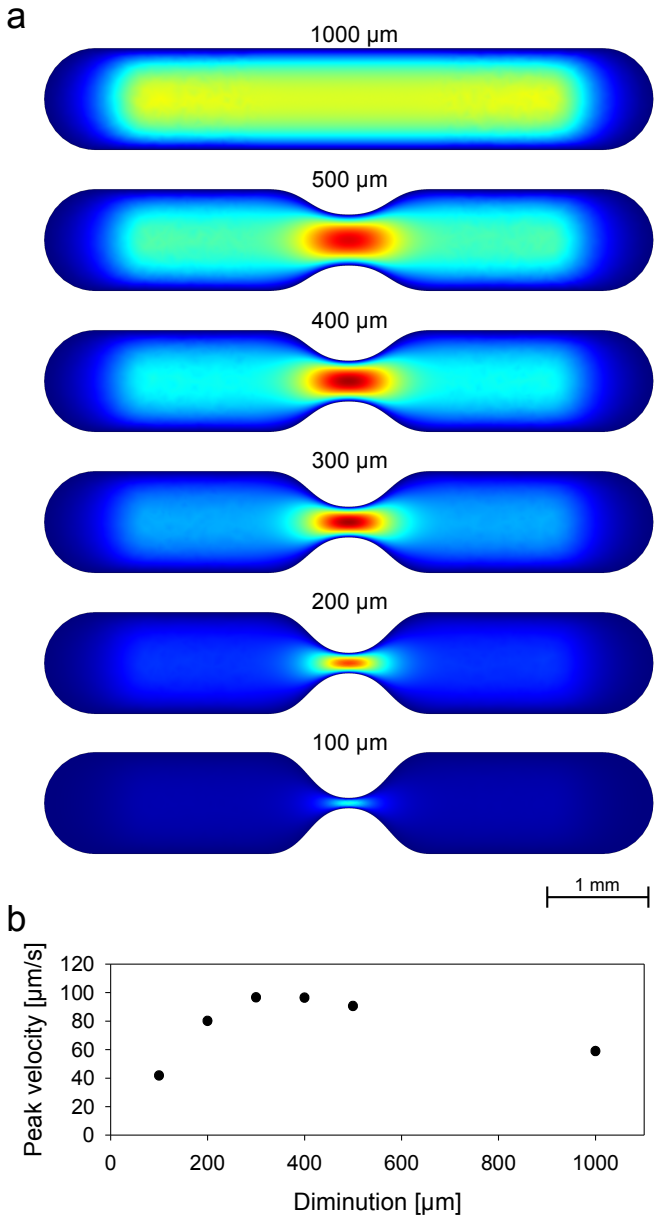

Figure 3.37: Velocity profiles (a) and peak velocity (b) as function of diminution size. In the case of no diminution (a, 1000 μm) flow was unhindered and equally distributed along the canal. Flow was always highest inside the diminution (a, 100, 200, 300, 400 and 500 μm). Maximum simulated peak velocity occurred in case of a diminution size of 300 μm (a and b). Peak velocity in the 300 μm case was more than 1.6 fold higher than peak velocity in the case of no diminution.

3.5 Improvement of production steps of optical artificial neuromasts

3.5.1 Sensor design

A two layer design was found which showed functional circuits (Fig. 3.38). Conductive paths connected electronic elements which were located on two sides. Circuit paths were guided through the circuit board with vias (Fig. 3.38 a). PSDs were positioned on the opposite of operational amplifiers to reduce space and simplify conductive shielding from water (Fig. 3.38 a and b). The light amplification circuit consisted of 64 electronic elements in the 8 channel design. Due to the SMD design the inter bar distance compared to the hand manufactured sensor device (Part 2.3) (Klein and Bleckmann, 2011; Klein et al., 2011; Klein and Bleckmann, 2012) was halved. The circuit board was sized $48 \times 28\,\mathrm{mm}^2$ and inter bar distance was 5.08 mm. Circuit boards were molded with casting resin in opaque POM devices (Appendix A). Interior sides of light emitting (side with PSDs) and light localization circuit boards (side with IR LEDs) were facing towards a lateral line canal –which was milled inside the opaque device– (see Appendix A). Additionally the lateral line canal housed a silicon bar array (Fig. 3.39). The silicon bar array consisted of 8 silicon bars sized $977.75 \pm 24.83\,\mu$m width, $149.25 \pm 6.67\,\mu$m thick and $2564.00 \pm 169.15\,\mu$m height ($\pm$ s.d. $n = 8$). The method for producing silicon bar arrays was devoloped during this work and is not shown due to the option of patenting. Note that all fabrication steps were available with automatic fabrication and that in the case of manual fabrication maximum standard deviation of bar dimensions was 6.6% of mean value.

3.5.2 Performance test of the 8 channel lateral line sensor

Sensor signals cause by two vibrating spheres and Kármán vortex street

The circuit board showed 7 of 8 fully functional channels. Due to a short circuit 1 channel (channel 2) produced signals, but without an amplification of one anode current in the first amplification step. Channels 5 to 8 were picked out for recordings. Two vibrating spheres (50.0 Hz and 49.8 Hz) caused beating sensor signals (Fig. 3.40 a). All recorded channels (Fig. 3.40, Ch 5 to Ch 8) showed a beat ($f_b = 0.1$ Hz, Fig. 3.40 a) and a superimposed ($f_s = 49.9$ Hz, Fig. 3.40 b) frequency. Both frequencies coincide with theoretical frequencies.

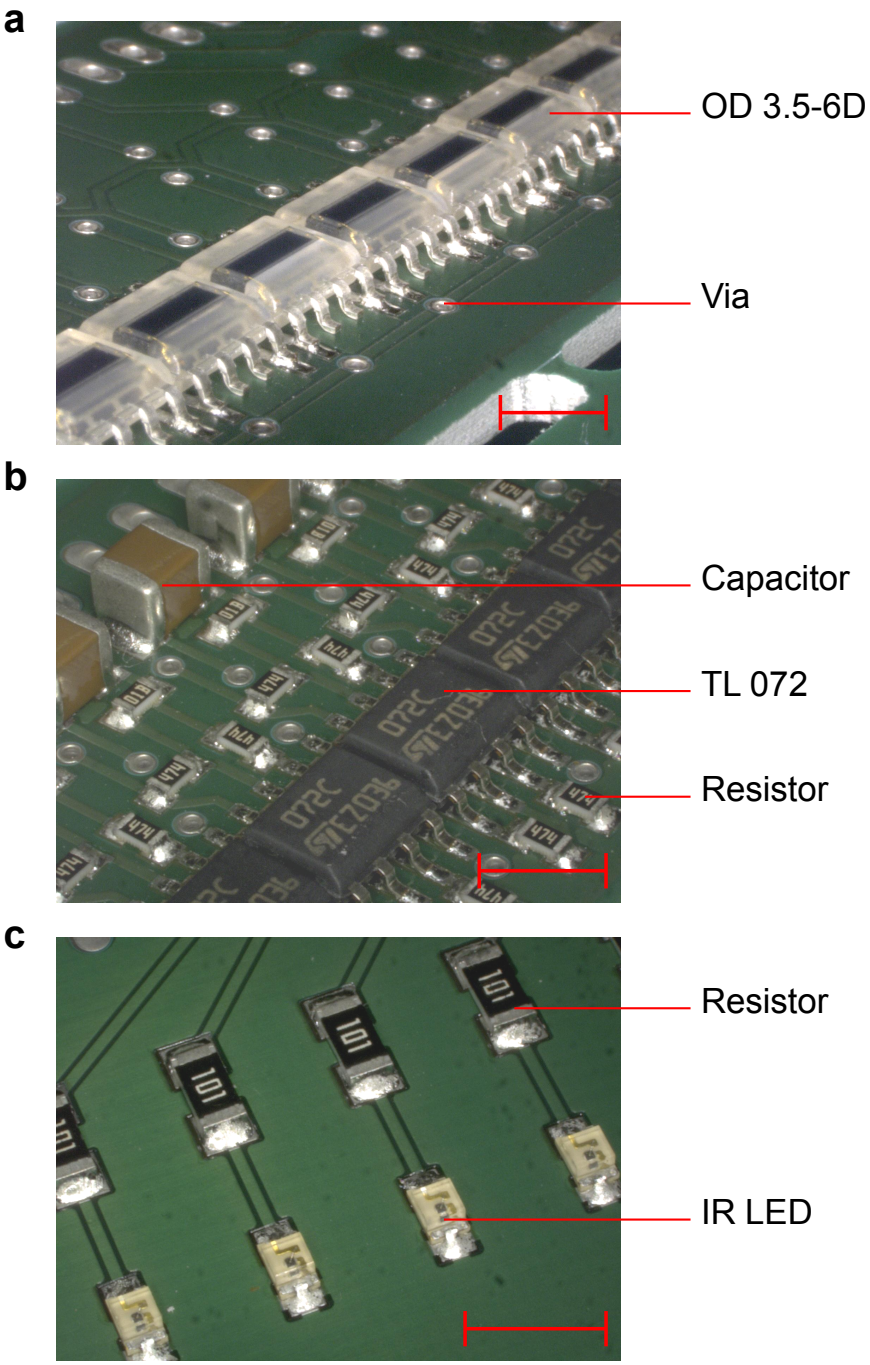

Figure 3.38: Un-molded light localization (interior side: a, exterior side: b) and IR emitting (interior side: c) circuit boards. IR LEDs (c) emit light which was guided through silicon bars (not shown). The position of the light spot – leaving the silicon bar – was measured with a PSD (OD3.5-6D, a) followed by an amplification and AC filter circuit (b, resistors, capacitor and 2 channel operational amplifier TL 072). Scale bar: 2.5 mm. Photographs in cooperation with Matthias Mayser, NEES institute, Bonn.

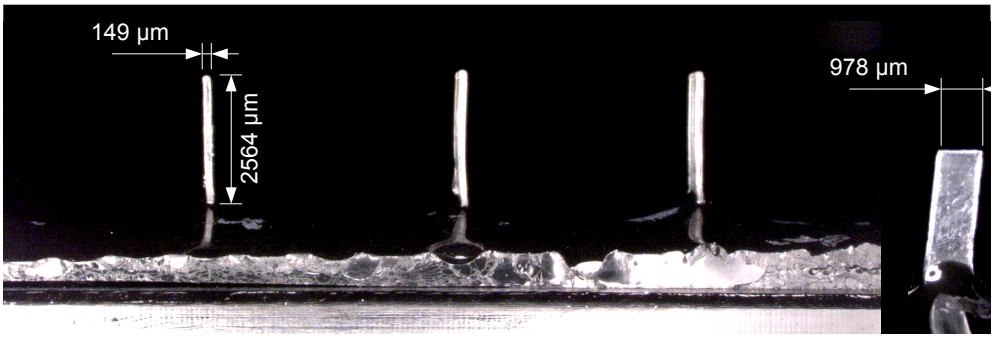

Figure 3.39: Detail of an 8 channel bar array. The side view (left) shows 3 silicon bars. IR LEDs (not shown) located at the bottom of the array illuminated silicon bars. Light leaving the tip of silicon bars was localized. The surface of the bar array was covered by an opaque sheet to avoid background light. Bars were 149 μm thick, 2564 μm height (left) and 978 μm width (right). Photographs in cooperation with Matthias Mayser, NEES institute, Bonn.

$$f_b = \frac{50.0 - 49.8}{2} Hz \tag{3.1}$$

$$f_s = \frac{50.0 + 49.8}{2} Hz \tag{3.2}$$

Flow influenced low pass filtered (10 Hz) sensor signals (Fig. 3.41). More disturbances were visible if flow was present. An upstream (6 cm) cylinder (2 cm) increased those disturbances. Therefore it was possible to measure beating signals as well as flow fluctuations in parallel and to separate those signals by applying filters accordingly to the frequency range of signals. Time shifted fluctuations were visible in the case of a 2 cm cylinder which was placed 0 cm upstream of the sensor device (Fig. 3.42). Those time shifted signals showed oscillations due to vortex street oscillations. Note that signal forms altered with time –as expected– and continuously altered with place (channel number).

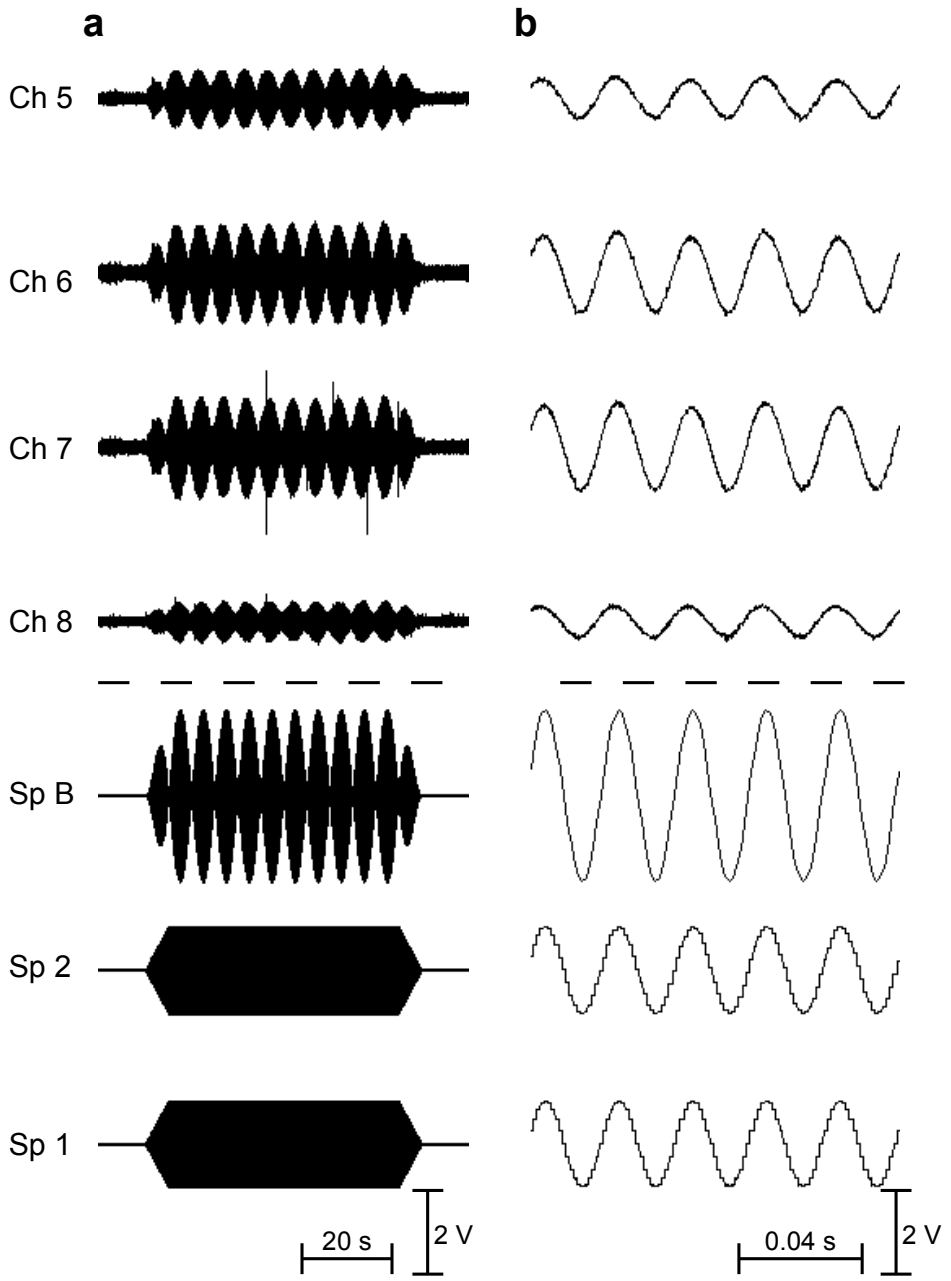

Figure 3.40: Beating sensor signals (Ch 5 to Ch 8) caused by 2 vibrating spheres (Sp 1 and Sp 2, Sp B = Sp 1 + Sp 2). Note that sensor signals followed the beating signal (a). The magnification (b) shows sensor signals in the case of maximum amplitude (Sp B). Recordings are plotted on equal scale. Ch 6 and Ch 7 as well as Ch 5 and Ch 8 had similar amplitudes. Outer channels had a lower amplitude as expected due to a higher distance to both vibrating spheres.

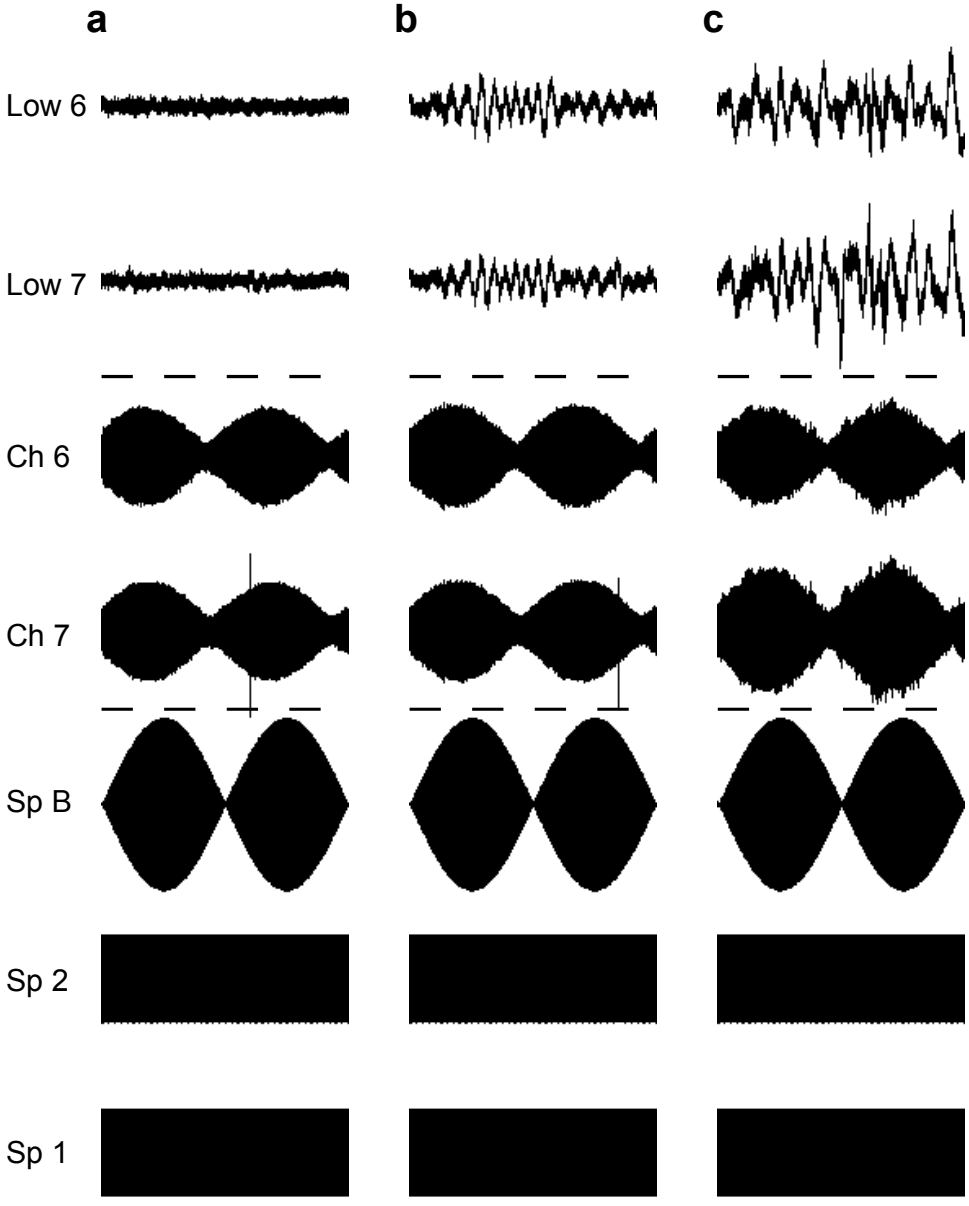

Figure 3.41: Beating sensor signals (Ch 6 and Ch 7) caused by 2 vibrating spheres (Sp 1 and Sp 2, Sp B = Sp 1 + Sp 2) and flow without (b) and with (c) a 2 cm cylinder located 6 cm upstream of the sensor device. Flow signatures were masked by the beating signal in unfiltered data (Ch 6 and Ch 7). Fluctuations were visible after applying a low pass filter (10 Hz, Low 6 and Low 7).

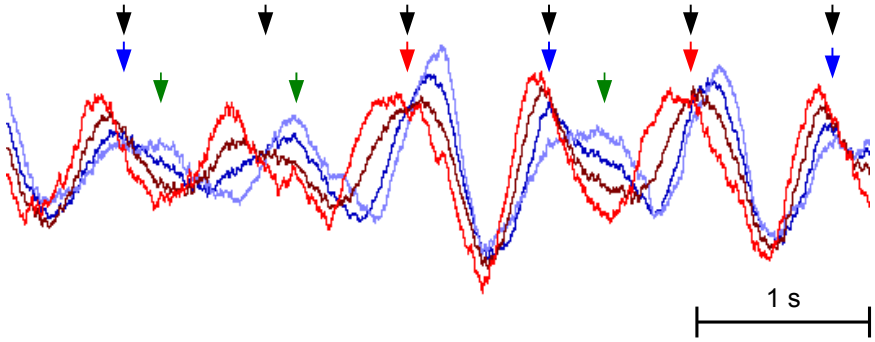

Figure 3.42: Recorded signature of a Kármán vortex street caused by a 1 cm cylinder. Recordings of four channels (light red: channel 5, red: channel 6, blue: channel 7 and light blue: channel 8) are shown. Black arrows indicate intervals of the vortex street oscillation. Size of signatures alter with oscillation cycle and channel number. Blue arrows indicate falling peak amplitudes with increasing channel number whereas red arrows indicate rising peak amplitudes with increasing channel number during one cycle of Kármán vortex street oscillation. Note that in some cycles intermediate peaks occur which rises with increasing channel number (green arrows).

4 Discussion

4.1 Trout prefer regions in which locomotory costs are reduced

4.1.1 Test of recording artifacts

In long time studies with thin wires inside the muscles of free swimming fish it is likely that the quality of recordings decreases over time. It was possible to perform long time studies with no visible changes of the quality of the recordings (Fig. 2.1). To verify the recordings a trout was killed and tied it inside the Kármán gait region to look whether the passive, vortex induced, motion of the animal produced artifacts on the recordings. No artifacts were found which may have been caused by the passive, Kármán vortex induced, motion.

4.1.2 Voxel preference and muscle activity

During all experimental runs trout preferred distinct sets of voxels. Mean muscle activity of preferred voxels was significantly below mean muscle activity of non-preferred voxels. This work confirms Przybilla et al. (2010) and Taguchi and Liao (2011) that animals were almost stationary (explored volume 15% and 9% in the up. and down. case). This work shows that an expression of muscle activity as function of three dimensional position was not consistent among experimental runs. For instance animals could show high muscle activity inside voxels preferred by other animals but always showed low muscle activity inside their own preferred voxels. In this work the behavioral modes Kármán gaiting, entraining and bow wake were not defined or classified over predefined rectangular regions Przybilla et al. (2010); Taguchi and Liao (2011) or body reactions (fin motions) Przybilla et al. (2010), which were observer dependent. Additionally this work focused not on short sequences in which animals showed an observer pre defined behavior, which was later analyzed, but focused on the long time performance of animals to access behavior and energy expenditure in general. For a more general expression of animal behavior voxel preference was defined over exploration of voxels. This value was expressed relative to an expected number of explorations retrieved

from a uniform distribution of animal presence. Due to this formulation this work allows the suggestion that trout in general prefer voxels in which locomotory costs were reduced. In natural habitats other factors including competitors, availability of food and predators may also influence behavior of trout.

4.1.3 Kármán gait, entraining, bow wake and wave mode

For a comparison with work of Przybilla et al. (2010) and Taguchi and Liao (2011) a threshold of trout presence of $k = 3.8$ was chosen. Voxels which were explored more than the threshold formed separable regions of animal presence similar with Kármán gait, entraining and bow wake region. Note that those regions were not rectangular in this work which is in contrast to the definition of two dimensional rectangular regions of Przybilla et al. (2010). Using this threshold a fourth preferred region was found called wave mode. This region occurred only at higher flow velocities (0.36 m/s and 0.48 m/s) and was located close to the surface downstream of the cylinder. Interestingly this region was the surface wave behind the cylinder and had a three dimensional flow structure due to the water air boundary. Trout also preferred the net region to hold station in the downstream case. Kármán gait, bow wake, entraining and wave mode region had curved shapes and three dimensional structures excluding entraining. Entraining had a cylindrical shape.

Muscle activity in Kármán gait, entraining and bow wake was significantly lower than in non-preferred regions. Liao (2004) also found that muscle activity during Kármán gait was reduced. Additionally this work confirms (Liao, 2004) that muscle activity during Kármán gait was phase locked to the alternating shed vortices. Liao (2004) found that no caudal red muscles were active during Kármán gait. In contrast recordings of this work show that caudal muscles were active during Kármán gaiting. Never the less caudal muscle activity was reduced during Kármán gait cycles compared to the muscle activity in non-preferred regions. The difference between findings of both work may depend on the electrode configuration used in Liao (2004) and this work. In this work a differential electrode configuration with a bigger inter-electrode distance was used. Therefore recordings were conducted from more muscle fibers than in the work of Liao (2004). Additionally recordings were conducted over longer time periods (3 hours) than in the work of Liao (2004).

4.1.4 Metabolism and muscle activity

Taguchi and Liao (2011) conducted oxygen measurements of trout during Kármán gait, entraining, bow wake and free stream swimming in a long time study and found that during free stream swimming oxygen consumption of trout was significantly higher than during other behavioral modes (KG, EN, BW and FS). Oxygen consumption is a measure of the metabolism and therefore the work of Taguchi and Liao (2011) clearly shows that trout show reduced metabolism during Kármán gait, entraining and bow wake compared to metabolism during swimming in undisturbed flow. This work coincide with these findings. Muscle recordings can not provide a measure of the total metabolism but only a measure of the energy expenditure activity of distinct muscles. In contrast the measure of oxygen consumption provide a measure of the total metabolism but time resolution and therefore spatial resolution is low. Both, the measure of oxygen consumption and electromyography are complementary methods providing on the one hand the three dimensional structure of preferred regions and on the other hand the energy expenditure.

4.1.5 Flow field, region preference and preference of turbulence

Particle image velocimetry data of this work show that stable vortex streets occurred during experiments. The flow field showed decelerated flow in the bow wake region, accelerated flow in the entraining region and unsteady alternating flow in the Kármán gait region as expected. Przybilla et al. (2010) found that entraining trout use a force balance between pressure drop due to the accelerated flow around the airfoil shaped body and drag caused by the flow. This work shows that preferred regions were bigger in upstream case than in downstream case. PIV data show that turbulent flow regime was only present downstream of the cylinder as expected. Pavlov et al. (2000) showed that fish prefer turbulent flow regimes on equal spatial scale than body size. In downstream case no turbulences in the scale of fish were present and only a small region in front of the cylinder of decelerated flow has formed. This explains the different size of preferred regions in up- and downstream case.

4.2 Neurons in the MON of rudd react on Kármán vortex streets

4.2.1 MON activity increased in the presence of a Kármán vortex street

Spike rate of recorded unit population (N = 31) increased with increasing cylinder diameter which was indicated by a positive regression slope of spike rate as function of cylinder diameter (m = 0.762 [S/s], p = 0.001). The MON consists of several layers and cell types (New et al., 1996; Bell et al., 2008). It is likely that the composition of recorded units was not equal to the composition of cell types of the MON due to at least two reasons. On the one hand the electrode was driven from dorsal to ventral in the hind brain. Therefore it is more likely that upper (dorsal) neuron types were recorded than deeper (ventral) neuron types. On the other hand neurons of different size emit different potentials as well as the probability to hit or come close to a unit differs. Therefore the increase of spike rate as function of cylinder size of all recorded units must not imply that the real MON population increases in spiking activity with increasing cylinder diameter. But the increase of spike rate as function of cylinder size implies that there were units which respond with an increase in spike rate to vortex streets caused by submerged cylinders.

4.2.2 Excitation and inhibition

The regression analysis of single neurons showed that 9 of 31 units increased significantly their spike rate with increasing cylinder diameter (stim condition). Those units were excitable units. During this study 2 of 31 units were found which decreased significantly their spike rate with increasing cylinder diameter. Those units were inhibitable units. Previous work also showed that there were excitable and inhibitable units inside the MON while stimulating the lateral line of goldfish with a vibrating sphere (Künzel et al., 2011) or bulk water flow (Bleckmann, 2008). In contrast, previous work found no units in lateral line nerve fibers during stimulation with vortex streets which significantly de- or increase their spike rate in the presence of a cylinder compared with uniform flow (Chagnaud et al., 2007).

4.2.3 Habituation and sensitisation

The regression analysis of single neurons showed that 4 of 31 units decreased significantly their spike rate with increasing cylinder diameter during post condition. This means that the presented cylinder size had an influence on the spike rate during the time after the cylinder has been presented and removed from the flow tank. This work therefore shows that some MON units habituated on the stimulus or were part of a regulatory network which inhibited those units after stimulus presentation. Habituation and inhibition enhances the dynamic range and sharpness of sensory systems. Units with strong habituation also showed a strong reaction on the stimulus (Units #10 and #15, see. Fig. 3.24). This is also visible from a negative correlation between regression slope of spike rates as function of cylinder size of stim and post cases ($m = -0.291$ [post/stim], $p < 0.001$). Interestingly 1 of 31 units increased significantly with its spike rate with increasing cylinder diameter during post condition. On a first glance this was not expected. On the one hand the exchange of cylinders caused surface waves which traveled through the flow channel. But 10 s before and after the change of cylinders were not analyzed. A reaction of units after 10 s of cylinder exchange to surface waves is not likely. On the other hand it is possible that the unit was part of a feedback network with excitation or was part of regulatory afferent fibers to the lateral line organ. The activity of a network with feedback connections could last longer than networks without feedback connections. Another possibility is that the electrode was attached to the neuron. This work gives strong evidence that habituation exists in the MON and lasts more than 10 s. This work can not exclude sensitisation in the MON.

4.2.4 A view on all recorded units in terms of spike rates

Combining the data of all regression analysis of single units inside one figure resulted in an image with no visible separable groups (Fig. 3.24). Units seem to exist in a continuum ranging from excitable to inhibitable units with respect to Kármán vortex streets as stimulus. The number of units was highest in regions with less or no reaction (concentration of units close to the origin) and decreased with increasing distance to the origin.

4.2.5 Spike pattern

Recorded units showed peak frequency similar to vortex shedding frequency. In contrast to lateral line nerve fibers, many recorded MON units with a sharp peak frequency were found. Interestingly also inhibitory units were found which also showed a similar peak frequency than vortex shedding frequency. No unit with an absolute peak frequency of twice the vortex shedding frequency was found but units with smaller harmonic peaks were found (see. Figs. 3.19, 3.20, 3.21 and 3.22). The spike interval plot coincide with FFT data and additionally shows that units were in bursts active. Bursts higher the probability for deeper neurons to fire.

4.2.6 Discrimination of vortex street caused by cylinders of different sizes

Single units were found which were able to discriminate different vortex street signals from each other in terms of spike rate and spike pattern. On the one hand the 2-way ANOVA showed that single units showed significant differences in spike rate during different cylinder presentations. On the other hand peak frequencies of some units were similar to vortex shedding frequency which differed with cylinder size. With increasing cylinder size vortex size increases and therefore also the stimulus. Spike rate often correlated with strength of stimulus. But also units were found with no significant correlation with cylinder size. Some of those units showed a peak frequency similar to the vortex shedding frequency. In almost all cases, as expected, the presence of a cylinder was discriminable from the case of no cylinder present in terms of spike rate or spike pattern or both.

4.2.7 Flow field and neuronal activity

Two units were found which correlated with the time series of flow components, which were parallel to the fish surface. The correlation map showed a peak close to the fish surface. This is expected due to the fact that hair cells in neuromasts were influenced by their adjacent flow field. That only a few units were found, with a strong correlation at a delay close to 0 ms, is expected. Neuromasts are widespread among the fish body. Therefore the laser sheet reached a small proportion of the flow field surrounding all neuromast.

4.2.8 MON units sharpen activity of Kármán vortex streets

Chagnaud et al. (2007) found that peak spiking frequency of lateral line nerve fibers (LLN) was similar to vortex shedding frequency. Therefore it was expected that vortex street signals propagate to the MON but unknown if vortex street signals were suppressed or sharpen. In contrast to the work of Chagnaud et al. (2007) - in which no significant differences in terms of spike rate were found - this work found significant differences in spike rates of MON units. With 20.8 [S/s] (Q.50) (Chagnaud et al., 2007) the measured spontaneous rate of LLN fibers was higher than spontaneous spike rate of recorded MON units (12 of 31 units, $Q0.50 = 1.17$ [S/s]). On the one hand brain areas involved in the processing of hydrodynamic information close to peripheral input often show higher spiking activity than deeper brain areas (Coombs et al., 1998). On the other hand the effect of different spontaneous activities between work of Chagnaud et al. (2007) and this work could also be due to slightly different set ups or fish species (*Carassius auratus* and *Scardinius erythrophthalmus*). MON units were found which showed almost no spikes during one half of the vortex street oscilation (Figs. 3.19 and 3.21 a). This is in contrast to the reaction of primary LLN fibers, which showed almost noisy spiking patterns (Chagnaud et al., 2007). Northcutt (1989), Montgomery et al. (1995) and Mogdans and Kröther (2001) found that neurons inside the MON were innervated by a wide spatial distribution of neuromasts. Additionally Künzel et al. (2011) found that MON units had diverse receptive fields and diverse reaction characteristics with respect to dipole stimuli which indicate that there was no uniform interpretation for MON units reaction with respect to this kind of stimulus. PIV measurements of this work show that vortex street signals had a large spatial extension alongside the fish. This is supported by the expected wavelength which calculates with $\lambda = v/f$ with velocity v, frequency f and wavelength λ. In this work calculated wavelengths were 5, 10 and 15 cm ($v = 6$ cm/s). Note that this wavelengths are on equal scale than body size of experimental animals ($L = 6$ - 9 cm). Therefore it is likely that noisy information of primary lateral line afferents – which carry vortex street signals in terms of frequency (Chagnaud et al., 2007) – were integrated over a wide distribution of Neuromasts. Note that a sharp representation of vortex street signals was found in this work and that response of MON units consisted in a continuum from no reaction to a strong reaction in terms of spike rate or spiking peak frequency or both. This is an indication that the MON is involved in the processing of vortex information and hydrodynamic distortions on equal scale than body length.

4.2.9 Filter properties of MON and feedback regulation of locomotion

The MON has a cerebellar like structure (Bell et al., 2008) and it is known that lateral line input in the medulla of goldfish is central inhibited by neurones which control active body movements (Russel, 1976). Active body movements produce pressure signals which lead to signals acting on the lateral line system of fish. It stands to reason that those signals were filtered. Bell et al. (2008) suggest that cerebellar like structures generate predictions about expected events. Due to the vicinity of the MON to the cerebellum, its cerebellar organization, the finding of this work that medullary neurons sharpen vortex street signals and that fish prefer turbulent regions (Liao, 2004; Pavlov et al., 2000) in which they show less energy effort it stands to reason that a feedback loop exists which fine tune locomotion. It stands to reason that the MON plays a major role in a feedback loop for efficient locomotion in turbulences. A feedback mechanism with intrinsic control may function that self induced hydrodynamic events were subtracted from the hydrodynamic image - according to Bell et al. (2008) - and then unexpected signals - like Kármán vortex streets - were perceived, sharpened - according to this work - and projected to motor units which adjust locomotion for better performance in the hydrodynamic flow field.

4.3 Distributed pore pattern of lateral line canals act as spatial filters

4.3.1 Frequency characteristics, signal amplitudes and functionality of the sensor

Theoretically the sensor (artificial neuromast) should have a band pass filter characteristic due to the elastic properties of the silicon bar and viscous damping by the canal fluid (damped spring system). No resonance frequency in a frequency range between 10 Hz and 80 Hz was found. In this range measurements show a decreasing sensitivity with increasing frequency. Pore diameters of ALLCs were calculated (and than designed) (Poiseuilles law) such that equal volume flow through the sensor device occurred if the pressure difference between the left and right pore row was equal among different ALLCs. Therefore an increase in pore number was correlated with a decrease in pore diameter. In contrast to calculations, ALLC 1P affected the amplitude of the sensor signal differently than other ALLCs. A difference in signal attenuation means that only relative amplitude values acquired among different ALLCs were comparable. To exclude effects due to different signal attenuation through ALLCs, autocorrelation was used for further analysis. Autocorrelation is independent of signal amplitude scaling if the internal sensor noise (chip noise, circuit noise) is small (less than 10%) compared to the external sensor signals (hydrodynamic fluctuations). This was the case for the sensor which was used in this work. A vibrating sphere signal caused vibrating signals measured with ALLCs P1 and P13. ALLC P1 attenuated air bubble noise less than ALLC 13P (not according to previous experiments) (c.f. Fig. 3.32). This indicate that the sensor was fully functional. Note that this work can exclude any stimulus artifacts since an ALLC without pores did not lead to sensor output fluctuations under all conditions applied.

4.3.2 ALLC type and signal to noise ratio

This work hypothesize that many small pores connected to one large canal will integrate an incoming signal over the spatial domain due to Poiseuilles law (see also Appendix C: pipe network equation from Klein (2009)).

$$\vec{v} = (f_p K + f_c I)^{-1} P \vec{p} \tag{4.1}$$

with $K = \begin{pmatrix} 2 & -1 & 0 & \cdots & 0 \\ -1 & 2 & -1 & \cdots & 0 \\ 0 & -1 & 2 & \cdots & 0 \\ \vdots & \vdots & \vdots & \ddots & \vdots \\ 0 & 0 & 0 & \cdots & 2 \end{pmatrix}$, $P = \begin{pmatrix} 1 & -1 & 0 & \cdots & 0 & 0 \\ 0 & 1 & -1 & \cdots & 0 & 0 \\ 0 & 0 & 1 & \cdots & 0 & 0 \\ \vdots & \vdots & \vdots & \ddots & \vdots & \vdots \\ 0 & 0 & 0 & \cdots & 1 & -1 \end{pmatrix}$ and identity

I is the solution of flow velocities ($\vec{v}$) inside a tube with many pores with outer pressures ($\vec{p}$).f_c, f_p, K and P were canal and pore parameters (see Appendix C: pipe network equation). Note that for large pore diameters f_p is zero and only pressure difference of adjacent pores had an effect on flow velocity. In contrast if pore diameters are small f_p is large and the pressure signal, acting on one pore, propagates over long distances through the lateral line canal.

Air bubbles greatly changed sensor output in all experimental runs. Nevertheless group 2 was less affected by air bubble induced noise under flow (vortex street) and no flow conditions (vibrating sphere). Interestingly not only air bubbles but also vortex street age affected peak autocorrelation coefficients. The upstream distance (longer distance means longer traveling time of vortices until impact on sensor) between ALLC center and D-cylinder was anti-correlated to peak autocorrelation coefficient. In the case of vortex street age, ALLC 13P lead to higher peak correlation values than ALLC 1P if the cylinder was placed more than 3 cm upstream of the center of the ALLC. This work hypothesize that parts of 3 dimensional degraded vortices passed the ALLC at different vertical positions due to random processes and degradation. Note that ALLC 13P covered a larger vertical section than ALLC 1P which may lead to more self similar sensor output in this case. Note that the experiment examining the influence of air bubble noise on vortex streets was also conducted with an upstream D-cylinder distance of 6 cm which is in the range where a significant difference between ALLC 13P and ALLC 1P was found. Under no noise conditions ALLCs of group 2 lead to significantly higher peak autocorrelation values than ALLCs of group 1 if a significant difference between ALLCs was found. If air bubbles were present, the

vortex street signal was distorted, indicated by decreased peak autocorrelation values in all data. ALLCs with large vertical extensions like ALLC 13P (group 2) showed a tendency for higher peak autocorrelation values. Peak autocorrelation values of both groups dropped similar if much noise (noise level 2) was present. This indicates that all ALLCs performed similar under high noise conditions. In contrast if less noise was present (noise level 1) the relative drop down of peak autocorrelation coefficient of ALLCs of group 2 was less than ALLCs those of group 1. Data acquired with noise level 1 and noise level 2 indicate that there is a range where ALLCs of group 2 performed better in the detection of oscillating signals than ALLCs of group 1 and that there exist a maximum noise level where the spatial filter technique had its limitations. This work clearly shows that noise filtering was due to the spatial pore distribution. This work can exclude effects due to pore number and pore size. ALLC 1P and ALLC 33P leaded to similar results despite different pore numbers and sizes. Additionally ALLC 5Pw and ALLC 5Pn behaved according to group 2 and group 1 respectively. The only difference between both was the spatial pore distribution. In conclusion, this work shows that noise filtering by artificial lateral line canals is due to the spatial pore distribution. It is likely that pore diameter also has a temporal filter effect (frequency response). van Netten (2006) showed that the canal act as low pass filter. Smaller canal diameters lead to lower velocity amplitudes (for constant pressure gradient) and to a higher cut of frequency. It is obvious that lower flow velocities and smaller canal diameters – which means shorter bending bars – substatially decrease sensitivity of a sensor. This work hypothesize that if a high cut of frequency is necessary, many small parallel pores could also be used instead of a smaller canal radius. This would have the advantage that flow amplitude did not diminish.

4.4 Diminutions of lateral line canals enhance signal amplitude

This work shows that the presence of a diminution alters the flow inside a lateral line canal. Maximum flow velocity always occurred in the center of the diminution. This is expected from the nearly incompressibility nature of water and from the quotient of transection areas of tapered and non-tapered regions of the canal. Pressure drop of tapered sections of the lateral line canal lead to a higher pressure drop (hydrodynamic resistance) than non-tapered sections according to Poiseuille equation (Blevins, 1984)

$$\Delta P = \frac{8\mu L Q}{\pi r^4} \tag{4.2}$$

with pressure difference between both tube ends ΔP, dynamic viscosity μ, length of the tube L, diameter of the tube r and volumetric flow rate Q. Both , acceleration – due to transection area quotient which lead to an increase of flow velocity with decreasing diminution size – and pressure drop – which lead to a decreasing flow velocity with decreasing diminution size – are contradictory acting. The existence of an optimal diminution can be explained with a simplified model of two connected ($Q_1 = Q_2$) tubes of different dimension and the solution of Poiseuilles equation

$$\Delta P_1 = \frac{8\mu L_1 Q_1}{\pi {r_1}^4} \quad \text{and} \quad \Delta P_2 = \frac{8\mu L_2 Q_2}{\pi {r_2}^4} \tag{4.3}$$

The outer pressure drop (ΔP) is equal to the sum of both partial pressure drops of both tubes

$$\Delta P = \Delta P_1 + \Delta P_2 = \frac{8\mu L_1 Q}{\pi {r_1}^4} + \frac{8\mu L_2 Q}{\pi {r_2}^4} \tag{4.4}$$

Let tube 1 be the non-tapered part with known parameters L_1 and r_1 and let tube 2 be the tapered tube with known length L_2 and unknown radius r_2 which had to be optimized by maximizing mean flow velocity v_2 inside tube 2. Mean flow velocity can be expressed in terms of volume flow

$$Q = v_2 \pi {r_2}^2 \tag{4.5}$$

leading to

$$\Delta P = \frac{8\mu L_1 v_2 \pi {r_2}^2}{\pi {r_1}^4} + \frac{8\mu L_2 v_2 \pi {r_2}^2}{\pi {r_2}^4} \tag{4.6}$$

This equation can be restated with

$$v_2 = k/(\frac{L_1 {r_2}^2}{{r_1}^4} + \frac{L_2}{{r_2}^2}) \tag{4.7}$$

and $k = \Delta P/(8\mu)$. To maximize v_2 the term $(\frac{L_1 {r_2}^2}{{r_1}^4} + \frac{L_2}{{r_2}^2})$ has to be minimized with respect to r_2. Differentiation of the term and evaluation of zero transections lead to

$$0 = 2L_1 r_2 {r_1}^{-4} - 2L_2 {r_2}^{-3} = 2r_2 * (L_1 {r_1}^{-4} - L_2 {r_2}^{-4}) \tag{4.8}$$

It is clear that $v_2 = 0$ for $r_2 = 0$. Therefore only the solution of the right side has to be considered

$$0 = (L_1 {r_1}^{-4} - L_2 {r_2}^{-4}) \Leftrightarrow r_2 = r_1 \left(\frac{L_2}{L_1}\right)^{-4} \tag{4.9}$$

The simulated lateral line canal was rectangular. Rectangular canals can be approximated by a tube with

$$r_d = \frac{2A}{P} \tag{4.10}$$

with hydraulic radius r_d, cross sectional area A and wetted perimeter P (Weilin et al., 2000). For the simulated canal with rectangular dimensions $500\,\mathrm{x}\,1000\,\mu\mathrm{m}^2$ equation 4.4 results

$$r_d = r_1 = \frac{2 * 500 * 1000}{2 * 500 + 2 * 1000} = 333.3 \tag{4.11}$$

Assuming a pore distance (center to center) of $5000\,\mu$m and a length of the diminution of $L_2 = 800\,\mu$m lead to $L_1 = 4200$. Using equation 4.4 results $r_2 = 220.19$. For a rectangular canal with $500\,\mu$m height and using r_2 with equation 4.4 the diminution width calculates to $282.36\,\mu$m. Note that the simulated optimal diminution of $300\,\mu$m is close to $282.36\,\mu$m. Diminutions were also present in nature and occur in head lateral line canals of teleosts (Bleckmann, 1994).It stands to reason that natural diminutions also amplify signal amplitude.

Optimal dimensions - which were found in this work - were used for the fabrication of a MEMS artificial lateral line sensor (Fig. 4.1) in the institute caesar (Bonn, Germany). First measurements were done in air with a MEMS prototype in which directional sensitivity and linearity of the signal with respect to volume flow rate was shown (Hendrik Herzog, unpublished). Therefore a proof of concept of optical canal neuromasts with MEMS already exists.

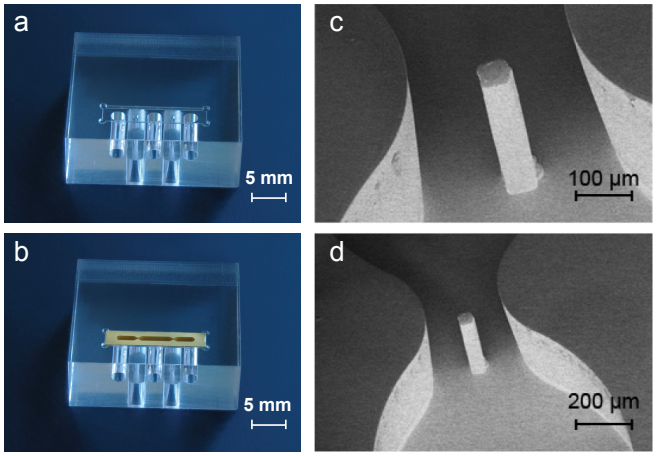

Figure 4.1: Artificial lateral line canal which was fabricated in MEMS. A housing (a) hold the fabricated silicon chip with bending bar structures (b). Magnifications (c and d) show the bending structure in the center of a diminution. Note that dimensions of the lateral line canal were similar to simulated dimensions. Photographs and REM images with permission of institute caesar (Bonn, Germany).

4.5 A reproducable artificial lateral line sensor

Several attempts to simulate, develop and build hair like flow sensors have been made (Humphrey et al., 1993; de Bree et al., 1998; Barth, 2004; Brücker et al., 2004; Krijnen et al., 2006; Kladt, 2007; Yang et al., 2010, 2011; Klein and Bleckmann, 2011; Klein et al., 2011; Klein and Bleckmann, 2012) ranging over capacitive, resistive and optical measurements. Capacitive and resistive methods were fabricated with MEMS and used almost stiff structures leading to less oscillation cycles and a low durability. Additionally most sensors work only in air. Flexible optical pillars have been developed (Brücker et al., 2004) but were filmed with a video camera which greatly enhances computational effort compared to the measurement of a direct electrical signal. Additionally expensive optics were necessary. In contrast to most other methods optical silicon bar sensors (Klein and Bleckmann, 2011; Klein et al., 2011; Klein and Bleckmann, 2012) were flexible, sensitive and need less computational effort as well as complex circuits. In contrast to freestanding structures, optical bars were sitting inside canals which avail additional filter properties and protect the bending structures from massive mechanical stress like collisions with obstacles. Optical artificial neuromasts were hand made and therefore showed widespread amplitude and frequency characteristics. Additionally photo-transistors with asymmetric aligned silicon bars were only piecewise directional sensitive. This work solved those disadvantages by

developing techniques for automatic fabrication of silicon bars for reproduceable frequency and amplitude characteristics. Additionally directional sensitivity was improved in this work due to the use of a position sensitive device (PSD) for optical measurements. Circuit costs for PSD amplification were higher than those for the phototransistor but costs due to the possibility of automatic fabrication were lower. This work confirms Klein and Bleckmann (2011) and Venturelli et al. (2012) that vortex street cycles were visible in sensor output as function of place and time (Fig. 3.42). Optical bar sensors of this work with PSDs were more sensitive than pressure sensors used by Venturelli et al. (2012). Venturelli et al. (2012) used stronger vortex street signals and pressure sensors had a sensitivity of 0.1 Pa for the least significant bit of the AD conversion whereas optical bar sensors of this work showed smooth curves of vortex street signals with an amplitude lower than 0.2 Pa (approximation with 2D FEM simulation, see Appendix). This indicates that the sensitivity of optical bar sensors was at least 1 order of magnitude more senitive than those of Venturelli et al. (2012).

5 Future Prospects

5.1 Combining locomotion and hydrodynamic sense

On the one hand this work shows that region preference of trout - which were exposed to unsteady flow - anti-correlated to their energy expenditure. On the other hand this work shows that similar unsteady flow signals were processed in the hindbrain of common rudd. Additionally behavioural studies show that the lateral line is involved in station holding next to cylinders which were exposed to flow (Przybilla et al., 2010). It stand to reason that a neuronal network in fish exist which uses hydrodynamic information to fine tune locomotion. This would ease station holding and navigation inside a complex hydrodynamic habitat. Navigation in turbulent, three dimensional flow, is a complex task and an underlying feedback algorithm like a possible neuronal circuit is of interest for the development of algorithm for autonomous water vehicles. Therefore further research should focus on the examination of neuronal and muscle activity of free swimming fish exposed to unsteady flow while observing the present flow field. The information gathered with artificial lateral line sensors under similar hydrodynamic conditions may help to increase knowledge of the biological system as well may function as part of a feedback loop of autonomous water vehicles.

5.2 Signal processing in the lateral line pathway and hydrodynamic imaging

Neuronal circuits of fish in the lateral line pathway are not well understood, especially for higher brain areas. This work shows that in contrast to dipole stimuli (Künzel et al., 2011), hydrodynamic stimuli of vortex streets propagate well in the MON. Additionally this work shows that flow fluctuations projected on a linear artificial lateral line array caused signals which alter in time and space. It is known that a somatotopic map of hydrodynamic information exist in goldfish (Plachta et al., 2003) which means that a representation in space is present. Together with the knowledge that hydrodynamic and visual information converge in the teleost brain (Kirsch et al., 2002) and multimodal information is used during feeding and

station holding (New, 2002; Przybilla et al., 2010) the question is near if a lateral line system may also provide enough information for hydrodynamic imaging or at least for pattern or object recognition. Several methods in neuro-informatics are known for pattern recognition, classification and data reconstruction. One pattern classification algorithm is called support vector machine (Steinwart and Christmann, 2006). Support vector machines were promising due to robust classification and fast computation time during classification at runtime. Future work should observe hydrodynamic images with artificial lateral line sensors and use classification algorithm to look if a classification of objects or flow regimes is possible. Preliminary data indicate that the discrimination of different cylinders at various bulk flow velocities and for various cylinder positions is possible (Maximilian Bothe, Bachlor thesis, University of Bonn, Germany, Fig. 5.1). Work should combine PIV and artificial lateral line measurements to research on flow reconstruction algorithms of the near field from data obtained with artificial lateral lines while keeping in mind that a superficial lateral line system also exists in nature which may provide necessary information for this task.

5.3 Commercial hydrodynamic sensors and the biomimetic flow sensor

This work proposes a biomimetic hydrodynamic sensor based on principles which were transfered from the lateral line organ of fish. The fabrication of the proposed sensor is available with automatic fabrication techniques which is necessary for a commercial use. Another necessary constraint for commercialization of the proposed sensor system is either a better performance, lower costs or a new field of application of the sensor. Future work has to compare commercial available sensors with the proposed sensor in terms of sensitivity, bandwidth, durability and production costs.

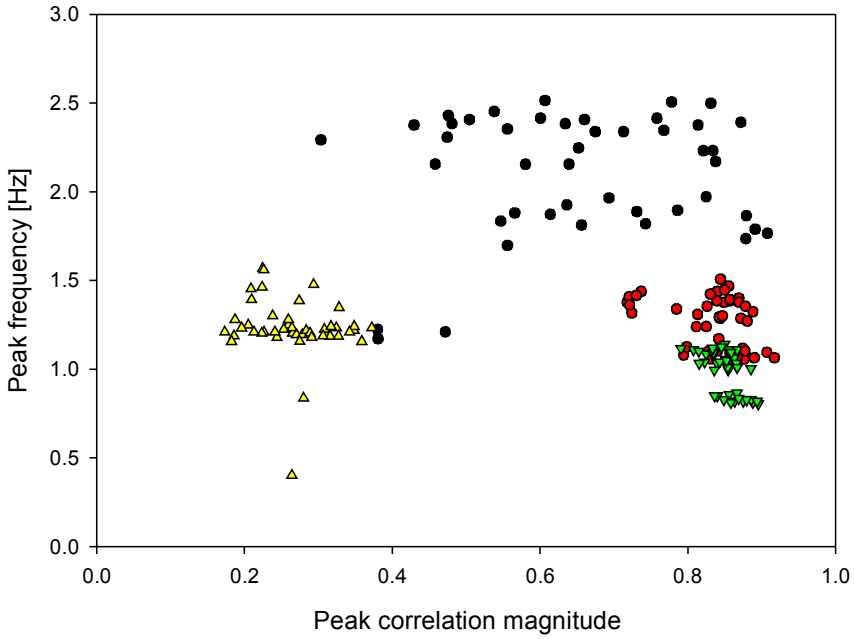

Figure 5.1: Object classification with a two channel artificial lateral line array. A two channel artificial lateral line array was exposed to cylinders of different diameters (yellow: no cylinder, black: 1 cm, red: 2 cm and green: 3 cm) in a flow channel. Peak frequency of the upstream sensor decreased whereas peak cross correlation magnitude between both sensor signals increased with increasing cylinder diameter. Data points of similar experimental conditions cluster in distinct regions with less overlap (no overlap in 3 dimensions, cross correlation delay of peak magnitude, not shown) which is necessary for object classification. Note that during the experiment 3 bulk flow velocities (7.0, 8.7 and 9.5 cm/s) and 3 cylinder positions (4, 6, and 8 cm upstream) were used with 5 repetitions for each experimental case.

Summary

This work investigated the energy expenditure and the hydrodynamic sense of fish exposed to unsteady flow, transfered natural principles of the hydrodynamic sense of fish to a biomimetic artificial lateral line system and uncovered the function of the occurrence of spatial pore patterns and diminutions in natural lateral line systems.

It turns out that trout – which were exposed to the flow field caused by a submerged cylinder – preferred distinct three dimensional regions in which locomotory costs were reduced. This work classified different behavioral modes over maxima of three dimensional region preference, which is a more abstract formulation than the definition of behavioral modes over rectangular two dimensional regions (Liao et al., 2003a,b; Liao, 2004; Przybilla et al., 2010). By uncoupling the appearance of trout from observer predetermined regions – as done in other work – this work comes to the conclusion that more the multiple appearance of trout at distinct regions correlated to their energy expenditure than the region itself. This means that animals could show high muscle activity inside regions preferred by other animals but always showed low muscle activity inside their own preferred region. Looking at all examined animals and experimental cases, this work coincide with the work of Liao et al. (2003a,b); Liao (2004); Przybilla et al. (2010), that entraining, Kármán gait and bow wake often were preferred regions. Additionally a fourth preferred region at higher flow velocities was found inside the surface wave behind the cylinder which is called wave mode.

It is well known that the lateral line system is involved in the perception of flow (Å. Flock and Wersäll, 1962; Bleckmann, 1980; Münz, 1985; Kalmijn, 1988; Coombs et al., 1988) and that signals caused by vortex streets were present but noisy in the periphery (Chagnaud et al., 2007). This work shows that the medial octavolateralis nucleus sharpen vortex street signals and that neuronal activity inside the MON correlated with flow. Most previous research on the function of the MON was done with vibrating spheres (Mogdans and Kröther, 2001; Künzel et al., 2011) or bulk water flow or both (Kröther et al., 2002). In contrast this work indicate that the MON is involved in a processing chain of vortex perception.

In sensory systems it is crucial to separate meaningful signals from noise which may occure in complex habitats. Nature has developed a stunning diversity of lateral line morphologies (Coombs et al., 1988). The function is not well understood. This work used biomimetic flow sensors based on the lateral line of fish and shows an artificial lateral line design with distributed pore patterns which significantly enhances signal to noise ratio. Therefore this work uncovers that at least one function of a similar natural morphological occurrence is a spatial filter. Additionally a finite element model with fluid structure interaction was used to develop a signal enhancing design of artificial neuromasts for fabrication with microelectromechanical systems. Interestingly a similar structure occurs in nature. This work shows that diminutions inside lateral line canals can amplify signals and that an optimal diminution size exists. Last but not least this work shows a new type of artificial lateral line canal sensor which is available with automatic fabrication techniques and lead to reproduceable sensors with similar properties.

Bibliography

F. Barth. Spider mechanoreceptors. *Curr. Opin. Neurobiol.*, 14:415–422, 2004.

C. Bell, V. Han, and N. Sawtell. Cerebellum-Like Structures and Their Implications for Cerebellar Function. *Annu. Rev. Neurosci.*, 31:1–24, 2008.

M. Bender, W. Gnatzy, and J. Tautz. The antennal feathered hairs in the crayfish: a non-innervated stimulus transmitting system. *J. Comp. Physiol., A*, 154:45–47, 1984.

H. Bleckmann. Reaction time and stimulus frequency in prey localization in the surface-feeding fish *Aplocheilus lineatus*. *J. Comp. Physiol., A*, 140:163–172, June 1980.

H. Bleckmann. *Reception of hydrodynamic stimuli in aquatic and semiaquatic ainmals*. Progr. Zool. Gustav Fischer Stuttgart, 1994.

H. Bleckmann. Peripheral and central processing of lateral line information. *J. Comp. Phys. A*, 194:145–158, 2008.

H. Bleckmann, A. Przybilla, A. Klein, A. Schmitz, S. Kunze, and C. Brücker. Station holding of trout: Behavior, physiology and hydrodynamics. In T. Cameron and H. Bleckmenn, editors, *Nature-Inspired Fluid Mechanics*, volume 119 of *Notes on Numerical Fluid Mechanics and Multidisciplinary Design*, pages 161–177. Springer Berlin / Heidelberg, 2012.

R. Blevins. *Applied fluid dynamics handbook*. Van Nostrand Reinhold Co., New York, 1984.

R. Blevins. *Flow-induced vibration*. Van Nostrand Reinhold, 1990.

C. Brücker, J. Spatz, and W. Schröder. Wall shear stress imaging using microstructured surfaces with flexible micro-pillars. *Application of laser techniques to fluid mechanics.*, 12th international symposium:number 7–5, 2004.

B. Chagnaud, H. Bleckmann, and J. Engelmann. Neural responses of goldfish lateral line afferents to vortex motions. *J. Exp. Biol.*, 209:327–342, 2006.

B. Chagnaud, H. Bleckmann, and M. Hofmann. Kármán vortex street detection by the lateral line. *J. Comp. Physiol., A*, 193(7):753–763, Jul 2007.

S. Coombs, J. Janssen, and J. Webb. Diversity of lateral line systems: evolutionary and functional considerations. In J. Atema, R. Fay, A. Popper, and W. Tavolga, editors, *Sensory biology of aquatic animals*, pages 553–593. Springer, Berlin Heidelberg New York, 1988.

S. Coombs, M. Hastings, and J. Finneran. Modeling and measuring lateral line excitation patterns to changing dipole source locations. *J. Comp. Physiol., A*, 178(3):359–371, 1996.

S. Coombs, J. Mogdans, M. Halstead, and J. Montgomery. Transformation of peripheral inputs by the first-order lateral line brainstem nucleus. *J. Comp. Physiol., A*, 182:609–626, 1998.

H. de Bree, H. Jansen, T. Lammerink, G. Krijnen, and M. Elwenspoek. Bidirectional fast flow sensor with a large dynamic range. *J. Micromech. Microeng.*, 9:186–189, 1998.

E. Denton and J. Gray. Mechanical factors in the excitation of clupeid lateral lines. *Pro. R. Soc. Lond. B*, 218:1–26, 1983.

R. Dowben and J. Rose. A metal filled micro-electrode. *Science*, 118:22, 1953.

J. Engelmann, W. Hanke, and H. Bleckmann. Lateral line reception in still- and running water. *J. Comp. Physiol., A*, 188(7):513–526, Aug 2002.

C. Gerstner and P. Webb. The station–holding performance of the plaice pleuronectes platessa on artificial substratum ripples. *Can. J. Zool.*, 76:260–268, 1998.

S. Groe, W. Schröder, and C. Brücker. Nano-newton drag sensor based on flexible micro-pillars. *Meas. Sci. Technol.*, 17:2689–2697, 2006.

J. Humphrey and F. Barth. Medium flow-sensing hairs: Biomechanics and models. In *Adv. Ins. Physiol.* Elsevier, 2007.

J. Humphrey, R. Devarakonda, I. Iglesias, and F. Barth. Dynamics of arthropod filiform hairs. i. mathematical modeling of the hair and air motions. *Phil. Trans.: Biol. Sci.*, 340:423–44, 1993.

A. Kalmijn. Hydrodynamic and acoustic field detection. In J. Atema, R. Fay, A. Popper, and W. Tavolga, editors, *Sensory Biology of Aquatic Animals*, pages 83–130. Springer–Verlag, New York, 1988.

J. Kirsch, M. Hofmann, J. Mogdans, and H. Bleckmann. Responses of diencephalic neurons to sensory stimulation in the goldfish, carassius auratus. *Brain Res. Bull.*, 57:419–421, 2002.

N. Kladt. *Neurobiology and modeling of cuticular hair sensilla of scorpions. Response characteristics and implications for biomimetic design.* PhD thesis, University of Bonn, 2007.

A. Klein. Examination of artificial lateral line systems. Diploma Thesis, 2009.

A. Klein and H. Bleckmann. Determination of object position, vortex shedding frequency and flow velocity using artificial lateral line canals. *Beilstein J. Nanotechno*, 2:276–283, 2011.

A. Klein and H. Bleckmann. Lateral line canal morphology and noise reduction. In A. Popper and A. Hawkins, editors, *The Effects of Noise on Aquatic Life*. Springer, 2012.

A. Klein, H. Herzog, and H. Bleckmann. Lateral line canal morphology and signal to noise ratio. *Proc. SPIE*, 7975:797507, 2011.

G. Krijnen, M. Dijkstra, J. van Baar, S. Shankar, W. Kuipers, R. de Boer, D. Altpeter, T. Lammerink, and R. Wiegerink. Mems based hair flow-sensors as model systems for acoustic perception studies. *Nanotechnology*, 17:84–89, 2006.

S. Kröther, J. Mogdans, and H. Bleckmann. Brainstem lateral line responses to sinusoidal wave stimuli in still and running water. *J. Exp. Biol.*, 205:1471–1484, 2002.

S. Künzel, H. Bleckmann, and J. Mogdans. Responses of brainstem lateral line units to different stimulus source locations and vibration directions. *J. Comp. Physiol., A*, 197:773–787, 2011.

T. Lamers and B. Pruitt. The MEMS Design Process. In R. Ghodssi und P. Lin, editor, *MEMS Materials and Processes Handbook*. Springer, 2011.

J. Liao. Neuromuscular control of trout swimming in a vortex street: implications for energy economy during the Kármán gait. *J. Exp. Biol.*, 207:3495–3506, 2004.

J. Liao. A review of fish swimming mechanics and behaviour in altered flows. *Phil. Trans. R. Soc. Lond. B*, 362:1973–1993, 2007.

J. Liao, D. Beal, G. Lauder, and M. Triantafyllou. The Kármán gait: Novel body kinematics of rainbow trout swimming in a vortex street. *J. Exp. Biol.*, 206(Pt 6):1059–1073, Mar 2003a.

J. Liao, D. Beal, G. Lauder, and M. Triantafyllou. Fish exploiting vortices decrease muscle activity. *Science*, 302:1566–1569, 2003b.

G. Loeb and C. Gans. *Electromyography for experimentalists*. University of Chicago Press, 1986.

M. McHenry and S. van Netten. The flexural stiffness of superficial neuromasts in the zebrafish (*Danio rerio*) lateral line. *J. Exp. Biol.*, 210:4244–4253, 2007.

M. McHenry, A. Strother, and S. van Netten. Mechanical filtering by the boundary layer and fluid-structure interaction in the superficial neuromast of the fish laterl line system. *J. Comp. Physiol., A*, 194:795–810, 2008.

J. Mogdans and H. Bleckmann. Responses of the goldish trunk lateral line to moving objects. *J. Comp. Physiol., A*, 182:659–676, 1998.

J. Mogdans and S. Kröther. Brainstem lateral line responses to sinusoidal wave stimuli in the goldfish, *Carassius auratus*. *Zoology*, 104:153–166, 2001.

J. Montgomery, S. Coombs, and M. Halstead. Biology of the mechanosensory lateral-line in fishes. *Rev. Fish. Biol. Fish.*, 5:399–416, 1995.

H. Münz. Single unit activity in the peripheral lateral line system of the cichlid fish *Sarotherodon niloticus*. *J. Comp. Physiol., A*, 157:555–568, 1985.

J. New. Multimodal integration in the feeding behaviors of predatory teleost fishes. *Brain. Behav. Evol.*, 59:177–189, 2002.

J. New, S. Coombs, C. McCormick, and P. Oshel. Cytoarchitecture of the medial octavolateralis nucleus in the goldfish, carassius auratus. *J. Comp. Neurol.*, 366:534–46, 1996.

R. Northcutt. The phylogenetic distribution and innervation of craniate mechanoreceptive lateral lines. In S. Coombs, P. Görner, and H. Münz, editors, *The mechanosensory lateral line: neurobiology and evolution*, pages 17–78. Springer, New York, 1989.

D. Pavlov, A. Lupandin, and M. Skorobogatov. The effects of flow turbulence on the behavior and distribution of fish. *J. Ichthyol.*, 40:232–261, 2000.

D. Plachta, W. Hanke, and H. Bleckmann. A hydrodynamic topographic map in the midbrain of goldfish Carassius auratus. *J. Exp. Biol.*, 206(Pt 19):3479–3486, Oct 2003.

A. Przybilla, S. Kunze, A. Rudert, H. Bleckmann, and C. Brücker. Entraining in trout: a behavioural and hydrodynamic analysis. *J. Exp. Biol.*, 213:2976–2986, 2010.

Å. Flock and J. Wersäll. A study of the orientation of the sensory hairs of the receptor cells in the lateral line organ of fish, with special reference to the function of the receptors. *JCB*, 15:19–27, 1962.

I. Russel. Central Inhibition of Lateral Line Input in the Medulla of the Goldfish by Neurones which Control Active Body Movements. *J. comp. Physiol.*, 111: 335–358, 1976.

A. Schmitz, H. Bleckmann, and J. Mogdans. Organization of the superficial neuromast system in goldfish, carassius auratus. *J. Morphol.*, pages 751–761, 2008.

T. Shimozawa, J. Murakami, and T. Kumagai. Cricket wind receptors: thermal noise for the highest sensitivity known. In F. Barth, J. Humphrey, and T. Secomb, editors, *Sensors and Sensing in Biology and Engineering*, pages 145–157. Berlin: Springer-Verlag, 2003.

I. Steinwart and A. Christmann. *Support vector machines*. Springer, 2006.

M. Taguchi and J. Liao. Rainbow trout consume less oxygen in turbulence: the energetics of swimming behaviors at different speeds. *J. Exp. Biol.*, 214:1428–1436, 2011.

S. van Netten. Hydrodynamic detection by cupulae in a lateral line canal: Functional relations between physics and physiology. *Biol. Cybern.*, 94(1):67–85, Jan 2006.

S. van Netten and S. Khanna. Stiffness changes of the cupula associated with the mechanics of hair cells in the fish lateral line. *Proc Natl Acad Sci U S A*, 91 (4):1549–1553, Feb 1994.

R. Venturelli, O. Akanyeti, F. Visentin, J. Ježov, L. Chambers, G. Toming, M. Kruusmaa J. Brown, W. Megill, and P. Fiorini. Hydrodynamic pressure sensing with an artificial lateral line in steady and unsteady flows. *Bioinspir. Biomim.*, 7, 2012.

S. Vogel. *Life in Moving Fluids*. Princeton University Press, 1996.

P. Webb. Entrainment by river chub nocomis micropogon and smallmouth bass micropterus dolomieu on cylinders. *J. Exp. Biol*, 201:2403–2412, 1998a.

P. Webb. *Swimming*. CRC Marine Science Series, 1998b.

Q. Weilin, G. Mala, and L. Dongqing. Pressure-driven water flows in trapezoidal silicon microchannels. *Int. J. Heat Mass Transfer*, 43:353–364, 2000.

S. Windsor, D. Tan, and J. Montgomery. Swimming kinematics and hydrodynamic imaging in the blind mexican cave fish (astyanax fasciatus). *J. Exp. Biol.*, 211:2950–2959, 2008.

S. Windsor, S. Norris, S. Cameron, G. Mallinson, and J. Montgomery. The flow fields involved in hydrodynamic imaging by blind mexican cave fish (astyanax fasciatus). part i: open water and heading towards a wall. *J. Exp. Biol.*, 213: 3819–3831, 2010a.

S. Windsor, S. Norris, S. Cameron, G. Mallinson, and J. Montgomery. The flow fields involved in hydrodynamic imaging by blind mexican cave fish (astyanax fasciatus).part ii: gliding parallel to a wall. *J. Exp. Biol.*, 213:3882–3842, 2010b.

Y. Yang, N. Nguyen, N. Chen, M. Lockwood, C. Tucker, H. Hu, H. Bleckmann, C. Liu, and D. Jones. Artificial lateral line with biomimetic neuromasts to emulate fish sensing. *Bioinsp. Biomim.*, 5:1–9, 2010.

Y. Yang, A. Klein, H. Bleckmann, and C. Liu. Artificial lateral line canal for hydrodynamic detection. *Appl. Phys. Lett.*, 99:023701, 2011.

M. Zdravkovich. *FlowaroundCircularCylinders. Volume1: Fundamentals*. Oxford University Press, NewYork, 1997.

Acknowledgments

I want to thank Prof. Horst Bleckmann for the supervision of my work and giving me a high degree of freedom. I greatly acknowledge Prof. Wolfgang Alt for carefully reading my work and for several stimulating Whitsunday seminars. I want to thank Hendrik Herzog for stimulating high-level talks, a splendent time on conferences around the world and last but not least a wonderful time in Bonn. I acknowledge the work of Simon Kranz and Jan Winkelnkemper who did a great job during experiments without this work had took more time. I want to thank Maximilian Bothe for supporting experiments of an object classification study. I want to thank Matthias Mayser for taking images of my 8 channel circuits and bar arrays with the 3-D microscope of the NEES institute. I thank Ruth Kretschmer for carefully reading this work and commenting on the manuscript. I thank Joachim Mogdans for commenting on the manuscript. I want to thank Maren Frings for coffee and conversations which helped to refocus my minds. I am thankful for the work of Stephanie Rabus who helped me with paperwork. I acknowledge the work of Stephanie Noack and Dominic Holtkamp who hand made silicon bars for my artificial lateral line sensors. For the organization of the GRK Bionik I want to thank Prof. Dr. von der Emde and Dr. Anke Schmitz. I want to thank the group of Mr. Lacher of the institute caesar for the implementation of artificial lateral line sensors with MEMS technique. This work was funded by the BMBF and the DFG (Bionik Graduate - GRK1572). Thank you for a high dimension of freedom due to almost unbound funds and possibilities. Last but not least I want to thank my family who was there for me when it realy mattered.

Appendix

Devices and circuit boards

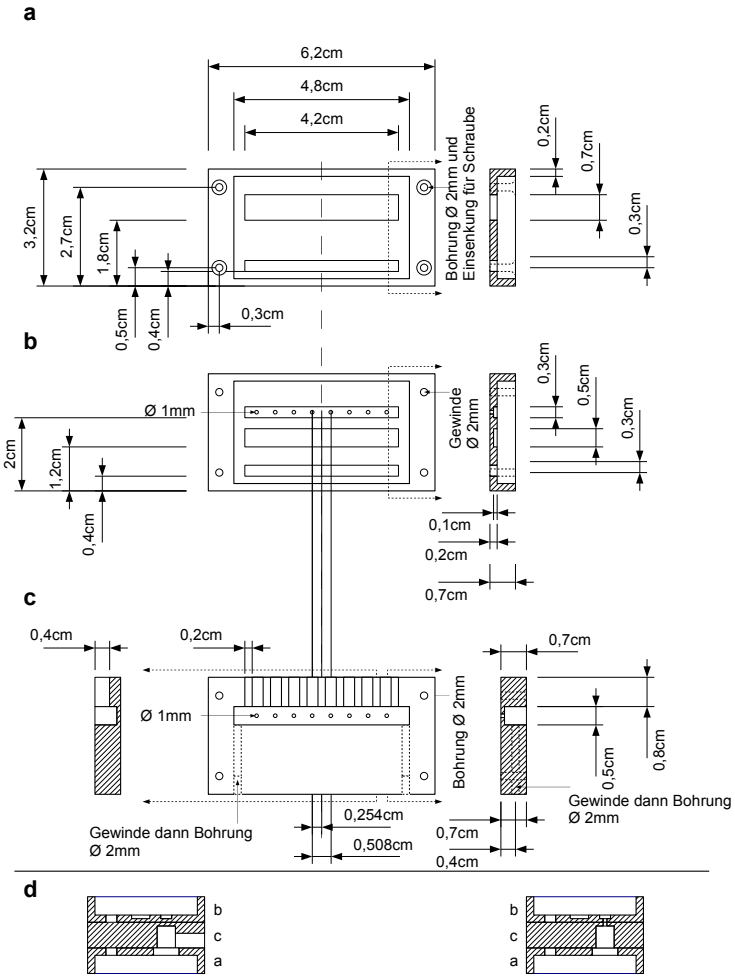

Device which was used to assemble eight channel circuits and bar silicon arrays. The light detection circuit was glued and molded in part a, the light emitting circuit was embedded in part b and the bar array was embedded in part c. Parts a, b and c were stacked (d) to form the sensor device. Note that due to the milling in c an artificial lateral line canal with 9 pores and 8 segments was formed.

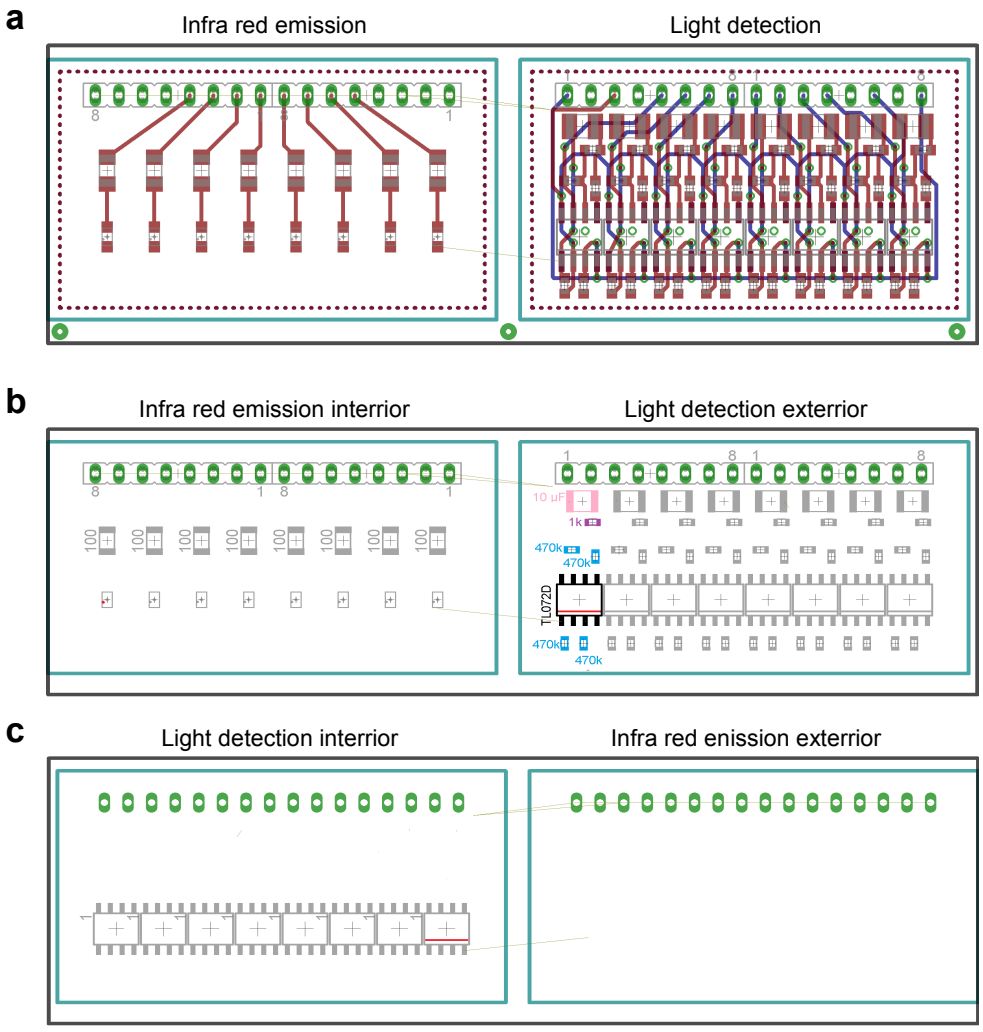

Circuit of the light amplification circuit. For better performance a PSD was used and signals amplified with two operational amplifiers. First the difference between both anodes was done to reduce the DC shift caused by the light itself on the photo-active area. Additionally the difference was amplified in this step. A high pass filter was used to eliminate the DC component before a second amplification step.

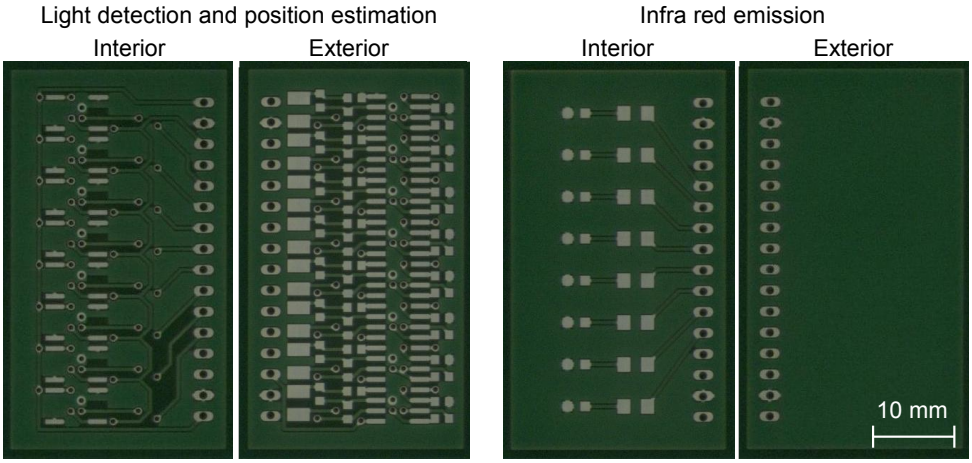

Unpopulated circuit boards. Interior sides of both circuit boards were facing the lateral line canal in the assembled device (not shown).

Programs

During the time of this work several programs have been developed. Programs were developed for analysis of other work, analysis of this work and my projects of interest. The programs developed during the time of this work consist of 6519 lines of C++ code (173,854 characters) and more than 878 lines of Matlab code (25,175 characters). This had produced more than 170 printed pages. Therefore programs were only added in digital form.

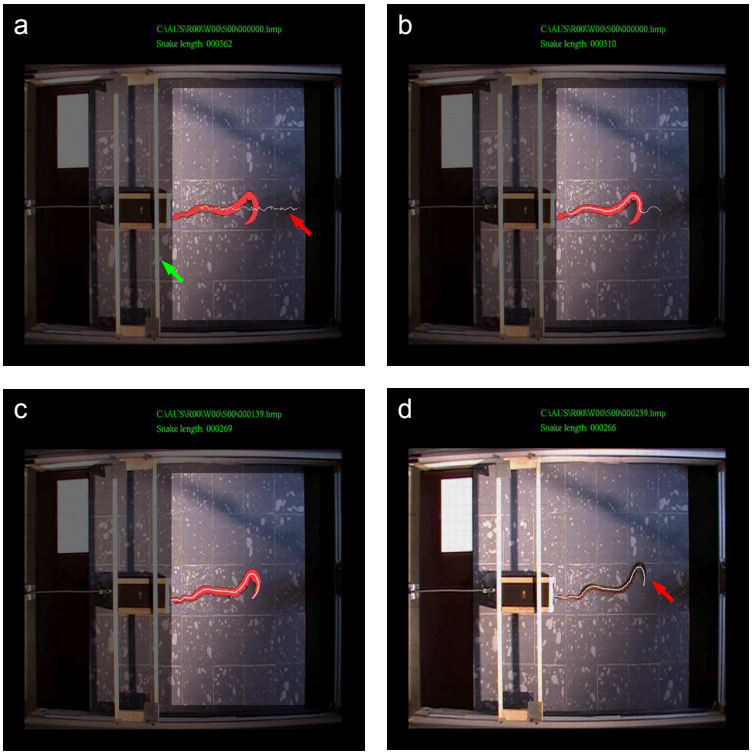

The Snake Tracker search for points inside the image which were possible points of the snake (a, red points). Additionally it optionally removes other moving objects like a hideout which was used for motivation (a, green arrow). Inside possible snake points a line with random noise is added (a, red arrow). The elastic line is fit into the cluster of snake points (b, red arrow). During the tracking process the line follows the center of the snake (c). Note that the snake had a similar color than the background (d, red arrow). Nevertheless the Snake Tracker was able to track the snake.

Snake tracker

1035 lines of C++ code, 26411 characters: This program was used to locate a snake on a background while the camera is not moving relative to the background. The program filters the snake pixel from the background and positions a chain of line segments through the center line of the snake. The chain is automatically adapted in length to the snake length. The program generates an output text-file with point coordinates of the link joints as function of frame number.

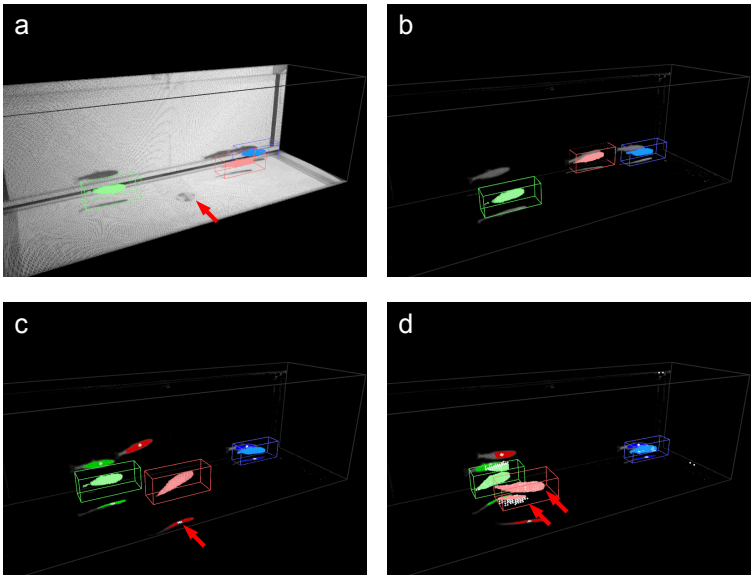

The Fish Tracker 3-D tracks up to 3 fish inside an experimental volume based on a bottom and side view (a, projected side and bottom view). Both views were calibrated using a linear model (see Materials and Methods). A D-shaped cylinder was placed inside the flow tank (a, red arrow). Tracked fish were color coded (b) and extension of fish clusters were indicated by parallelepipeds (b). The fish Tracker 3-D uses a physical model of mass and velocity to track the center of fish over time. Additionally tracked parallelepipeds were repulsive to each other to prevent from tracking a single fish with more than one parallelepipeds. Additionally the repulsive model is used on the two dimensional projection plane (c, red arrow). Note that using only two views the proposed problem may have nonunique solutions (d, red arrows). This means that more positions inside the flow tank were possible fish than real fish inside the flow tank. The Fish Tracker 3-D excludes those nonunique solutions by tracking fish over the time domain. Additionally the Fish Tracker 3-D is robust against single fish disappearing from the filmed volume. If the disappeared fish reenters the filmed volume, the parallelepiped is shifted towards its position.

Fish tracker 3-D

2803 lines of C++ code, 73782 characters: This program projects a video of side and bottom view over a 45 mirror in 3-D space. It uses a linear camera calibration explained in section 2.1.7 of this work. The program eliminates the background noise of non fish position and tracks three animals in parallel. Mathematically there is no unique solution if animals are located at distinct positions. To improve the chance of correct animal tracking in those situations a heuristic in time is used. This program produces text files with three dimensional position of three animals as function of frame number.

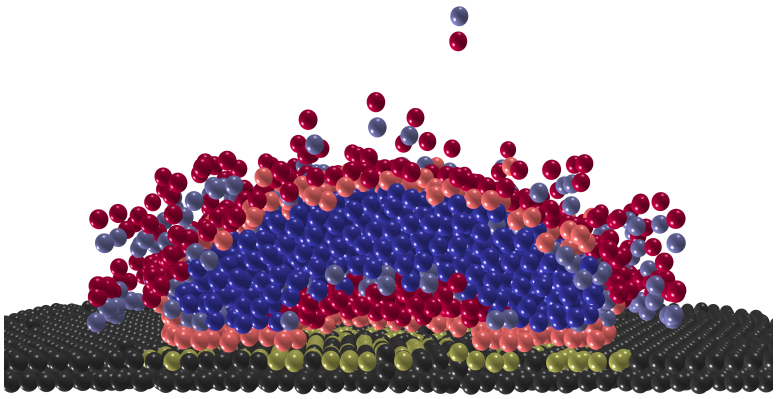

The particle reaction model showed semi cellular structures which self assembled close to the reactive surface (grey). Amphiphillic molecules (red: hydrophilic head, blue: hydrophobic tail) formed double membranes. A fluid filled chamber developed after membrane forming. Note that particles of the surrounding fluid were not plotted.

Particle reaction model

1583 lines of C++ code, 41737 characters: This program simulates particles with chemical properties. Particles interact over attractive, repulsive and viscous forces dependent on their type. Additionally distinct particle pairs are allowed to react. A reaction alters the properties of particles, produce a covalent bond between particles or both. A set of parameters was found which produced cellular membrane shaped objects with a cavity inside like postulated pioneer organisms in early evolution of life by Wächtershäuser.

Visualization of particle reaction model

1098 lines of C++ code, 31924 characters: This program draws particle model data and saves bitmaps.

Matlab scripts for analysis of energy expenditure as function of place

Raster the volume. 200 lines Matlab code, 6870 characters: This script uses two dimensional animal position data of the bottom and side view. The script calculates the three dimensional position of trout and uses a perspective correction with a linear model (see Materials and Methods). The experimental volume is divided into $1\,cm^3$ voxels. Mean EMG as well as number of stay of each voxel is calculated.

Create regions of KG, EN, WM, BW and FS. 190 lines Matlab code, 4661 characters: This script creates regions of defined number of presence.

Extract EMG values. 62 lines Matlab code, 2074 characters: This script calculates mean EMG values, volume and number of presence of regions. Regions were calculated with the previous script.

Matlab scripts for spike extraction, pattern analysis and unit PIV correlation

40s20s Spike rate analysis. 243 lines Matlab code, 6679 characters: This script calculates spike rates and auto correlations.

40s20s Spike pattern analysis. 183 lines Matlab code, 4918 characters: This script calculates FFT of spikes and cumulated inter spike intervals.

Pipe network equation

The lateral line canal is treated as a system of connected pipes (Klein, 2009). Under viscous dominated flow conditions the flow inside a pipe can be calculated using the Hagen Poiseuille equation van Netten (2006). The pipe network model should explain the general influence of different artificial lateral line proportions on the flow propagation inside the canal.

Assumption 1: The pressure acting on the lateral line canal pores does not fluctuate. In this case the flow inside a pipe could be described by the Hagen Poiseuille equation.

Assumption 2: The lateral line canal is a network of connected pipes (*segment pipes and pore pipes*).

Assumption 3: The flow inside the pipes is driven by the pressure difference between both pipe ends. There is only one pressure at each node influencing the flow of all attached pipes.

Assumption 4: No mass can be eliminated in the system. Especially the volume entering one node is equal to the volume going out.

Assumption 5: There are no effects due to the geometry of the nodes (*only true for viscous flow*).

A linear lateral line canal with N segments has $N+1$ pores with outer pressures P_1^p to P_{N+1}^p. There are $N+1$ nodes (*connection points of segments and pore tubes*) with pressures P_1^c to P_{N+1}^c inside. The flow velocity (v_1^p to v_{N+1}^p) in the pore tubes (*positive flow: outside to inside*) and the velocities in the segments (v_1^c to v_N^c) (*positive flow: lower indices to higher indices*) could be calculated by the Hagen Poiseuille equation

$$\dot{V} = \frac{\delta V}{\delta t} = \frac{\pi r^4 \Delta P}{8\eta L} \tag{1}$$

(*volume flow* $\dot{V}$*, volume* V*, time* t*, radius of the tube* r*, length of the tube* L *and pressure* P) if the pressure drop is known. The volume flow $\dot{V}$ could be expressed in terms of the velocity v and the radius of the tube ($\dot{V} = \pi r^2 v$). Setting this into equation 1 yields in

$$\pi r^2 v = \frac{\pi r^4 \Delta P}{8\eta L} \tag{2}$$

$$\Leftrightarrow \Delta P = 32 \frac{v \eta L}{D^2} \tag{3}$$

with a diameter of the tube $D = 2r$. Let $\Delta P_n^c = P_n^c - P_{n+1}^c$ be the pressure drop over the canal segment n and $\Delta P_n^p = P_n^p - P_n^c$ the pressure drop over the pore tube n. The pressure drop $P_n^p - P_{n+1}^p$ could be expressed as

$$P_n^p - P_{n+1}^p = \Delta P_{n|n+1} = \Delta P_n^c + \Delta P_n^p - \Delta P_{n+1}^p \tag{4}$$

The resulting linear equation system can be written as

$$\begin{pmatrix} \Delta P_{1_p|2_p} \\ \Delta P_{2_p|3_p} \\ \Delta P_{3_p|4_p} \\ \vdots \\ \Delta P_{N_p|N+1_p} \end{pmatrix} = \begin{pmatrix} \Delta P_1^c + \Delta P_1^p - \Delta P_2^p \\ \Delta P_2^c + \Delta P_2^p - \Delta P_3^p \\ \Delta P_3^c + \Delta P_3^p - \Delta P_4^p \\ \vdots \\ \Delta P_N^c + \Delta P_N^p - \Delta P_{N+1}^p \end{pmatrix} \tag{5}$$

Applying the Hagen Poiseuille equation explicit for all canal segments and pore tubes yields in

$$\Delta P_n^c = 32 \frac{v_n^c \eta L_c}{{D_c}^2} \qquad \text{and} \qquad \Delta P_n^p = 32 \frac{v_n^p \eta L_p}{{D_p}^2} \tag{6}$$

If we combine the equations 6 and 5 the result could be written as

$$\begin{pmatrix} \Delta P_{1_p|2_p} \\ \Delta P_{2_p|3_p} \\ \Delta P_{3_p|4_p} \\ \vdots \\ \Delta P_{N_p|N+1_p} \end{pmatrix} = 32\eta \begin{pmatrix} \frac{L_p v_1^p}{{D_p}^2} + \frac{L_c v_1^c}{{D_c}^2} - \frac{L_p v_2^p}{{D_p}^2} \\ \frac{L_p v_2^p}{{D_p}^2} + \frac{L_c v_2^c}{{D_c}^2} - \frac{L_p v_3^p}{{D_p}^2} \\ \frac{L_p v_3^p}{{D_p}^2} + \frac{L_c v_3^c}{{D_c}^2} - \frac{L_p v_4^p}{{D_p}^2} \\ \vdots \\ \frac{L_p v_N^p}{{D_p}^2} + \frac{L_c v_N^c}{{D_c}^2} - \frac{L_p v_{N+1}^p}{{D_p}^2} \end{pmatrix} \tag{7}$$

The volume flowing in each node is equal to the volume flowing out. To connect the segments and the pores, which could have different diameters, a factor has to be introduced.

$$\frac{v^c}{v^p} = \frac{{D_p}^2}{{D_c}^2} \tag{8}$$

Using the factor above and the mass conservation will result in the node equation

$$v_n^p = \frac{{D_c}^2}{{D_p}^2}(v_n^c - v_{n-1}^c) \tag{9}$$

Therefore equation 7 could be written as

$$\begin{pmatrix} \Delta P_{1_p|2_p} \\ \Delta P_{2_p|3_p} \\ \Delta P_{3_p|4_p} \\ \vdots \\ \Delta P_{N_p|N+1_p} \end{pmatrix} = 32\eta \begin{pmatrix} \frac{L_p D_c^2 v_1^c}{{D_p}^4} + \frac{L_c v_1^c}{{D_c}^2} - \frac{L_p D_c^2 (v_2^c - v_1^c)}{{D_p}^4} \\ \frac{L_p D_c^2 (v_2^c - v_1^c)}{{D_p}^4} + \frac{L_c v_2^c}{{D_c}^2} - \frac{L_p D_c^2 (v_3^c - v_2^c)}{{D_p}^4} \\ \frac{L_p D_c^2 (v_3^c - v_2^c)}{{D_p}^4} + \frac{L_c v_3^c}{{D_c}^2} - \frac{L_p D_c^2 (v_4^c - v_3^c)}{{D_p}^4} \\ \vdots \\ \frac{L_p D_c^2 (v_N^c - v_{N-1}^c)}{{D_p}^4} + \frac{L_c v_N^c}{{D_c}^2} - \frac{L_p D_c^2 (-v_N^c)}{{D_p}^4} \end{pmatrix} \tag{10}$$

Defining

$$f_p = 32\frac{\eta L_p D_c^2}{{D_p}^4} \qquad \text{and} \qquad f_c = 32\frac{\eta L_c}{{D_c}^2} \tag{11}$$

equation 10 could be written as

$$\begin{pmatrix} \Delta P_{1_p|2_p} \\ \Delta P_{2_p|3_p} \\ \Delta P_{3_p|4_p} \\ \vdots \\ \Delta P_{N_p|N+1_p} \end{pmatrix} = \begin{pmatrix} f_p(v_1^c - 0) + f_c v_1^c - f_p(v_2^c - v_1^c) \\ f_p(v_2^c - v_1^c) + f_c v_2^c - f_p(v_3^c - v_2^c) \\ f_p(v_3^c - v_2^c) + f_c v_3^c - f_p(v_4^c - v_3^c) \\ \vdots \\ f_p(v_N^c - v_{N-1}^c) + f_c v_N^c - f_p(0 - v_N^c) \end{pmatrix} \tag{12}$$

$$\Leftrightarrow \begin{pmatrix} \Delta P_{1_p|2_p} \\ \Delta P_{2_p|3_p} \\ \Delta P_{3_p|4_p} \\ \vdots \\ \Delta P_{N_p|N+1_p} \end{pmatrix} = \begin{pmatrix} f_p((v_1^c - 0) - (v_2^c - v_1^c)) + f_c v_1^c \\ f_p((v_2^c - v_1^c) - (v_3^c - v_2^c)) + f_c v_2^c \\ f_p((v_3^c - v_2^c) - (v_4^c - v_3^c)) + f_c v_3^c \\ \vdots \\ f_p((v_N^c - v_{N-1}^c) - (0 - v_N^c)) + f_c v_N^c \end{pmatrix} \tag{13}$$

$$\Leftrightarrow \begin{pmatrix} \Delta P_{1_p|2_p} \\ \Delta P_{2_p|3_p} \\ \Delta P_{3_p|4_p} \\ \vdots \\ \Delta P_{N_p|N+1_p} \end{pmatrix} = f_p \left(2 \begin{pmatrix} v_1^c \\ v_2^c \\ v_3^c \\ \vdots \\ v_N^c \end{pmatrix} - \begin{pmatrix} 0 \\ v_1^c \\ v_2^c \\ \vdots \\ v_{N-1}^c \end{pmatrix} - \begin{pmatrix} v_2^c \\ v_3^c \\ v_4^c \\ \vdots \\ 0 \end{pmatrix} \right) + f_c \begin{pmatrix} v_1^c \\ v_2^c \\ v_3^c \\ \vdots \\ v_N^c \end{pmatrix} \tag{14}$$

Setting

$$\vec{v} = \begin{pmatrix} v_1^c \\ v_2^c \\ v_3^c \\ \vdots \\ v_N^c \end{pmatrix} \qquad \text{and} \qquad \vec{p} = \begin{pmatrix} \Delta P_1^p \\ \Delta P_2^p \\ \Delta P_3^p \\ \vdots \\ \Delta P_{N+1}^p \end{pmatrix} \tag{15}$$

equation 14 could be written as

$$P\vec{p} = f_p K\vec{v} + f_c I\vec{v} \tag{16}$$

$$\Leftrightarrow \vec{v} = (f_p K + f_c I)^{-1} P\vec{p} \tag{17}$$

with $K = \begin{pmatrix} 2 & -1 & 0 & \cdots & 0 \\ -1 & 2 & -1 & \cdots & 0 \\ 0 & -1 & 2 & \cdots & 0 \\ \vdots & \vdots & \vdots & \ddots & \vdots \\ 0 & 0 & 0 & \cdots & 2 \end{pmatrix}$, $P = \begin{pmatrix} 1 & -1 & 0 & \cdots & 0 & 0 \\ 0 & 1 & -1 & \cdots & 0 & 0 \\ 0 & 0 & 1 & \cdots & 0 & 0 \\ \vdots & \vdots & \vdots & \ddots & \vdots & \vdots \\ 0 & 0 & 0 & \cdots & 1 & -1 \end{pmatrix}$ and identity I. This is the solution of a linear equation system which describes the flow inside the segments ($\vec{v}$) dependent on the canal parameters (f_c, f_p, K *and* P) and given pressures ($\vec{p}$) at the pore openings. Note that for large pore diameters f_p is zero and only pressure difference of adjacent pores had an effect on flow velocity. In contrast if pore diameters are small f_p is large and the pressure signal, acting on one pore, propagates over long distances through the lateral line canal.

Simulated vortex street with FEM

For a comparison of the sensitivity of the optical artificial neuromast with other sensors pressure differences at the pores were necessary. Fluid flow next to a cylinder was simulated in a transient analysis to retrieve a pressure field with pressure magnitudes comparable to the experiments. A vortex street developed during the simulation (Fig. 8 a). Pressure as function of time close to the wall and in 2 cm distance to the wall was extracted (Fig. 8 a, b red and blue lines). Flow inside the senor should be proportional to the pressure difference at the pore openings. Therefore the pressure difference was calculated (Fig. 8 a, b black lines). A peak pressure difference between two 1 cm spaced points of 0.192 Pa occurred close to the wall of the simulated flow tank 10 cm downstream of the cylinder.

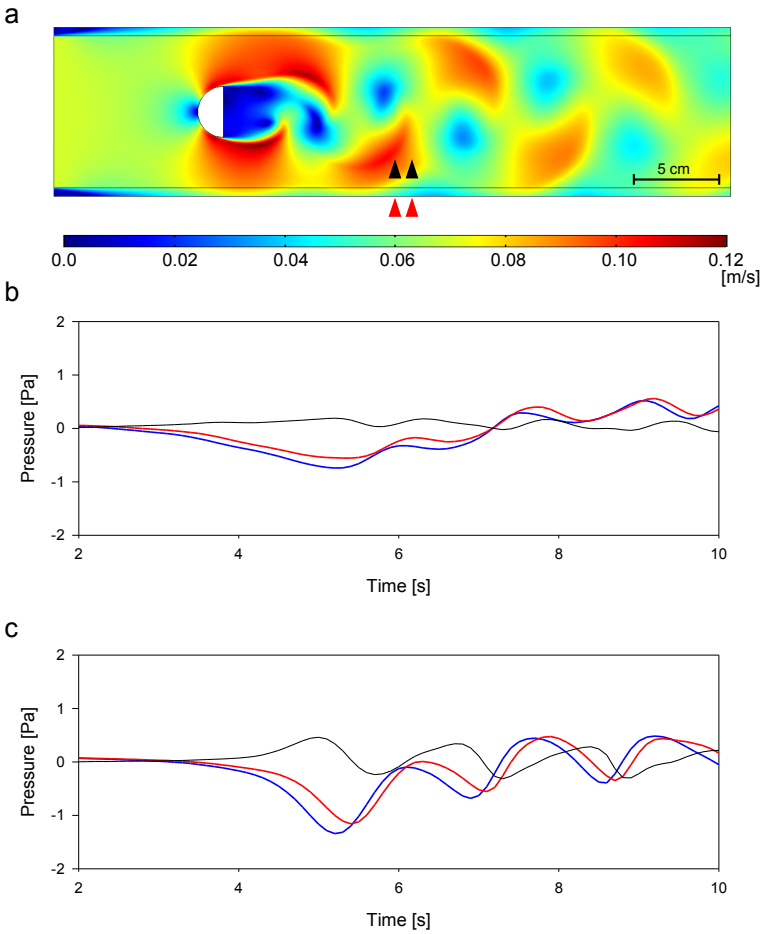

Development of a vortex street in FEM. In the transient study a vortex street occured (a, time = 10 s). Bulk flow velocity was 6 cm/s. Color coded velocity magnitudes showed alternating patterns. Pressure profiles over time (b, c) were extracted from the model at the location of red and black arrowheads (a). Red und blue lines in a and b indicate the pressure over time at the up- and downstream arrowhead (a). The black lines indicate pressure differences of red and blue lines. Peak magnitude of pressure differences close to the wall (a, red arrows, b) were close to 0.3 Pa. Note that a vortex street occured in the transient study after about 5 s.

Eidesstattliche Erklärung

Hiermit erkläre ich an Eides statt, dass ich die Dissertation selbst und ohne jede unerlaubte Hilfe angefertigt habe, dass diese oder eine ähnliche Arbeit noch keiner anderen Stelle als Dissertation eingereicht worden ist und dass sie an der im Publikationspart (Publications) aufgeführten Stelle auszugsweise veröffentlicht worden ist.

Bonn, den 26.10.2012